Development of medical devices for osteoarthritis diagnosis, antimicrobial, wound closure, and wound pH milieu monitoring

by

Shuxin Li

Presented to the Faculty of the Graduate School of

The University of Texas at Arlington in Partial Fulfillment

of the Requirements

for the Degree of

DOCTOR OF PHILOSOPHY IN BIOMEDICAL ENGINEERING

The University of Texas at Arlington

December 2019

ACKNOWLEDGEMENTS

I want to express my appreciation to my parents and families for their generous support on my studying, living, and researching. Also, I would like to send my sincere gratitude to my friends who helped me and entertained me throughout the past of my life. Moreover, I appreciate the support and instruction from my PI, Dr. Liping Tang, and my co-PI, Dr. He Dong. They have always been my primary reinforcement during my career as a researcher and given me constructive advices upon my projects. Last but not least, I would like to mention my collaborators and lab member for being extraordinarily supportive and cooperative throughout my PhD period.

Collaborators

Dr. Joseph Borrelli, Dr. Jon Senkowski, Dr. Wenjing Hu, Dr. Ashwin Nair, Ms. Hong Vu, Mr. Weike Chen, Ms. Su Yang, and Mr. Paul Renick.

Lab members

Dr. Jun Zhou, Dr. Wei Cong, Dr. Yihui Huang, Dr. Ashley Dacy, Dr. MinKyung Khang, Dr. Amir Hakamivala, Ms. Joyita Roy, Ms. Samira Izuagbe, and Mr. Ali Mohamedi.

December 2019

Abstract

Development of medical devices for osteoarthritis diagnosis, antimicrobial, wound closure, and wound pH milieu monitoring

The University of Texas at Arlington, 2019

Supervising Professors: Dr. Liping Tang, Dr. He Dong.

Nanotechnology has been widely used in the field of biomedical engineering. For example, nanoparticles have been employed for targeted drug delivery due to their retention effect, increased permeability, site-specific targeting, and avoiding phagocytosis as foreign materials. Moreover, nanotools, such as liposomes, Q-dots, dendrimers, micelles, and carbon nanotubes, have been developed for disease diagnosis and treatment. Generally, the application of nanotechnology can be categorized as follows: nanomedicine, tissue regeneration, biomarker/biosensors, nanorobots, and gene therapy. In the past four years, I have been focusing on developing nanotechnology for diagnosis and treatment of many diseases such as osteoarthritis, open wound, and infection. Based on the work I have done, I published two articles in peer reviewed journals and had one manuscript in submission. All the abovementioned works are summarized in the following chapters.

Chapter 1: **Li S**, Cong W, Hakamivala A, Huang Y, Borrelli J Jr, Tang L. Hyaluronic Acid-Based Optical Probe for the Diagnosis of Human Osteoarthritic Cartilage. *Nanotheranostics* 2018; 2(4):347-359.

Chapter 2: Chen W, **Li S**, Renick PJ, Yang S, Pandey N, Boutte C, Nguyen KT, Tang L, Dong H. Bacterial Acidity-Triggered Antimicrobial Activity of Self-assembling Peptide Nanofibers. *Journal of Materials Chemistry B*. 2019; 7(18):2915-2919.

Chapter 3: **Li S**, Zhou J, Huang Y, Roy J, Zhou N, Yum K, Sun X, Tang L. Injectable Click Chemistry-based Bioadhesives for Accelerated Wound Closure. *Acta Biomaterialia*. 2019 (under review).

Chapter 4: **Li S**, Vu H, Senkowsky J, Hu W, Tang L. A near infrared fluorescent pH indicator film for wound milieu pH monitoring. *Experimental Dermatology*. 2019.

Motivations

Nanotechnologies have served human's healthcare from many aspects. For example, nanomedicines take advantage from nanoparticle-based drug delivery system and have gained great success in cancer treatment which requires the precise targeting function. Tissue regeneration technology utilizes nanomaterial-based implants to replace and to repair injured at a small scale. Various nanoprobes have been developed to target cancer surface markers for cancer diagnosis and treatments. Nanorobots, an advanced technology employing nanometer-sized machine, have been applied for specified therapeutic action at the sites that are unavailable for conventional surgical intervention. Nanoparticles-based gene vectors have been developed for efficient gene therapy by overpassing blood brain barrier and increasing cellular internalization of nucleic acid through specific surface coating. Therefore, it is super encouraging for us to use the nanotechnology to solve problems associated with human's diseases in a biomedical engineering manner.

In the past four years, my research has been focusing on how nanotechnology can be developed for new applications for many diseases such as osteoarthritis, open wound, and infection. Specifically, my thesis documents my contributions to the development of these new technologies, including a new imaging nanoprobe to detect early stage of osteoarthritis (Chapter 1), acidic environment triggered smart antimicrobial self-assemble nanofibers (Chapter 2), nano-surgical bioadhesive (Chapter 3), and nano probe-embedded wound dressing for wound pH monitoring (Chapter 4). The motivation and accomplishment of the work are summarized in the following chapters.

Treatment to osteoarthritis at an early stage (or cellular level) is generally considered as impossible due to lacking the diagnostic tool. It is well established that early diagnosis and

treatment may produce the best therapeutic outcomes. Therefore, there is a great need to develop a diagnostic tool. Such goal may be achieved by the development of nanoprobes to target inflammatory cell accumulation often associated with early stage of osteoarthritis. In Chapter 1, a hyaluronic acid-based optical probe was designed and fabricated for the diagnosis of early stage osteoarthritic cartilage. The probe was fabricated using hyaluronic acid (HA) particles conjugated with near-infrared dye and folic acid (FA). Using human articular cartilage, we verified the existence of activated macrophages on osteoarthritic cartilage with highly up-regulated expression of folate receptors. In addition, we found that FA-HA probes had higher binding amounts to osteoarthritic tissue than healthy ones. Finally, the co-localization of the imaging probe, folate receptors and cartilage degeneration on the tissue sections indicated the extraordinary accuracy and efficiency of this osteoarthritis diagnostic probe.

Antimicrobial peptides have been widely used as an efficient approach to treat bacterial infection. However, due to their systemic toxicity and instability, antimicrobial peptides cannot be used in many clinical applications. To overcome such drawbacks, there is a need on the development of stable antimicrobial peptide nanoclusters which only release antimicrobial peptides at the site of infection. In Chapter 2, a self-assembling nanofiber (SAN) was developed to sense the microenvironmental pH change associated with bacterial growth. The SANs are supramolecular assemblies of multidomain peptides which are buried inside the assembly under physiological condition and disassemble at the bacterial colonization site with an acidic pH. Our results show that such strategy can significantly reduce the peptide cell toxicity and hemolytic activity due to the perfect stability under physiological condition while produce an impressive antimicrobial effect induced by acidic environment at the site of *B fragilis*.

Tissue adhesives have been widely used in wounds closure to replace the traditional suturing approach due to the decreased foreign body reactions and no need for further removal. However, many of the existing commercial tissue adhesives have their individual flaws upon application. Therefore, tissue adhesives with strong adhesion strength, biodegradability, low cytotoxicity, and can be applied on a wet surface remain highly desirable. In Chapter 3, an injectable click chemistry-based bioadhesive was developed for accelerated wound closure. Briefly, by taking advantage of the fast and specific inverse-demand Diels-Alder cycloaddition reaction, copper-free click chemistry pair trans-cyclooctene /tetrazine was employed in the chitosan to produce bioadhesives for the first time. The gelation time of the bioadhesives can be adjusted to less than 2 minutes which perfectly meets the need for surgical wound closure in practice. With the adding of 4-arm polyethylene glycol propionaldehyde (PEG-PALD) as a co-crosslinker, the adhesive strength of the bioadhesives can be optimized to be 2.7 times higher than that of the conventional fibrin glue. The chitosan bioadhesives stand out with excellent cytocompatibility and the cytotoxicity of their degradation product is also minimal. Through a mice incision wound model, we proved that the chitosan bioadhesives can close the wound faster and promote the wound healing process compared with the fibrin glue. In conclusion, our results support the innovative chitosan bioadhesives to be highly translational and can be widely applied for multiple types of wound closure in the wound management.

Prognosis of wound healing is a key to design treatment plan for physicians. Currently, wound healing process is generally monitored through visual observation, such as using Bates-Jensen Wound Assessment Chart and wound measuring tools. However, this approach can be experience dependent and not precise due to the complicated environment that exists in the chronic wounds. While it is well established that wound pH is an important indicator of wound healing

status, there is no diagnosis tool that have been developed for wound pH monitoring. Our previous study has fabricated a ratiometric imaging nanoprobes for pH detection. By taking advantage of this early work and as described in Chapter 4, pH nanoprobes were used to fabricate a ratiometric film for measuring pH of wound milieu. The ability of this film to monitor wound pH was assessed using simulated wound fluids and wound exudates soaked onto discarded wound dressings. *In vitro* tests showed that the film can accurately and rapidly detect a wide range of pH (from pH 4 to 8) in wound milieu. Further, wound dressing studies showed that the newly fabricated pH sensing films can indirectly reveal wound alkalinity by measuring pH on wound contact side of discarded wound gauze. By comparing patients with different wound conditions, we find that the pH sensing film can be used to measure wound exudate pH with high accuracy and efficiency. Equally important, this diagnostic may serve the first wound diagnosis tool which can provide an accurate and real-time assessment of healing activity in chronic wounds.

Table of Contents

Chapter 1. Hyaluronic Acid-Based Optical Probe for the Diagnosis of Human Osteoarthritic Cartilage

Shuxin Li,[1] Wei Cong,[1,2] Amirhossein Hakamivala,[1] YiHui Huang,[1] Joseph Borrelli, Jr,[1] Liping Tang[1,3]*

1. Department of Bioengineering, University of Texas at Arlington, Arlington, TX 76019, USA
2. Department of Oral Anatomy, College of Stomatology, Dalian Medical University, Dalian, Liaoning, 116044, China
3. Department of Biomedical Science and Environmental Biology, Kaohsiung Medical University, Kaohsiung 807, Taiwan

* Corresponding author. Department of Bioengineering, University of Texas at Arlington, P.O. Box 19138, Arlington, TX 76019-0138, USA. Tel.: +1 817 272 6075; fax: +1 817 272 2251. E-mail address: ltang@uta.edu.

Abstract

Osteoarthritis is typically caused by cartilage injury, followed by localized inflammatory responses and tissue deterioration. Early treatment of osteoarthritis is often impossible due to the lack of diagnostic options. Recent studies have supported that different imaging probes can be used for arthritis detection in mice. However, none of these diagnostic tools have been tested on human articular cartilage. To fill this gap, an optical imaging probe was developed to target activated macrophages and the accumulation of imaging probes on tissue was used to assess the severity of human osteoarthritis.

Methods: The probe was fabricated using hyaluronic acid (HA) particles conjugated with near-infrared dye and folic acid (FA). The ability of the FA-HA probes to detect activated macrophages and quantify cartilage injury was evaluated using a cell culture model *in vitro* and human osteoarthritic cartilage explants *ex vivo*.

Results: Our cell study results supported that the FA-HA probes are cell compatible (up to 0.5mg/mL) and can detect activated macrophages in 30 minutes. Using human articular cartilage, we verified the existence of activated macrophages on osteoarthritic cartilage with highly up-regulated expression of folate receptors (~13 folds by comparison with healthy control). In addition, we found that FA-HA probes had higher binding amounts (~3 folds) to osteoarthritic tissue than healthy ones. Histological analyses confirmed that there was a strong linear relationship (R=0.933) between the fluorescent intensity of tissue-associated probe and the extent of folate receptors on osteoarthritic cartilage. Finally, the co-localization of the imaging probe, folate receptors and cartilage degeneration on the tissue sections indicated the extraordinary accuracy and efficiency of this osteoarthritis diagnostic probe.

Conclusions: Our results support the probe as an effective diagnostic tool to detect the area and severity of osteoarthritic human articular cartilage.

Keywords: osteoarthritis; diagnosis; optical probes; hyaluronic acid; folate receptor; human explant.

1. Introduction

Osteoarthritis has become a major cause of disability in the United States responsible for a tremendous sociological and economic burden [1, 2]. Early diagnosis and treatment of osteoarthritis is believed to delay disease progression and improve the patient outcome [3]. According to the Arthritis Foundation, osteoarthritis may be diagnosed by a physical examination, followed by confirmation with joint aspiration, X-ray and Magnetic Resonance Imaging (MRI) [4-6]. Unfortunately, joint aspiration and X-ray imaging are unreliable and cannot be used to detect localized cartilage injury before any structural damage emerges [7, 8]. MRI is comparatively sensitive, valid and reproducible for assessing whole-joint structures including cartilage degeneration, subchondral bone marrow lesions, joint effusion and synovitis [9]. However, MRI is unable to detect localized cartilage tissue deterioration which is often associated with the early onset of osteoarthritis [10]. Therefore, there is a need for the development of new methods to assess localized cartilage damage of osteoarthritis.

Increasing evidence supports that synovial macrophages play an important role in the progression of osteoarthritis [11-13]. Firstly, the accumulation of macrophages at the synovial lining and cartilage surfaces is the first symptom of osteoarthritis [11]. Secondly, macrophages are the most prevalent cells that infiltrate in a human osteoarthritic joint, accounting for 65% of all infiltrating cells [14]. Thirdly, a recent study has shown that activated synovial macrophages enhance osteophyte formation, fibrosis and many signs of osteoarthritis [15]. Fourthly, inflammatory cytokines released by activated macrophages, such as TNF-α and IL-1β, have been shown to promote the inflammatory and destructive responses in osteoarthritis [12]. Lastly, the critical role of macrophages in osteoarthritis progression is confirmed in a study that shows that the depletion of synovial macrophages results in a significant reduction of osteophyte and fibrosis

formation in a murine osteoarthritis model [15]. These results suggest that the detection of activated macrophages is a reliable indicator for assessing the severity and location of osteoarthritis.

The folate receptor (FR) is a family of glycosyl phosphatidylinositol–anchored proteins and has high affinity for FA [16]. Beta form of FR (FRβ) is specifically expressed on activated macrophages in inflamed joints and has been used as a target for drug delivery [17, 18] based on several unique characteristics of the FR. Firstly, expression of FR can only be found on activated macrophages but no other blood cells such as lymphocytes, granulocytes or erythrocytes [19]. Secondly, increased amount of FR is present on activated macrophages in the inflammatory environment but not on quiescent resident macrophages [20]. Finally, folate targeting near infrared probes were found to able to assess the disease progression of LPS induced arthritis mice model by quantifying the extent of active macrophage accumulation in the joints [21]. These results support that folate probes can be developed to detect the presence of activated macrophages on osteoarthritic cartilage via FR-folate interaction.

Several imaging modalities have been investigated on their ability to detect activated macrophages during the progression of rheumatoid arthritis and osteoarthritis. Using single-photon–emission computed tomography, a study demonstrated that a diethylene triaminepenta acetic acid (DTPA)–folate probe can be fabricated to monitor the macrophage accumulation in joint tissue of rat osteoarthritis models [22]. Folate-conjugated ^{99m}Tc chelator was also studied to monitor macrophage recruitment using gamma scintigraphy in a rat RA model [23]. Lastly, a formyl peptide receptor 1-targeting peptide probe cFLFLF-PEG-^{64}Cu was investigated for its ability to detect activated macrophages in an induced osteoarthritis rat model via positron emission tomography imaging [13]. While these nuclear medicine methods can detect the accumulation of

activated macrophages at the site of arthritis, the risk of radiation exposure limits their use for routine osteoarthritis diagnosis.

To overcome this limitation, other optical imaging methods have been investigated for arthritis diagnosis. For example, a FR-targeting near infrared (NIR) probe was developed to detect activated macrophage recruitment in mice with induced rheumatoid arthritis [21]. Another study has shown that NIR dye (Cy5.5 fluorochrome)-conjugated anti-macrophage antibody (anti-F4/80 antibody) can be used to visualize the presence of a higher number of macrophages at a joint with induced osteoarthritis in mice [24]. Despite all these observations, none of these probes have been evaluated on their capability to diagnose human osteoarthritic cartilage tissue in human, which was the focus of this investigation.

In this study, we fabricated FR-targeting probes by conjugating NIR dye and folic acid onto hyaluronic acid (HA) particles. HA, a natural polymer with inherently biocompatible and biodegradable properties, has been widely used as a drug carrier [25, 26] and imaging probe [27]. The physical, chemical and cellular compatibility of the probes was characterized. The ability of the FA-HA probes to detect and quantify the number of activated macrophages was investigated *in vitro*. Finally, using discarded human cartilage tissue, we determined the effectiveness of FA-HA probes for identifying the area of osteoarthritic tissue and assessing the extent of osteoarthritic degeneration in human osteoarthritic explants.

2. Materials and methods

2.1 Materials

HA (sodium salt, 700KDa) was obtained from Lifecore Biomedical (Chaska, MN). Divinyl sulfone (DVS, 97%), 1-heptanol (98%) and folic acid (FA, ≥97%) were obtained from Sigma-

Aldrich (St. Louis, MO). Dioctyl sulfosuccinate sodium salt (AOT, 96%) and isooctane (99%) were obtained from Fisher Scientific (Hampton, NH). Polyethylene glycol $(NH_2)_2$ (HCl salt, 5000 Da) was purchased from Jenkem Technology (Beijing, China). N-Hydroxysuccinimide (NHS) and 1-Ethyl-3-(3-dimethylaminopropyl) carbodiimide were obtained from Thermo Scientific (Rockford, IL). CF647A amine dye was purchased from Biotium, Inc. (Fremont, CA).

2.2 Fabrication of FA-conjugating HA probes

HA particles were synthesized via a water-in-oil microemulsion process as described earlier with minor revisions [28]. Briefly, 3 mL of HA aqueous solution (1.5wt% in 0.2M NaOH) was added dropwise into an oil phase solution composed of 50 mL of isooctane, AOT (0.2M) and 1-heptanol (0.04M) under homogenization at 28,000 rpm (OMNI GLH homogenizer, OMNI international, GA). Divinyl sulfone (0.015M) was added dropwise into the polymer solution and homogenized at 28,000 rpm for 5 minutes. The reaction then proceeded under vigorous stirring (2,200 rpm) at ambient temperature for 1 hour. Following the addition of 3 mL of hydrochloric acid (0.2M) to stop the reaction, the HA particles were collected by precipitation in 80 mL of acetone and sequentially washed with acetone, ethanol and water. After removal of large (micron-sized) particles via centrifugation 2x at 6 x g for 10 minutes, nano-sized particles were collected by centrifugation at 805 x g for 10 minutes, and the collected nanoparticles were lyophilized and stored at 4^{o}C for further use.

HA particles were conjugated with fluorescent dye as described previously [29]. Briefly, HA particles (50mg/mL, PBS pH=6.0) were incubated with EDC (0.66M) and NHS (0.66M) at room temperature for 24 hours. The activated HA particles were collected by centrifugation at 805 x g for 10 minutes. The activated HA particles were dispersed in PBS (pH=7.2) containing CF647A

amine dye (1.2mM) and allowed to react for 24 hours in dark. CF647A-labeled HA particles were purified via the centrifuge. Absorptive and fluorescent spectra of the CF647A-labeled HA particles were measured using an ultraviolet-visible spectrophotometer (Lambda 19 Spectrometer, Perkin Elmer, MA) and an Infinite M200 microplate reader (Tecan, San Jose, CA), respectively.

Some of the CF647A-labeled HA particles were further conjugated with FA to prepare FA receptor-targeting HA (FA-HA) probes. First, FA was modified with PEG $(NH_2)_2$ to introduce an amine group into FA [30]. Namely, FA (2.8mM) was activated by its overnight incubation in a solution of dimethyl sulfoxide (DMSO) containing EDC (4.2mM) and NHS (4.2mM) at room temperature; subsequently, PEG $(NH_2)_2$ (2.8mM) was incubated with the activated FA solution for 24 hours at room temperature in a dark setting to introduce a free amine group into the FA (FA-PEG-NH_2). FA-PEG-NH_2 was then purified with exhaustive dialysis (molecular cutoff: 2kDa) against DMSO and subsequently against water. The FA-PEG-NH_2 was lyophilized and stored at 4 ^oC for further use. To conjugate FA onto CF647A-labeled HA particles, 10 mg of CF647A-labeled HA particles, 6.6 mM of FA-PEG-NH_2 and 66 mM of EDC were dispersed in PBS (pH=4.5). After stirring overnight at room temperature, the FA-conjugated CF647A-labeled HA particles (FA-HA probes) were collected via centrifugation at 9,838 x g. The FA-HA probes were washed 3X with DI water, lyophilized and stored under dark conditions for future use.

2.3 Characterization of FA-conjugated HA probes

Particle size and particle size distribution were analyzed at a particle concentration of 0.33 mg/mL using a Photon Correlation Spectrometer and a ZetaPALS Particle Sizing software (ZetaPALS, Brookhaven Instruments Co., Holtsville, NY, USA). The morphology of the probes was observed by using a scanning electron microscope (Hitachi S-4800 II FE SEM, operating voltage 15 kV).

HA particles were firstly labeled with CF647 before FA conjugation. The conjugation efficiency of CF647A dye was determined based on an established method and equation: Conjugation efficiency = $(M_0\text{-}M_1)/M_{NP} \times 100\%$, where M_0 is the mass of initial input dye, M_1 is the mass of unconjugated dye and M_{NP} is the mass of the HA particles. [31] M_1 = (volume × absorbance at 648 nm × molecular weight of dye) / (path length × extinction coefficient of dye at 648nm) [32]. All experimental data is collected in PBS (pH=7.4). The absorbance (at 648 nm) was measured with a UV/VIS spectrophotometer (Beckman DU-640, Beckman Coulter, TX).

To determine the optical properties of the CF647A-labeled HA particles, 200μL of the probes in PBS (pH=7.4) (1mg/mL) was placed in a 96-well plate and fluorescence spectra were recorded using a SpectraMax Gemini XPS microplate reader (Molecular Devices, Sunnyvale, CA) [33].

To determine the FA conjugation efficacy on the probes, FTIR spectra of FA-HA probes were determined using a Nicolet 6700 FT-IR spectrometer (Thermo Nicolet Corp., Madison, WI) at a resolution of 8 cm^{-1} with a scan width of 4000-400 cm^{-1}. Conjugation efficiency of FA on probes (FA-PEG mass per milligram of the dried probes) was quantified based on the measurement of FA absorbance at 362nm as described previously [34].

2.4 Cytotoxicity assay of FA-HA probes

Cytotoxicity of the probes were evaluated using human chondrocytes (ATCC, Manassas, Virginia) as described earlier [35]. Briefly, cells were seeded in a 96-well plate at a density of 8×10^3 cells/well and incubated in chondrocyte medium (ATCC, Manassas, VA), which was supplemented with 10% fetal bovine serum (FBS) and 1% penicillin-streptomycin, for 24 hours in an incubator set at 5% CO_2 and 37℃. The seeded cells were incubated with different concentrations

of probe for 72 hours. The adherent cells were washed 3X with PBS (pH=7.4) and then incubated with 100 μL of media containing 10 μL of AlamarBlue® Cell Viability Reagent (Sigma-Aldrich) for 4 hours. A microplate reader (infinite 200, Tecan, Switzerland) was used to record the fluorescent intensities at an excitation of 540 nm and an emission of 590 nm. Cell viability was determined by the ratio of the fluorescent intensity of experimental group to the fluorescent intensity of control group (no probes added) × 100% [34].

2.5 In vitro macrophage targeting

Studies were carried out to illustrate the probes' ability to target activated macrophages using activated THP-1 cells, as described previously [34]. Briefly, human THP-1 monocytic cells (ATCC, 1.5×10^4 cells/mL/well in RPMI 1640) were incubated with phorbol 12-myristate 13-acetate (PMA, R&D system) (162 nM PMA for 48 hours) to produce activated macrophages [29]. FA-HA-CF647 probes (final concentration 0.5mg/mL) were then added into activated and naive THP-1 cells for 15 and 30 minutes. To determine the role of the probe's FA on macrophage targeting, a similar *in vitro* study was carried out, which entailed the incubation of activated THP-1 cells with an excess amount of FA (18μM) for 20 minutes prior to the supplement of FA-HA probes (final concentration 0.5mg/mL) or HA control particles. At the end of the study, macrophages were washed with fresh media 5X and cell-associated fluorescent intensity in each well was read with a microplate reader. In addition, confocal laser scanning microscopy certified the location of targeted probes on activated THP-1 cells. Specifically, activated THP-1 cells were incubated with either FA-HA probes (0.1mg/mL) or RPMI 1640 medium (as control) for 4 hours in 37°C. Cells were washed with PBS (pH=7.4) three times and then stained with DAPI for three minutes. Thus, the interaction between live cells and probes could be visualized with different

laser channels using confocal laser scanning microscopy (Leica TCS SP8 SMD, Leica, Buffalo Grove, IL, USA) at different channels: DAPI channel (Excitation: 400nm, Emission: 470nm, Exposure time: 200ms), Cy5 channel (Excitation: 647nm, Emission: 670nm, Exposure time: 800ms) and White light channel (Exposure time: 100ms).

Murine Raw 264.7 macrophage (ATCC, Manassas, VA) was the model cell used to assess the effectiveness of FA-HA probes in targeting inflammatory cells. Raw 264.7 macrophages were cultured in folate-free RPMI media containing 10% FBS at 37℃ until reaching 75% confluence. To up-regulate cell surface FR expression, cultured murine macrophages were activated by supplementing 1.0 μg/mL lipopolysaccharide (LPS) (from *E. coli*, Sigma, St. Louis, MO) for 4h, as shown in previous publications [36]. After LPS incubation, cells were washed 2X with RPMI to remove non-adherent cells. FA-HA probes (final concentration 0.5mg/mL in RPMI) and NIR-labeled control HA particles were co-cultured with different numbers of activated macrophages (12,500, 25,000, 50,000, and 100,000). After a 30-minute culture period, macrophages were washed with PBS (pH=7.4) buffer three times to remove free particles/probes. The extent of targeting efficiency was then quantified by measuring the fluorescent intensity at a 630 nm excitation wavelength and 690 nm emission wavelength using a microplate reader.

2.6 Ex vivo targeting of human arthritic cartilage explant

To assess the ability of FA-HA probes to target OA cartilage tissue, human articular cartilage was obtained from the discarded tissue of anonymous patients (N=4) undergoing total knee replacement and was stored at sterile saline at 4 °C for up for 24 hours prior to the experiments. As supported by previous publications [37] and our preliminary studies, the cartilage tissue used in the investigation possessed the histological characteristics and FA-HA probe affinity resembling

freshly isolated cartilage samples. Explants were isolated from the weight bearing area in lateral femoral condyles with different severities of osteoarthritis and dissected into the mean size in mm: 20.0 ± 3.3 (L) × 13.4 ± 2.9 (W). In addition, explants isolated from non-weight bearing area without apparent osteoarthritis injury was used as healthy controls. The explants were washed gently with sterile saline and then immersed in a 6-well plate containing 3 mL of saline. Different concentrations (final concentrations, 100 μg/mL and 20 μg/mL) of FA-HA probes and HA control were added into the well plate which was then placed on a constant shaker in a dark setting. Explants in the plate were imaged at various time points (30, 45, 75, 105 and 135 minutes) using a custom-made fluorescent imaging system, and the collected images were processed as described in our previous publication [38]. Data was plotted in terms of the mean intensity of Region of Interest (ROI) over time.

2.7 Histological analysis

After imaging, the explants were embedded in an OCT compound and then sliced into 5-μm sections. The sections were fixed in iced acetone (-20°C) for 5 minutes prior to histological staining. For double staining of FR and macrophages (CD68), the sections were incubated with FR antibody (1:50, Santa Cruz Biotechnology, Santa Cruz, CA, USA) and anti-CD68 antibody (1:80, Abcam, Cambridge, MA, USA) overnight at 4℃, followed by Alexa Fluor 594-conjugated anti-mouse IgG antibody (1:120, Abcam, Cambridge, MA, USA) and Alexa Fluor 488-conjugated anti-rabbit IgG antibody (1:120, Abcam, Cambridge, MA, USA) incubation for 1 hour at room temperature. A negative control was simultaneously generated by carrying out identical histological staining without the use of primary antibody. To reduce background staining caused by endogenous peroxidase activity and non-specific binding, all section staining was blocked with

3% hydrogen peroxide (10 minutes) and 5% purified goat serum (10 minutes), respectively. For the immunohistochemistry (IHC) staining, the sections were incubated with FR antibody (1:50, Santa Cruz Biotechnology, Santa Cruz, CA, USA) overnight at 4℃ and followed by HRP-conjugated anti-mouse IgG antibody (1:500, Abcam, Cambridge, MA, USA) incubation for 1 hour at room temperature. Diaminobenzidine (DAB, sigma, MO, USA) was used as a chromogen for color development and methyl green was used as counterstain. FR scores were calculated to quantify the degree of FR expression, based on a published study [39]. Briefly, A (number of positive cells) and B (intensity of staining, including: 0= no color reaction; 1 = mild reaction; 2 = moderate reaction, 3 = intense reaction) were counted. Final FR scores were then calculated based on the following formula: FR score =A × B [39]. To determine the relationship between probe binding amounts and FR scores, we divided the tissue sections into 29 regions/cross-sections. In each cross-section, we measured its associated NIR intensity and FR score. The linear relationship between each cross-section probe accumulation and FR scores was determined statistically.

2.8 Co-localization of probes and diseased human tissue

The probes' ability to detect osteoarthritic tissue was verified using histological methods, which involved determining the locations of probe accumulation and FR expression on human osteoarthritic tissue. Human osteoarthritic tissue incubated with probes (100 μg/mL for 2 hours) were cryosectioned into two consecutive sections. One section was used for staining FR expression. The second section was used for NIR imaging to visualize the probe distribution. Subsequently, the slide was stained with Safranin O to assess the severity of cartilage tissue degeneration on the surface of the osteoarthritic cartilage. The Safranin O staining was carried out as described earlier [40]. After the staining, the slice was scanned through a pathology slide scanner (PathScan Enabler

IV, Meyer Instruments, TX, USA). By merging NIR images and Safranin O images, we would be able to determine whether the probes preferentially accumulated on and diagnosed the location of the degeneration tissue.

2.9 Statistical analyses

All the results will be expressed as mean ± standard error (including FR score on osteoarthritic and healthy cartilage, normalized cell viability, fluorescence of cell targeting and fluorescence on human tissue images). Student t-test was performed to compare the difference between groups. A value of $p \leq 0.05$ was considered significant. Linear regression analysis was used to determine all calibration curves. The Pearson correlation coefficient (R) was calculated to measure the linear correlation between two variables.

3. Results

3.1 Folate receptor expression on human osteoarthritic tissue

Using histological analysis, the location of FR expression and macrophage accumulation on osteoarthritic tissue sections was determined. We found that abundant FR expression on the surfaces of osteoarthritic tissue coincided with the accumulation of macrophages (Figure. 1A). These observations supported that most of the macrophages on osteoarthritic tissue expressed FR. Furthermore, by comparison with healthy tissue, there was a substantially higher level of FR expression on osteoarthritic tissue (Figure. 1B). This finding concurred with the FR score results, in which osteoarthritic tissue FR scores were significantly higher than healthy tissue FR scores (Figure. 1B). These results support our overall hypothesis that FR-targeting probes can be

employed to diagnose the extent of inflammatory responses on human osteoarthritic cartilage tissue.

3.2. HA particle synthesis, separation and characterization

To fabricate FR-targeting probes, we first synthesized HA particles by an emulsion polymerization technique using an AOT/isooctane/H_2O emulsion system, while employing DVS as the crosslinker. The fabricated particles exhibited a wide range of particle sizes (Average size = 1161.1 nm, size variation = 89.8 nm). To narrow the particle size distribution, we applied a differential centrifugation method and collected a small size range of HA particles. DLS determined that the diameter of HA particles was ~490 nm (Figure. 2A). SEM images of the particles revealed the spherical shape of HA particles although the diameter of the particles reduced to ~200 nm due to dehydration during the process of sample preparation (insert Figure. 2A). The particles were then conjugated with a NIR dye - CF647A. The resultant NIR-labeled HA particles had a maximum absorbance peak at 654 nm and a maximum emission peak at 680 nm (Figure. 2B). The conjugation efficiency of CF647A on HA particles was 10.7 nmol CF647A per 1 mg of HA particles.

3.3 Characterization of FA-conjugated HA probes

Folate conjugation to HA particles was achieved through a succinimidyl ester-amine reaction between FA-PEG-NH_2 and HA particles. FTIR spectra of FA-HA probes, HA particles and FA confirmed the success of the conjugation process, since the peak of phenyl and pterin rings (1485~1519 cm^{-1}) [41], a unique marker of FA, appeared on the FTIR spectrum of FA-HA probes (Figure. 2C). Based on the absorbance of FA-HA probes and the calibration curve generated with

FA-PEG solution, we determined that the average conjugation efficiency of FA on HA particles was 120 nmol folate per 1 mg of HA particles.

3.4 Cytotoxicity of HA particles and FA-HA probes

The cytotoxicity of HA particles and FA-HA probes was determined using human chondrocytes. We found that HA particles had no detectable cytotoxicity up to 1 mg/mL (Figure. 2D). Similarly, FA-HA probes were found to have no detectable cytotoxicity up to 0.5 mg/mL (Figure. 2D). Based on these observations, both HA particles and FA-HA probes were used in subsequent studies in media with concentrations <0.5 mg/mL.

3.5 FA-HA probes targeting efficiency on activated macrophages

The ability of FA-HA probes to detect activated macrophages was investigated using both Murine Raw 264.7 macrophage and human THP-1 cell lines. We first examined the interactions between probes and activated THP-1 cells using fluorescence microscopy (Figure. 3A). Cy5 and DAPI images were taken to reveal the location of FA-HA probes and macrophages, respectively. By overlaying both Cy5 and DAPI images, we clearly saw a large number of FA-HA probes on the surfaces of activated macrophages, which would directly support the targeting process. By measuring cell-associated fluorescent intensities at different time points (15 and 30 minutes), we found that FA-HA probes had a significant higher specificity to activated macrophages (~10X) than to naïve cells (Figure. 3B). Additionally, the amounts of probes accumulated on activated macrophages in 15 minutes are only slightly less than those in 30 minutes (Figure. 3B). To determine the role of FA on probes in targeting activated macrophages, a competition-binding test was performed in which free folate molecules were incubated with activated macrophages prior to

the addition of FA-HA probes. As expected, prior incubation of free FA (18μM) significantly reduce (~67%) FA-HA probe affinity to activated macrophages. These results support that probe accumulation on activated macrophages was mediated by the interaction between FA on probe and FR on inflammatory cells (Figure. 3C).

To explore the idea about whether probes could be used to quantify the numbers of activated macrophages, different numbers of activated Murine Raw 264.7 macrophages (treated with LPS) were incubated with FA-HA probes and control particles. After incubation for 30 minutes, we then assessed the probes' binding affinity by measuring the cell-associated fluorescent intensities. In agreement with earlier results, we found that there was a strong linear relationship between the number of activated macrophages and FA-HA probe associated fluorescent intensity (R=0.993) (Figure. 3D). The FA-HA probes' binding affinity to activated macrophages was calculated to be 7.00±1.91 ng/cell. On the other hand, there was only a small amount of the control particles associated with activated macrophages. These results agreed with our hypothesis that FA-HA probes can be used to detect and quantify activated macrophages.

3.6 Imaging efficiency on human osteoarthritic cartilage

Using human osteoarthritic cartilage tissue, we then investigated the ability of FA-HA probes to detect activated macrophages on human osteoarthritic cartilage explants *ex vivo*. Specifically, osteoarthritic tissue was first incubated with different concentrations (100 vs 20 μg/mL) of FA-HA probes and HA particles for different periods of time (30, 45, 75, 105 and 135 minutes) and then imaged using an NIR imager (Figure. 4A). Interestingly, shortly after incubation with FA-HA probes, we saw an uneven fluorescent signal distribution on osteoarthritic tissue. Based on the average fluorescent intensity acquired from the randomly picked ROI, we find that

FA-HA probes reach their peak targeting efficiency as early as 30 minutes (Figure. 4B). In general, the average intensity of the 100 μg/mL group was about 2.5 X higher than the intensity of the 20 μg/mL group. Moreover, the amount of FA-HA probes associated with human OA cartilage was about 2.6 and 2.3 folds more than that of control HA particles at the concentrations of 100 and 20 μg/mL, respectively. These findings supported that a higher administration dose contributed to a better imaging capability *in vitro* and the probes had a significant better targeting efficiency than control HA particles.

3.7 Quantification of folate receptor expression on human osteoarthritic tissue.

OA is associated with a varying degree of inflammatory responses at different areas of cartilage tissue. Under white light, osteoarthritic cartilage tissue showed slightly opaque, rough and yellowed surfaces (Figure 5A). In addition, the extent of inflammatory responses on different areas of cartilage tissue could not be easily identified by naked eyes. However, using FA-HA probes and NIR imaging, we could easily identify the area of extensive inflammatory responses on human cartilage tissue (Figure 5B). To assess the relationship between probe binding amounts and FR scores on cartilage tissue, we divided each tissue sections into 29 regions across the whole section. For each region, we determined the intensities of tissue associated probes (via NIR imaging) (Figure 5B) and the extent of FR expression (via FR scores) (Figure 5C). Using statistical analysis, we found a linear relationship between the NIR signal intensities and FR scores (Figure. 5D). Through the regression analysis, probe fluorescent intensity was found to have a strong correlation with the FR number (Mean probe intensity = 104.25 × FR number -37.066, R = 0.933). The statistical results of this experiment supported our hypothesis that FA-HA probes can be used to assess the severity of human OA cartilage.

3.8 Co-localization of FA-HA probes and FR expression and cartilage tissue degeneration

We further determined the FA-HA probes' ability for OA diagnosis by using confocal laser scanning microscopy and histological analysis to examine the probe distribution and degenerative cartilage tissue, respectively. As present in the stitched images, the probe distribution can be visualized clearly on the surface of the osteoarthritic cartilage sample (Figure. 6A). To determine the extent of cartilage degeneration, we used both FR IHC and Safranin O staining. The FR IHC stain imaging revealed a heterogeneous surface structure, indicating the degenerative nature of the OA tissue (Figure. 6B). Safranin O staining has been widely used to quantify proteoglycan content and to reflect the extent of cartilage degeneration. As anticipated, the Safranin O staining revealed the location and extent of cartilage degeneration (Figure. 6C). Impressively, the highest fluorescent intensity was located exactly at the most degenerated area, which means the probes were able to indicate the area of degenerative cartilage tissue through a specific targeting process.

4. Discussion

In the present study, FA-conjugated HA probes were fabricated and investigated for their ability to diagnose inflammatory responses on human osteoarthritic cartilage explants. Our results support that FA-HA probes can be used to detect activated macrophages via NIR imaging. In addition, probe-associated fluorescent intensities can be measured to reflect the number of activated macrophages in culture. By applying FA-HA probes (100 μg/mL) on cartilage tissue, we can visualize the extent of inflammatory responses on cartilage tissue within 30 minutes in the presence of free probes. Even though Osteoarthritis Research Society International (OARSI)

histological scoring has been widely used to determine the overall knee joint damage, OARSI scores can only reflect an average cartilage tissue injury and cannot be used to identify the areas of injured cartilage. We believe that the FA-HA probes can be used to identify localized cartilage injury by taking advantage of an intra-articular imaging technique established earlier [42].

The results of this work supports that FR can be used as a targeting ligand for OA diagnosis in humans. It should be noted that several different probes with different targeting ligands have been developed for *in vivo* OA diagnosis recently. Firstly, cathepsin B, an extracellular cysteine protease, was used as a marker of OA. Specifically, cathepsin B sensitive NIR probes were fabricated and then investigated for early OA diagnosis [43]. Secondly, fluorescence resonance energy transfer MMP-13 fluorogenic probes were fabricated and investigated for *in vivo* OA detection [44]. Thirdly, ApoPep-1 (CQRPPR), a peptide that is able to bind to apoptotic and necrotic cells, was tested for its ability to detect OA *in vivo* via its binding to apoptotic chondrocytes [45].

Different imaging modalities have been investigated for OA diagnosis with different advantages and disadvantages. For example, an investigational folate receptor-targeting companion imaging agent, 99mTc-folate (Etarfolatide), has recently been used to assay the participation of activated macrophages in a substantial proportion of human osteoarthritic knees using SPECT-CT [46]. However, the imaging method is invasive, causes negative side effects due to the imaging agent [47] and the bioavailability provided by intravaneous injection is low for articular cartilage due to the avascular structure, which leads to insufficient imaging information for diagnosis [48]. Conversely, our probe is fabricated with HA, which has been approved by the United States Food and Drug Administration for intra-articular injection since 2001 [49, 50]. Despite the improved penetration depth of NIR imaging [51], it is possible that the accumulation

of FA-HA probes on cartilage tissue cannot be detected non-invasively. In that case, a fluorescence arthroscope may be used to image the probe accumulation on cartialge tissue *in situ,* which has been documented recently [52].

HA is selected for this application based on the following advantages: first, HA has been used in the form of particles and tissue scaffolds for enhancing cartilage tissue repair and regeneration [53]; Second, studies have shown that HA is able to mediate chondrocyte proliferation and matrix synthesis in a cartilage microenvironment through the CD44-HA pathway [54]; and finally, HA may diminish immune responses by reducing the motility of lymphocytes [55], which would lead to inhibition of PMN leukocyte migration [56] and neutrophil aggregation and adhesion [57]. These unique characteristics may permit the further development of FA-HA probes into a treatment method that induces chondrogenic tissue regeneration and healing in osteoarthritic cartilage tissue. It should be noted that many other biocompatible, water soluble and biodegradable polymers have been developed as *in vivo* imaging probes [58]. For example, Poly(ethylene glycol) [59], Poly (L-glutamic acid) [60] and N-(2-Hydroxypropyl) methacrylamide [61] with various functional groups have been used to fabricate probes with different targeting and therapeutic moieties. It is possible the FR-targeting probes can be made using different polymer carriers. However, further studies are needed to determine the potential effects of polymer types on probe-cell interactions and affinity.

5. Conclusion

FA-targeting and NIR-labeled HA probes have been successfully designed to target FR-upregulated cells in culture and on human osteoarthritic tissue explants. These probes were characterized to be spherical, nanoscale and non-cytotoxic; in addition, they exhibited a strong

targeting efficiency on FR upregulated macrophages. Furthermore, by adding the probes in the solution, we can not only visualize the area but also the extent of inflammatory and degenerative cartilage tissue in 30 minutes *ex vivo*. Our results support that this imaging probe has a tremendous potential to be used as a novel diagnostic method to evaluate OA in a clinical setting.

Abbreviations

OA: osteoarthritis; HA: hyaluronic acid; FA: folic acid; FR: Folate receptor, MRI: magnetic resonance imaging; TNF-α: tumor necrosis factor alpha; IL-1β: Interleukin 1 beta; NIR: near infrared; DVS: Divinyl sulfone; AOT: dioctyl sulfosuccinate sodium salt; NHS: N-hydroxysuccinimide; EDC: 1-Ethyl-3-(3-dimethylaminopropyl) carbodiimide; PBS: phosphate buffered saline; FTIR: fourier-transform infrared spectroscopy; FBS: fetal bovine serum; PMA: phorbol 12-myristate 13-acetate; LPS: lipopolysaccharide; ROI: Region of Interest; IHC: immunohistochemistry; DLS: dynamic light scattering; SEM: scanning electron microscope.

Acknowledgement

This work was partially supported by a Research & Scholarship Excellence Gift and a Translational Research Award No. W81XWH-14-1-0459 from the Defense Health Program through the Department of Defense Peer Reviewed Orthopaedic Research Program. Opinions, interpretations, conclusions and recommendations were those of the authors and are not necessarily endorsed by the Department of Defense.

Competing Interests

The authors have declared that no competing interest exists.

Figure Legends

Graphical abstract

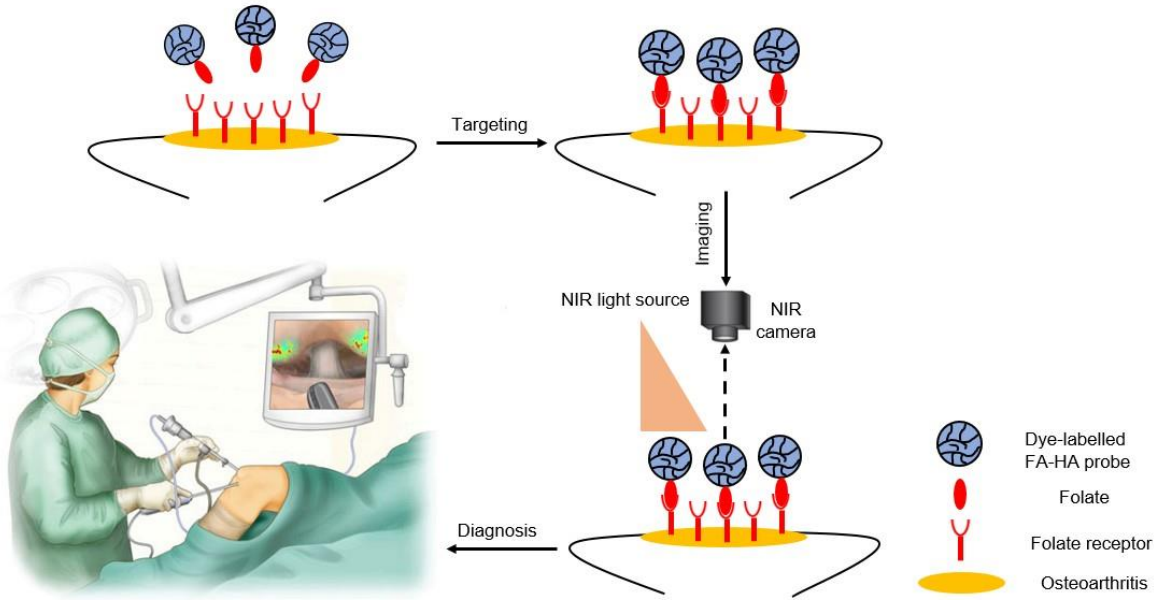

Figure 1

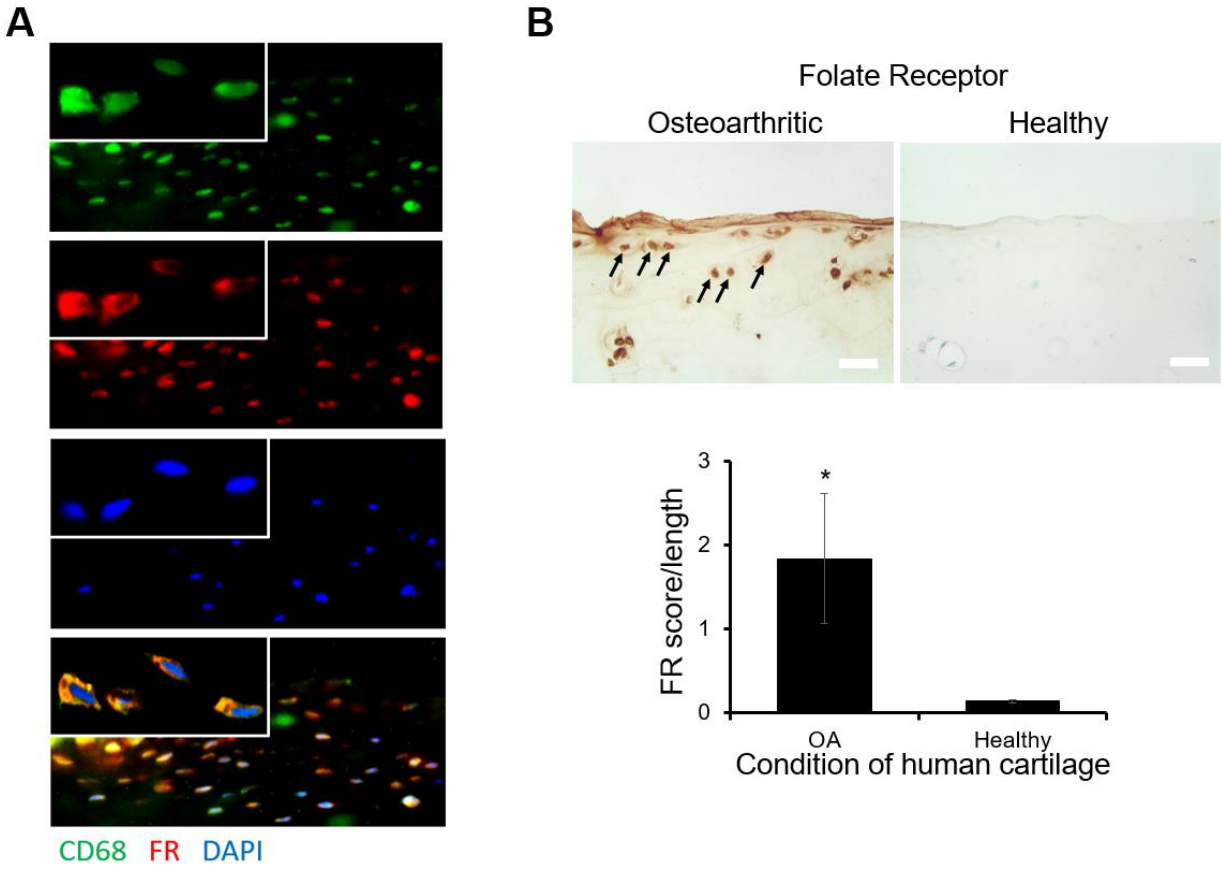

Figure 1. Preliminary histological study on human osteoarthritic tissue **(A)** Double staining images of folate receptor (FR: Cy3 channel-red) and macrophages (CD68: GFP channel-green, nucleus: DAPI-blue) on human osteoarthritic tissue were taken under 200X and 630X (inserted, oil immersion lens). **(B)** The expression of FR on osteoarthritic tissue was compared with FR expression on healthy tissue and arrows indicated positive staining result (scale bar: 0.1 mm). All the statistical data was presented as mean ± standard deviation, n=8 for OA tissue and n=3 for healthy tissue. Student t-test was performed to compare the difference between groups (including significance between FR score over length of OA and healthy tissue. A value of *$p \leq 0.05$ was considered significant.

Figure 2

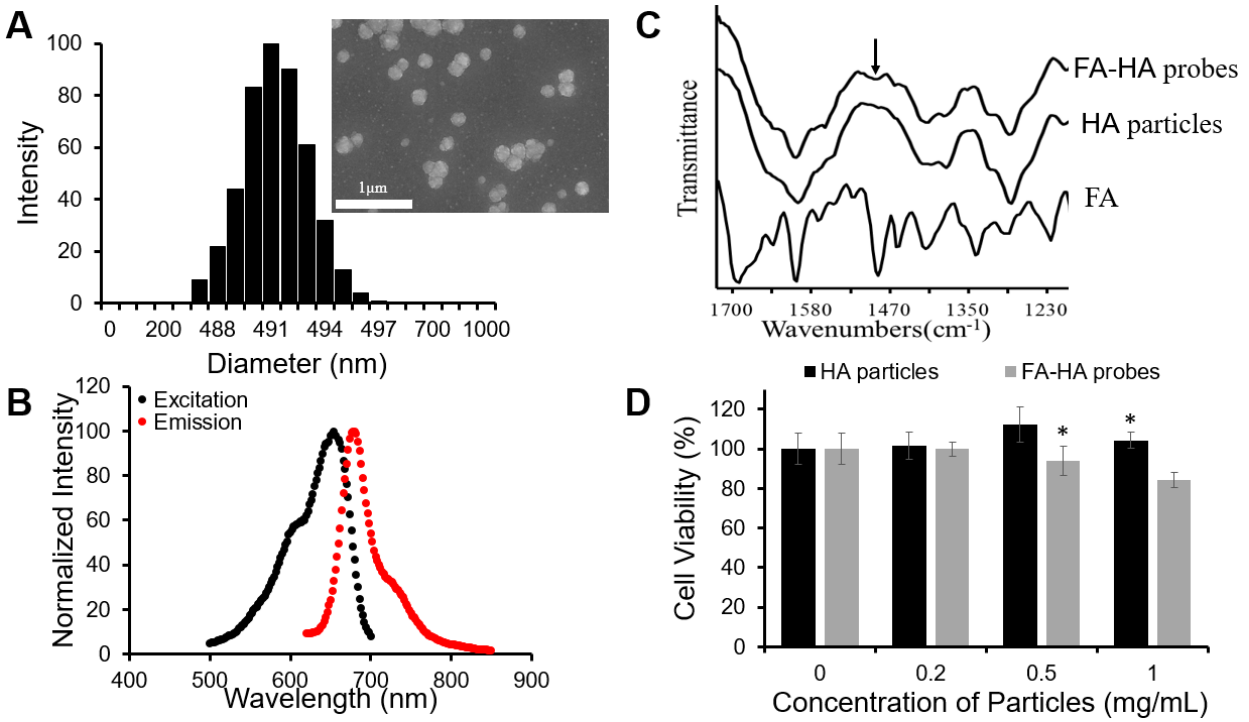

Figure 2. Physical and chemical characterizations of the probes. **(A)** HA particle size distribution was determined using DLS and particle morphology was observed with SEM (scale bar: 1μm). **(B)** The optical properties of the CF647A-labeled FA-HA probes were determined using a microplate reader. (C) Fourier transform infrared spectra of the FA, HA particles and FA-HA probes were employed to confirm the conjugation process. The arrow notes the peak of the phenyl and pterin rings (1485~1519 cm^{-1}). (D) Chondrocyte cytotoxicity study was carried out using HA particles and FA-HA probes. All the statistical data was presented as mean ± standard deviation, n=3 for each group. Student t-test was performed to compare cytotoxicity of different probe concentrations with the control group. * $P \leq 0.05$: Significance vs. the same materials (either HA particles or FA-HA probes).

Figure 3

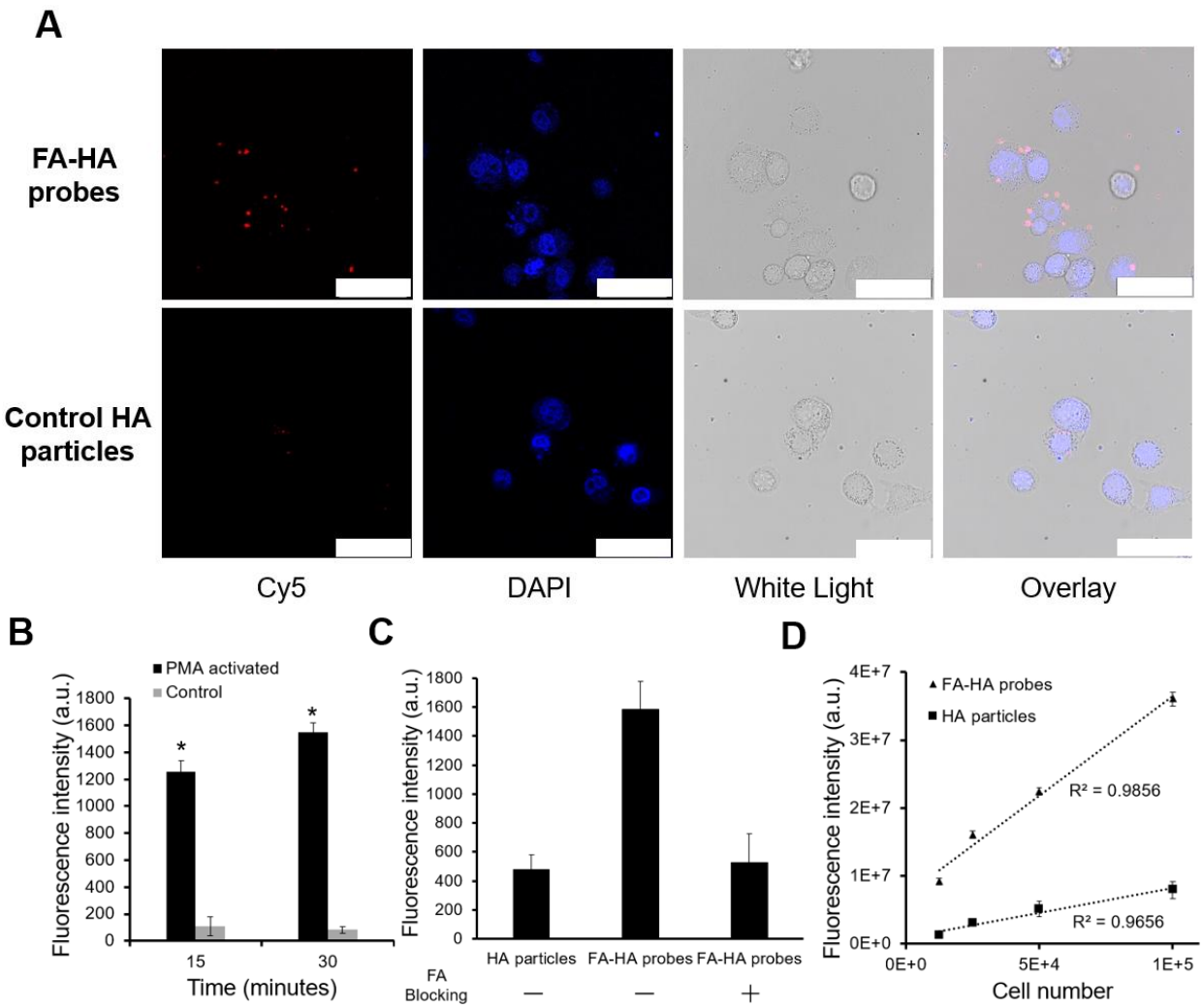

Figure 3. *In vitro* evaluation of the FA-HA probe's ability to target both activated human THP-1 cells (Figure 3A&B&C) and Murine Raw 264.7 macrophages (Figure 3D). **(A)** Fluorescent and white light images of activated macrophages treated with FA-HA probes and control HA particles at different channels - Cy5 channel (probes/particles), DAPI channel (macrophages), white light channel and overlay channel (scale bar: 50 μm). **(B)** Fluorescent intensities of PMA activated macrophages and naïve macrophages after incubation with FA-HA probes for 15 and 30 minutes. **(C)** Fluorescent intensities of HA particles or FA-HA probes on activated macrophages with or without the pre-treatment of free FA (18 μM) for 30 minutes. **(D)** The relationship between the number of activated Raw 264.7 macrophages and fluorescent intensities of cell-bound FA-HA probes/HA particles. All the statistical data was presented as mean ± standard deviation, n=3 for all groups. Pearson correlation coefficients were calculated between cell numbers and cell associated fluorescent intensities. A value of *$p \leq 0.05$ was considered significant.

Figure 4

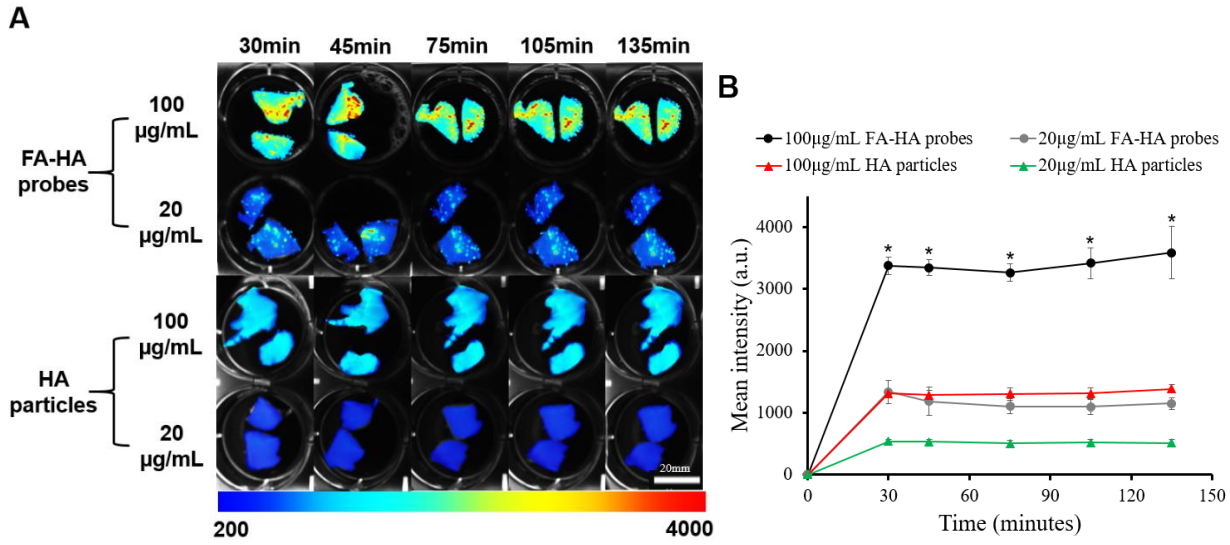

Figure 4. The ability of FA-HA probes to diagnose injured cartilage was evaluated using human osteoarthritic tissue *in vitro*. **(A)** Time and dose dependent fluorescent images of osteoarthritic human tissue co-cultured with different concentrations of FA-HA probes and HA particles (as control) (scale bar: 20mm). **(B)** The fluorescent intensities of all tissue incubated with different concentrations (20 and 100 µg/ml) of FA-HA probes and HA particle controls for different periods of time (up to 140 minutes) were calculated and compared. n=6 for all groups. The background fluorescence intensity of the HA particle control incubated tissue was 360±17. A value of *$p \leq 0.05$ was considered be significant.

Figure 5

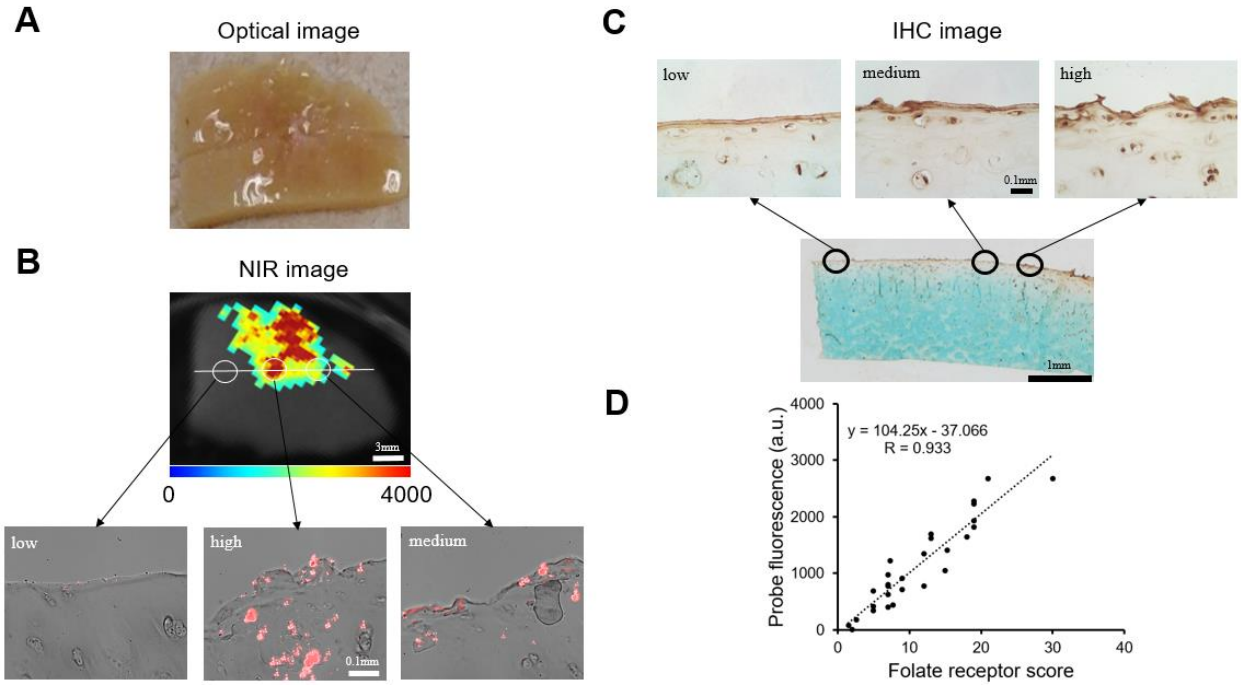

Figure 5. Relationship between fluorescent imaging and histological analysis results. **(A)** Optical image of human osteoarthritic tissue before OCT embedding. **(B)** Top panel: NIR fluorescent image of human osteoarthritic tissue taken after being incubated with FA-HA probes for 30 minutes. Bottom panel: probe incubated tissue was divided into 29 sections and then imaged using confocal laser scanning microscopy. Representative images of low, medium and high amounts of probe accumulation on tissue. (**C)** Top panel: representative images of FR IHC stained tissue with low, medium and high folate receptor scores. Images were taken under 200X microscope. Bottom panel: whole tissue image was taken using PathScan. **(D)** The linear relationship between tissue associated fluorescent intensities in each region and corresponding folate receptor scores on human osteoarthritic tissue were determined statistically with a Pearson correlation coefficient of 0.933.

Figure 6

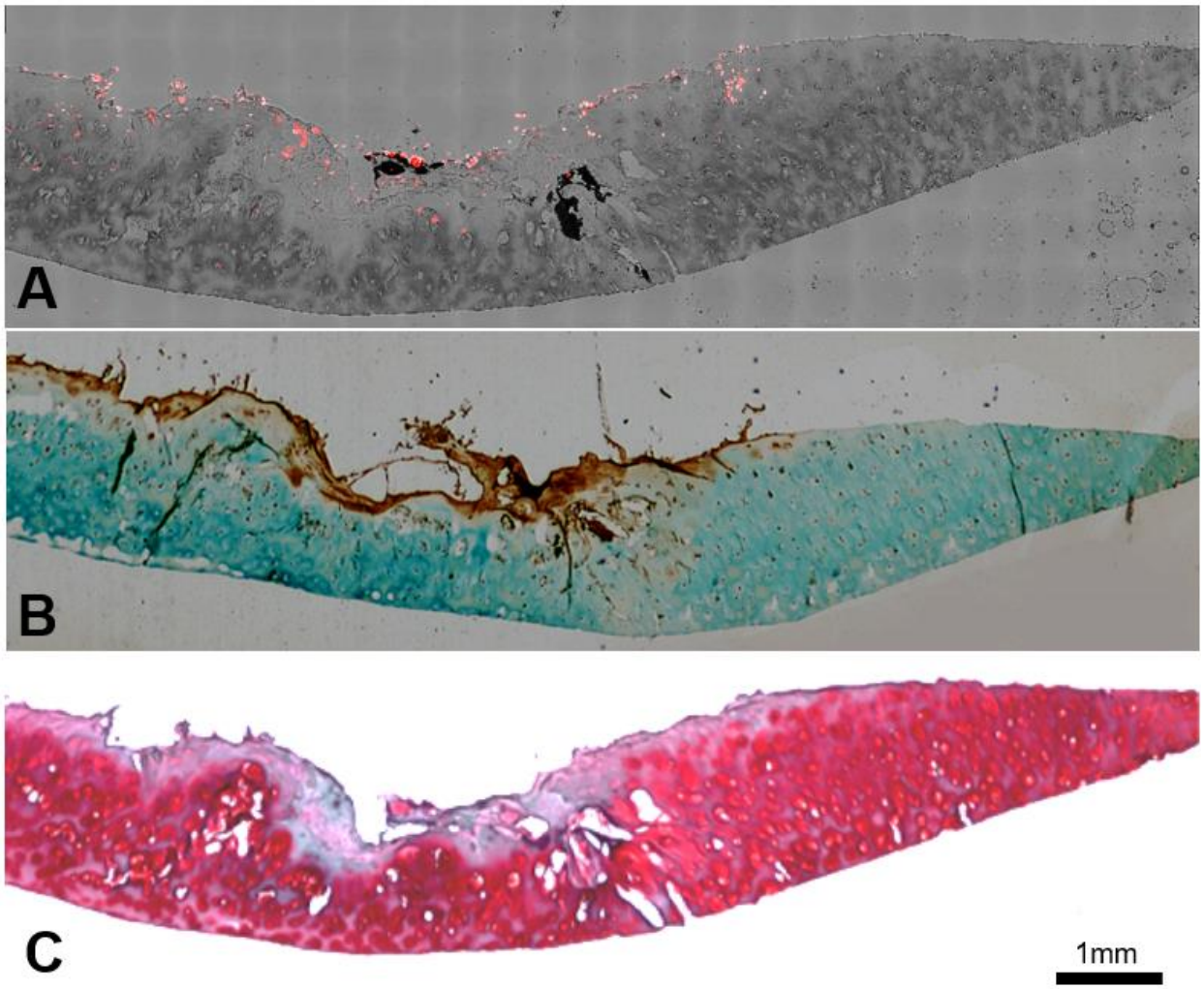

Figure 6. Co-localization of probes and cartilage tissue degeneration on human osteoarthritic explants were carried out using both confocal imaging and histological analysis. **(A)** Stitching image of FA-HA probe distribution on exposed tissue was taken using a Leica confocal laser-scanning microscope. **(B)** Scanning image of FR IHC staining on adjacent tissue section was taken using PathScan. **(C)** Scanning image of Safranin O staining on the identical tissue section (as in Figure 6A) was taken using PathScan.

References

[1] Kotlarz H, Gunnarsson CL, Fang H, Rizzo JA. Insurer and out-of-pocket costs of osteoarthritis in the US: evidence from national survey data. Arthritis Rheum. 2009;60:3546-53.
[2] Luo X, Pietrobon R, Sun SX, Liu GG, Hey L. Estimates and patterns of direct health care expenditures among individuals with back pain in the United States. Spine. 2004;29:79-86.
[3] Chu CR, Williams AA, Coyle CH, Bowers ME. Early diagnosis to enable early treatment of pre-osteoarthritis. Arthritis Res Ther. 2012;14:212.
[4] Eckstein F, Wirth W, Nevitt MC. Recent advances in osteoarthritis imaging—the osteoarthritis initiative. Nat Rev Rheumatol. 2012;8:622-30.
[5] Ding C, Zhang Y, Hunter D. Use of imaging techniques to predict progression in osteoarthritis. Curr Opin Rheumatol. 2013;25:127-35.
[6] Fernandez-Madrid F, Karvonen RL, Teitge RA, Miller PR, An T, Negendank WG. Synovial thickening detected by MR imaging in osteoarthritis of the knee confirmed by biopsy as synovitis. Magn Reson Imaging. 1995;13:177-83.
[7] Guermazi A, Roemer FW, Burstein D, Hayashi D. Why radiography should no longer be considered a surrogate outcome measure for longitudinal assessment of cartilage in knee osteoarthritis. Arthritis Res Ther. 2011;13:247.
[8] Kraus VB. Editorial [Hot Topic: Waiting for Action on the Osteoarthritis Front (Guest Editors: Virginia Byers Kraus and Thomas Aigner)]. Curr Drug Targets. 2010;11:518-20.
[9] Kandahari AM, Yang X, Dighe AS, Pan D, Cui Q. Recognition of immune response for the early diagnosis and treatment of osteoarthritis. J Immunol Res. 2015;2015:1-13.
[10] de Lange-Brokaar B, Ioan-Facsinay A, Van Osch G, Zuurmond A-M, Schoones J, Toes R, et al. Synovial inflammation, immune cells and their cytokines in osteoarthritis: a review. Osteoarthritis Cartilage. 2012;20:1484-99.
[11] Bondeson J, Blom AB, Wainwright S, Hughes C, Caterson B, van den Berg WB. The role of synovial macrophages and macrophage-produced mediators in driving inflammatory and destructive responses in osteoarthritis. Arthritis Rheum. 2010;62:647-57.
[12] Bondeson J, Wainwright SD, Lauder S, Amos N, Hughes CE. The role of synovial macrophages and macrophage-produced cytokines in driving aggrecanases, matrix metalloproteinases, and other destructive and inflammatory responses in osteoarthritis. Arthritis Res Ther. 2006;8:R187.
[13] Yang X, Chordia MD, Du X, Graves JL, Zhang Y, Park YS, et al. Targeting formyl peptide receptor 1 of activated macrophages to monitor inflammation of experimental osteoarthritis in rat. J Orthop Res. 2016;34:1529-38.
[14] Pessler F, Chen L, Dai L, Gomez-Vaquero C, Diaz-Torne C, Paessler M, et al. A histomorphometric analysis of synovial biopsies from individuals with Gulf War Veterans' Illness and joint pain compared to normal and osteoarthritis synovium. Clin Rheumatol. 2008;27:1127-34.
[15] Blom AB, van Lent PL, Holthuysen AE, van der Kraan PM, Roth J, van Rooijen N, et al. Synovial lining macrophages mediate osteophyte formation during experimental osteoarthritis. Osteoarthritis Cartilage. 2004;12:627-35.
[16] Antony AC. Folate receptors. Annu Rev Nutr. 1996;16:501-21.
[17] Paulos CM, Varghese B, Widmer WR, Breur GJ, Vlashi E, Low PS. Folate-targeted immunotherapy effectively treats established adjuvant and collagen-induced arthritis. Arthritis Res Ther. 2006;8:R77.
[18] Low PS, Henne WA, Doorneweerd DD. Discovery and development of folic-acid-based receptor targeting for imaging and therapy of cancer and inflammatory diseases. Acc Chem Res. 2008;41:120-9.
[19] Xia W, Hilgenbrink AR, Matteson EL, Lockwood MB, Cheng JX, Low PS. A functional folate receptor is induced during macrophage activation and can be used to target drugs to activated macrophages. Blood. 2009;113:438-46.
[20] Nakashima-Matsushita N, Homma T, Yu S, Matsuda T, Sunahara N, Nakamura T, et al. Selective expression of folate receptor beta and its possible role in methotrexate transport in synovial macrophages from patients with rheumatoid arthritis. Arthritis Rheum. 1999;42:1609-16.

[21] Chen W-T, Mahmood U, Weissleder R, Tung C-H. Arthritis imaging using a near-infrared fluorescence folate-targeted probe. Arthritis Res Ther. 2005;7:R310.
[22] Piscaer TM, Muller C, Mindt TL, Lubberts E, Verhaar JA, Krenning EP, et al. Imaging of activated macrophages in experimental osteoarthritis using folate-targeted animal single-photon-emission computed tomography/computed tomography. Arthritis Rheum. 2011;63:1898-907.
[23] Turk MJ, Breur GJ, Widmer WR, Paulos CM, Xu LC, Grote LA, et al. Folate-targeted imaging of activated macrophages in rats with adjuvant-induced arthritis. Arthritis Rheum. 2002;46:1947-55.
[24] Hansch A, Frey O, Sauner D, Hilger I, Haas M, Malich A, et al. In vivo imaging of experimental arthritis with near- infrared fluorescence. Arthritis Rheum. 2004;50:961-7.
[25] Kim H, Jeong H, Han S, Beack S, Hwang BW, Shin M, et al. Hyaluronate and its derivatives for customized biomedical applications. Biomaterials. 2017;123:155-71.
[26] Dosio F, Arpicco S, Stella B, Fattal E. Hyaluronic acid for anticancer drug and nucleic acid delivery. Adv Drug Del Rev. 2016;97:204-36.
[27] Tripodo G, Trapani A, Torre ML, Giammona G, Trapani G, Mandracchia D. Hyaluronic acid and its derivatives in drug delivery and imaging: recent advances and challenges. Eur J Pharm Biopharm. 2015;97:400-16.
[28] Xu X, Jha AK, Duncan RL, Jia X. Heparin-decorated, hyaluronic acid-based hydrogel particles for the controlled release of bone morphogenetic protein 2. Acta Biomater. 2011;7:3050-9.
[29] Yoon HY, Koo H, Choi KY, Lee SJ, Kim K, Kwon IC, et al. Tumor-targeting hyaluronic acid nanoparticles for photodynamic imaging and therapy. Biomaterials. 2012;33:3980-9.
[30] Zhang J, Rana S, Srivastava RS, Misra RD. On the chemical synthesis and drug delivery response of folate receptor-activated, polyethylene glycol-functionalized magnetite nanoparticles. Acta Biomater. 2008;4:40-8.
[31] Yap WT, Song WK, Chauhan N, Scalise PN, Agarwal R, Shea LD. Quantification of particle-conjugated or-encapsulated peptides on interfering reagent backgrounds. Biotechniques. 2014;57:39-44.
[32] Fasman GD. Practical handbook of biochemistry and molecular biology. Florida, USA: CRC press; 1989.
[33] Huang Y, Zhou J, Hakamivala A, Wu J, Hong Y, Borrelli J, et al. An optical probe for detecting chondrocyte apoptosis in response to mechanical injury. Sci Rep. 2017;7:10906.
[34] Zhou J, Tsai YT, Weng H, Baker DW, Tang L. Real time monitoring of biomaterial-mediated inflammatory responses via macrophage-targeting NIR nanoprobes. Biomaterials. 2011;32:9383-90.
[35] Monteiro-Riviere N, Inman A, Zhang L. Limitations and relative utility of screening assays to assess engineered nanoparticle toxicity in a human cell line. Toxicol Appl Pharmacol. 2009;234:222-35.
[36] Hattori Y, Sakaguchi M, Maitani Y. Folate-linked lipid-based nanoparticles deliver a NFκB decoy into activated murine macrophage-like RAW264. 7 cells. Biol Pharm Bull. 2006;29:1516-20.
[37] Zhou S, Thornhill TS, Meng F, Xie L, Wright J, Glowacki J. Influence of osteoarthritis grade on molecular signature of human cartilage. J Orth Res. 2016;34:454-62.
[38] Peng Z, Zhou J, Dacy A, Zhao D, Kearney V, Zhou W, et al. Design of a portable imager for near-infrared visualization of cutaneous wounds. J Biomed Opt. 2017;22:016010-.
[39] Fedchenko N, Reifenrath J. Different approaches for interpretation and reporting of immunohistochemistry analysis results in the bone tissue–a review. Diagn Pathol. 2014;9:221.
[40] Schmitz N, Laverty S, Kraus V, Aigner T. Basic methods in histopathology of joint tissues. Osteoarthritis Cartilage. 2010;18:S113-S6.
[41] Mohammed EMKA-D. Qualitative and Quantitative Determination of Folic acid in Tablets by FTIR Spectroscopy. IJAPBC. 2014;3:773-80.
[42] Ike RW. Diagnostic arthroscopy. Baillieres Clin Rheumatol. 1996;10:495-517.
[43] Lai W-FT, Chang C-H, Tang Y, Bronson R, Tung C-H. Early diagnosis of osteoarthritis using cathepsin B sensitive near-infrared fluorescent probes. Osteoarthritis Cartilage. 2004;12:239-44.
[44] Ryu JH, Lee A, Na JH, Lee S, Ahn HJ, Park JW, et al. Optimization of matrix metalloproteinase fluorogenic probes for osteoarthritis imaging. Amino Acids. 2011;41:1113-22.

[45] Che X, Chi L, Park CY, Cho G-H, Park N, Kim S-G, et al. A novel method to detect articular chondrocyte death during early stages of osteoarthritis using a non-invasive ApoPep-1 probe. Arthritis Res Ther. 2015;17:309.
[46] Kraus VB, McDaniel G, Huebner JL, Stabler TV, Pieper CF, Shipes SW, et al. Direct in vivo evidence of activated macrophages in human osteoarthritis. Osteoarthritis Cartilage. 2016;24:1613-21.
[47] Zolle I. Technetium-99m pharmaceuticals. Vienna, Austria: Springer; 2007.
[48] Sophia Fox AJ, Bedi A, Rodeo SA. The basic science of articular cartilage: structure, composition, and function. Sports health. 2009;1:461-8.
[49] Acc Chem ResAltman R, Manjoo A, Fierlinger A, Niazi F, Nicholls M. The mechanism of action for hyaluronic acid treatment in the osteoarthritic knee: a systematic review. BMC Musculoskel Disord. 2015;16:321.
[50] Printz JO, Lee JJ, Knesek M, Urquhart AG. Conflict of interest in the assessment of hyaluronic acid injections for osteoarthritis of the knee: an updated systematic review. J Arthroplasty. 2013;28:30-3. e1.
[51] Weissleder R, Ntziachristos V. Shedding light onto live molecular targets. Nat Med. 2003;9:123-8.
[52] Nguyen DT, van Horssen P, Derriks H, van de Giessen M, van Leeuwen T. Autofluorescence imaging for improved visualization of joint structures during arthroscopic surgery. J Exp Orthop. 2017;4:19.
[53] Collins MN, Birkinshaw C. Hyaluronic acid based scaffolds for tissue engineering—A review. Carbohydr Polym. 2013;92:1262-79.
[54] Ishida O, Tanaka Y, Morimoto I, Takigawa M, Eto S. Chondrocytes are regulated by cellular adhesion through CD44 and hyaluronic acid pathway. J Bone Miner Res. 1997;12:1657-63.
[55] Balazs E, Darzynkiewicz Z. The effect of hyaluronic acid on fibroblasts, mononuclear phagocytes and lymphocytes. Biology and fibroblasts. 1973;66:237-52.
[56] Partsch G, Schwarzer C, Neumüller J, Dunky A, Petera P, Bröll H, et al. Modulation of the migration and chemotaxis of PMN cells by hyaluronic acid. Z Rheumatol. 1989;48:123-8.
[57] Forrester JV, Lackie J. Effect of hyaluronic acid on neutrophil adhesion. J Cell Sci. 1981;50:329-44.
[58] Zhang Y, Yang J. Design strategies for fluorescent biodegradable polymeric biomaterials. J Mater Chem B. 2013;1:132-48.
[59] Okuda T, Kobayashi Y, Yanamoto S, Okamoto H. PEG conjugation of a near-infrared fluorescent probe for noninvasive dual imaging of lung deposition and gene expression by pulmonary gene delivery. J Drug Targeting. 2012;20:801-12.
[60] Melancon MP, Wang W, Wang Y, Shao R, Ji X, Gelovani JG, et al. A novel method for imaging in vivo degradation of poly (L-glutamic acid), a biodegradable drug carrier. Pharm Res. 2007;24:1217-24.
[61] Zhang Y, Guo C, Li S, Luo K, Hu J, Gu Z. The Potential of Poly [N-(2-hydroxypropyl) methacrylamide] via Reversible Addition-Fragmentation Chain Transfer Polymerization as Safe Nanocarrier. J Nanosci Nanotechnol. 2016;16:5746-54.

Chapter 2. Bacterial Acidity-Triggered Antimicrobial Activity of Self-assembling Peptide Nanofibers

Weike Chen,[a] Shuxin Li,[b] Paul Renick,[c] Su Yang,[a] Nikhil Pandy,[b] Cara Boutte,[c] Kytai T. Nguyen,[b] Liping Tang,[*,b] and He Dong[*,a]

a. Department of Chemistry and Biochemistry, The University of Texas at Arlington, Arlington, TX, 76019, USA. Email: he.dong@uta.edu.

b. Department of Bioengineering, The University of Texas at Arlington, Arlington, TX, 76019, USA.

c. Department of Biology, The University of Texas at Arlington, Arlington, TX, 76019, USA.

A self-assembling peptide nanofiber is developed to sense the microenvironmental pH change associated with bacterial growth. Using a near-infrared probe, a strong correlation was observed between the local pH reduction of bacterial colonies with the degree of peptide disassembly, which led to their enhanced antimicrobial activity against anaerobic bacteria.

Trigger-responsive nanomaterials have tremendous promise for targeted therapeutic delivery strategies that improve the treatment of a variety of diseases.[1] Among various approaches, self-assembly has been proven as an effective bottom-up approach to construct functional nanomaterials. A wide range of molecular building blocks, including amphiphilic polymers, lipids, proteins and peptides can be custom-designed and assembled into "smart" nanomaterials that can sense various disease-specific microenvironmental conditions.[2] Self-assembled nanomaterials can easily change their physicochemical properties in response to the environmental change and lead to local release of therapeutics with enhanced drug potency and reduced side effects on healthy tissues and cells. In recent years, great levels of success have been achieved for nanomaterials designed for targeted cancer therapy.[3] However, the development of self-assembled nanomaterials for targeted antimicrobial delivery is just getting underway for infectious disease treatment.[4]

Similar to some of the tumor tissues, certain bacteria can reduce the local pH of the infection tissues through low oxygen triggered anaerobic fermentation.[5] Host immune response can further lower the local pH where bacteria reside through mechanisms of production of lactic acids during phagocytosis.[6] While the acidic pH is considered as an undesirable factor causing the reduction of the antimicrobial activity of several classes of antibiotics,[7] it can be utilized as a natural physiological cue for the design of antimicrobial nanomaterials for targeted antimicrobial delivery. Recent reports have demonstrated advances in the design of acid-sensitive nanoparticles

for targeting the bacterial membrane and delivery of small molecule antibiotics to treat bacterial infections in acidic conditions.[4a] Acid-dependent helical polypeptides were also reported to selectively target and eradicate pathogenic *H. pylori* without affecting commensal bacteria in the stomach.[4d] These successful examples provide the inspiration and highlight the feasibility of using pH as a physiological trigger to achieve targeted antimicrobial therapy.

In this work, we sought to develop a novel acid-activatable antimicrobial therapy by capitalizing on our recent development of self-assembling nanofibers (SANs) for bacterial acidity triggered antimicrobial delivery. SANs are supramolecular assemblies of *de novo* designed multidomain peptides (MDPs) that have been explored as highly cytocompatible antimicrobial and cell penetrating nanomaterials.[8] The first generation of MDPs has a general formula of $K_x(QL)_yK_z$ (amino acid single code letter K: Lysine, Q: Glutamine, L: Leucine) to mimic natural cationic antimicrobial peptides (AMPs). Unlike most conventional AMPs that exist as monomers in solution, MDPs can form supramolecular β-sheet nanofibers in which the hydrophobic residues and non-polar surface are partially masked between the two sheets, which has been proven as an important factor to minimize the cytotoxicity of MDPs toward mammalian cells.[9] As shown in our previous work, the cytocompatibility was greatly enhanced for SANs compared to that of traditional monomeric AMPs. However, on the negative side, the confinement of the hydrophobic moiety within the assembly can also reduce their antimicrobial activity while monomeric AMPs are more potent to kill bacteria. As such, the current study by developing SANs that undergo pH-responsive disassembly combines the advantages of both self-assembled peptides in terms of their cytocompatibility and monomeric AMPs in terms of their antimicrobial activity to treat acidity-associated bacterial infection. The central hypothesis is SANs under the physiological condition are bio-inert because the membrane-interacting hydrophobic moieties of SANs are buried inside

the assembly and not accessible to the cell membrane. At the bacterial colonization site with an acidic pH, MDPs become charged and the increased charge density triggers SANs disassembly and subsequent release of activated peptides to effectively interact with the cell membrane and kill bacteria (**Figure 1**).

Three MDPs with the sequences of $WH_5(QL)_6K_2$, $WH_7(QL)_6K_2$, and $WH_9(QL)_6K_2$ abbreviated as WH_5, WH_7 and WH_9 (H: Histidine, W: Tryptophan) were initially explored as the building units to fabricate SANs. The sequences were chosen based on the following considerations. First, the central repeating (QL) domain provides the driving force for SANs formation under the neutral physiological condition as discussed in our previous studies.[8b] Second, oligo-histidine of different lengths was incorporated at the N-terminus to endow pH-responsiveness to SANs. At a pH below the pKa of histidine, peptides become charged. The electrostatic repulsion among the positively charged MDPs will destabilize SANs and lead to the release of activated MDPs that can effectively eradicate bacteria. Third, the numbers of histidine residues are varied in order to integrate and achieve a good balance between self-assembly under the neutral condition and disassembly upon acidification. MDPs with different numbers of histidine would render a small library to explore the effect of charge on SANs stability, disassembly efficiency and their resulting biological activities. Lastly, two lysine residues were appended at the C-terminus to ensure sufficient solubility of SANs and minimize lateral fiber aggregation through electrostatic repulsion. All peptides contain a tryptophan residue for accurate determination of the peptide concentration by UV spectroscopy.

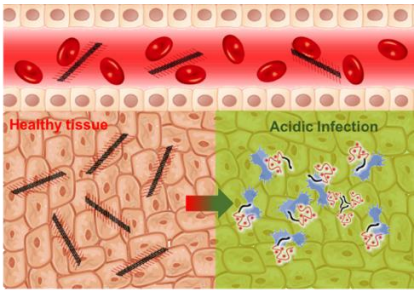

Figure 1. Cartoon representation of cytocompatible and hemocompatible SANs formed by pH-responsive MDPs and their disassembly triggered by local bacterial acidity for the delivery of activated MDPs to eradicate bacteria.

Elucidating the physicochemical properties of MDPs as a function of pH is critical to tailoring their biological activities. Critical assembly concentration (CAC) measurements were first conducted to investigate their ability to assemble under different pH conditions. As shown in **Figure S2**, a non-linear relationship was observed for all three MDPs at pH 7.4 (Tris buffer, 20 mM) suggesting the formation of higher ordered assemblies as the concentration increased. At an acidic pH (MES buffer, pH 5.7, 20 mM), a linear correlation was found between the fluorescence intensity and peptide concentrations, suggesting the majority of peptides do not self-assemble and rather remain isolated. It is worth noting that we choose pH 5.7 as the acidic condition for this study, considering the balance between the protonation degree of histidine (pKa=~6) and bacterial growth under the acidic condition. The pH-dependent self-assembly and disassembly was further investigated and confirmed by circular dichroism (CD) spectroscopy. At pH 7.4, all three peptides exhibited predominant β-sheet structures as characterized by a minimum peak between 210-220 nm (**Figure S3a**) indicating the formation of SANs. When the pH is reduced to 5.7, which is below the pKa point of histidine, the presumed increase in positive charges and electrostatic repulsion triggered disassembly and unfolding of β- sheets to random coils and/or weak helices. As shown in **Figure S3b**, all three MDPs unfolded upon pH reduction, but to different degrees. WH_7 and WH_9 exhibited more disordered structures than WH_5 given the larger blue shifts of the minimum absorption down to ~ 203 nm indicating a greater tendency to disassemble. To quantitatively determine the extent of SANs disassembly, spin dialysis was used to estimate the amounts of disassembled MDPs upon pH reduction. Centrifugal filters with molecular weight (MW) cutoff at 10 kDa and 30 kDa were used to separate the monomeric MDP and any potential non-specific aggregates (up to 9 mers) (due to their amphiphilic nature) from the residual higher ordered assemblies, respectively. As shown in **Table 1**, no materials were

detected in the filtrate for all three MDPs through spin dialysis suggesting the stability and integrity of SANs at the neutral pH. At the acidic pH, disassembly occurs as shown by the increased concentrations of MDPs in the filtrate using both filters. It was estimated that 24.60% of WH_5, 34.70% of WH_7 and 41.00% of WH_9 were disassembled to monomers based on the dialysis result using the filter with a MW cutoff at 10 kDa. Using a 30 kDa filter, the percentage of MDPs in the filtrate increased to 37.77%, 62.56% and 71.46% for WH_5, WH_7 and WH_9, respectively.

Table 1. Quantification of disassembled MDPs

Peptides	10 kDa filter		30 kDa filter	
	pH 7.4	pH 5.7	pH 7.4	pH 5.7
WH_5	0	24.60 ± 0.08%	0	37.77 ± 0.56%
WH_7	0	34.70 ± 0.08%	0	62.56 ± 3.55%
WH_9	0	41.00 ± 0.49%	0	71.64 ± 0.27%

Standard deviation is calculated based on 3 measurements for each sample

The filtrate of WH_9 at pH 5.7 was analyzed by CD spectroscopy showing highly disordered random coil structures (**Figure S3c**), thus excluding the possibility of the presence of β-sheet oligomers in the filtrate. The oligomeric species present in the filtrate is likely due to the non-specific aggregation between the amphiphilic MDPs. Transmission electron microscopy (TEM) reveals the morphological change of MDPs under different pH treatments. For TEM characterization and the following biological evaluation, we primarily focused on WH_9 because it is the most sensitive to pH change giving a higher extent of disassembly upon solution acidification. At pH 7.4, WH_9 spontaneously self-assembled to form elongated fibers (**Figure 2a**). Reducing the pH to 5.7 led to a significant reduction of the fiber density and the formation of non-specific spherical aggregates (**Figure 2b**). We suspect that these spherical aggregates were formed from disassembled MDPs due to the drying effect during TEM sample preparation

process. The disassembly of SANs was verified by dynamic light scattering (DLS) measurements showing a dramatically reduced particle size to below 2 nm when pH was reduced (**Figure 2c** and **Figure S4**). Although the number mean of the hydrodynamic diameter generated by DLS does not represent the actual size of these nanofibers due to their non-spherical shapes, the dramatic size reduction suggests the effectiveness of solution acidity to trigger the disassembly of SANs.

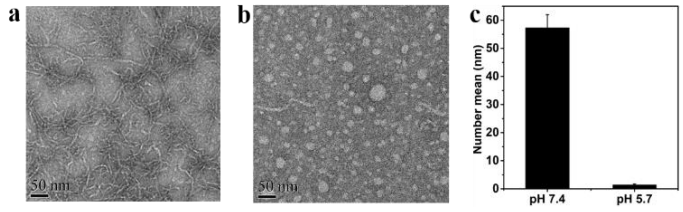

Figure 2. Negatively stained TEM images of WH_9 at (**a**) pH 7.4 showing SANs formation and (**b**) at pH 5.7 showing SANs disassembly. (**c**) pH-dependent hydrodynamic size measurement by DLS. Peptide concentration: 100 μM in Tris buffer (pH 7.4, 20 mM) and MES buffer (pH 5.7, 20 mM)

Acidity-triggered SANs disassembly was further studied in the context of bacterial inoculation on an agar plate. We chose *Bacteroides fragilis* as a model bacterium that undergoes anaerobic growth leading to the acidification of the surrounding environment. We first determined whether the growth of *B. fragilis* would influence the pH immediately adjacent to the bacterial colony. Using a pH ratiometric near infrared probe developed recently,[10] we measured the change of fluorescent intensity of the probe with time using an *in vivo* Kodak imager. The results allow us to calculate the pH nearby the colony on an agar plate at 0.5, 2.5, 7, and 22.5 hrs upon bacterial inoculation. Interestingly, we find that growth of *B. fragilis* releases metabolites which can cause the surrounding environment to become acidic (from pH 7.5 to pH 6.3 in less than 24 hrs) (**Figure S5**). To test whether the in-situ low pH can induce SANs disassembly, we synthesized and prepared rhodamine (Rho)-labeled WH_9. Rho-WH_9 has very low fluorescent intensity due to fluorescent quenching upon self-assembly. By reducing the local pH, WH_9 disassembles leading to the recovery of rhodamine fluorescence. Therefore the fluorescence intensity of the peptide reflects the degree of peptide disassembly and can be used to correlate

with the microenvironmental pH change associated with bacterial growth. To determine whether the acidic environment nearby bacterial colonies causes SANs to disassemble, Rho-WH_9 was applied on both the bacterial colonies and non-inoculated agars as controls after 24 hrs of bacterial inoculation. The fluorescence intensity was monitored immediately using an *in vivo* Kodak imager. The results showed an average of 88% increase of the fluorescence intensity for peptides deposited on the bacteria colonies than those on the agar media without bacteria (**Figure 3a**), suggesting a local acidic pH can trigger the disassembly of SANs, leading to the recovery of self-quenched fluorescence. The fluorescence intensity of the peptide across the bacterial colony was further plotted as a function of imaging pixels (~ 0.1 mm/per pixel) starting from the outermost of a colony (shown as 0 on the x-axis of **Figure 3b**) while moving toward the center (shown as 10 on the x-axis of **Figure 3b**). The local bacterial pH change across a single colony was measured by the ratiometric fluorescence probe described above and plotted in the same manner. A good correlation was observed between the reduced pH and the increased fluorescence of Rho-WH_9, further confirming local bacterial acidity can trigger SANs disassembly.

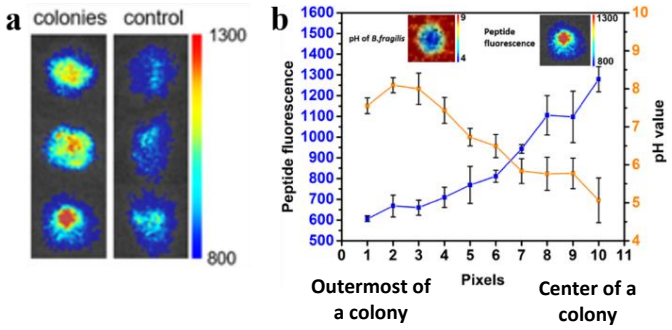

Figure 3. Local bacterial acidity triggered peptide disassembly as determined by in situ fluorescence microscopy. a) Fluorescence intensity of Rho-labeled WH_9 deposited on 3 bacterial colonies (3 spots on the left panel) compared to those on agar media (right panel) without bacteria showing that the acidic bacterial environment can induce SANs disassembly that led to a recovery of the self-quenched rhodamine fluorescence. b) Correlation of the local bacterial pH (orange line) with the fluorescence intensity of Rho-labeled WH_9 (blue lines) applied on bacterial colonies. The inset pictures are fluorescent microscopic images of bacterial colonies upon Rho-Labeled peptide treatment (right) and colonies containing the near infrared pH probe (left).

The antimicrobial activities of WH_9 were tested against both gram-negative bacteria, *Escherichia coli* and *B. fragilis* and gram-positive bacteria, *Staphylococcus aureus* under the anaerobic condition where bacterial cultures became acidic over time Peptides were co-incubated

with *E. coli*, *B. fragilis* and *S. aureus* for 48 hrs and the UV absorbance at 600 nm was measured for the estimation of the minimum inhibitory concentration (MIC) values. As shown in **Table 2**, WH_9 was effective against all three bacterial strains in the anaerobic condition where the bacterial culture gradually became acidic to pH 6.4. The MIC values of WH_9 were determined at 10 μM against *E. coli*, 5 μM against *B. fragilis* and 5 μM against *S. aureus*. In contrast, the MIC of WH_9 was estimated at 40 μM against *E. coli* in the aerobic condition where the culture pH remained neutral (pH was between 7.2 and 7.5 during culture). For aerobic bacterial cultures with a starting pH at 5.7, the MIC was determined as 10 μM comparable to that determined in the anaerobic condition. In comparison, the MICs of WH_5 and WH_7 were determined at 40 μM and 20 μM in the acidic aerobic *E. coli* cultures showing less potency to inhibit the growth oft he bacteria. The antimicrobial activity also correlates well with the peptide's ability to dissemble as detailed in the spin dialysis experiment (**Table 1**).

Table 2. Antimicrobial activity, cytotoxicity and hemolytic activity

Peptides	MIC (μM)					IC_{50} μM	HC_{10} μM
	Anaerobic			Aerobic			
	E.coli	*B. fragilis*	*S.aureus*	*E.coli*			
				pH 7.4	pH 5.7		
WH_9	10	5	5	> 40	10	>80	>160

The mode of antimicrobial action was investigated by epifluorescence microscopy. WH_9 was co-incubated with *E. coli* aerobically so that the culture pH can be adjusted and maintain at either acidic or neutral during the entire culture. A live-dead assay was performed wherein *E. coli* was incubated with WH_9 for 3 hrs, followed by staining with SYTO9 and Propidium Iodide (PI). As shown in (**Figure 4a**), a much higher fraction of *E. coli* cells fluoresced red at the acidic pH due to pH-triggered disassembly and release of peptides that can increase the membrane permeability of PI. At the neutral pH (**Figure 4b**), the peptide was confined within the SANs and

does not have sufficient freedom to access to and further permeate the bacterial cell membrane. The live-dead assay was also performed in Gram-positive *S. aureus* culture showing the same trend of pH-dependent antimicrobial activity (**Figure S6**).

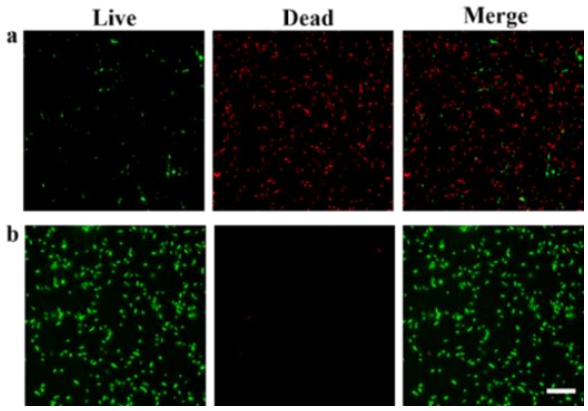

Figure 4. Fluorescence images of Live/dead bacterial assay results. Top panel: *E.coli* treated with 20 μM WH9 at (**a**) pH 5.7 and (**b**) pH 7.4 for 3hrs. Live bacteria were stained with SYTO9 (green) and dead bacteria was stained with PI (red). Scale bar: 20 μm.

The physical interaction between WH_9 and bacteria was also studied by fluorescence microscopy upon incubation of FITC-labelled WH_9 with *E. coli* followed by PI staining. The binding affinity of WH_9 toward bacteria was greatly improved upon acidification as demonstrated by the numbers of bacterial cells that are attached by peptides showing green fluorescence on the cell membrane (**Figure S7a**) while at the neutral condition much less binding occurs between the peptides and bacteria (**Figure S7b**). Scan electron microscopy (SEM) was used to visualize any morphological change induced in bacteria by exposure to WH_9 at the acidic condition. As compared to control bacteria without peptide treatment (**Figure S8a**), *E. coli* incubated with WH_9 under the acidic culture condition showed significant membrane damage (**Figure S8b**), suggesting the mode of action is through bacterial membrane disruption by the disassembled peptides.

A critical challenge associated with conventional AMPs is their moderate to severe cytotoxicity and hemolytic activity.[11] We have recently demonstrated that self-assembly can be an effective approach to reduce the non-polar membrane-contact area of AMPs leading to greatly improved cytocompatibility and bacterial cell selectivity.[9] To evaluate the cytotoxicity of the

newly designed WH_9 toward mammalian cells during blood circulation, NIH/3T3 fibroblasts were incubated with peptides at various concentrations and the cell viability was quantified by the MTT assay. 80 μM was selected as the upper concentration threshold to avoid potential precipitate formation as the peptide concentration increases in the mammalian culture media. As shown in **Figure S9**, dose-dependent cell viability was measured showing > 80% of cell viability up to 40 μM and 72% cells were still alive upon incubation with peptides at 80 μM. The hemocompatiblity was evaluated by incubating human red blood cells (RBCs) with WH_9 at different concentrations for 1 hr and released haemoglobin was measured by UV spectroscopy (**Figure S10**). Within the tested peptide concentrations up to 160 μM (*16* times of the MIC) less than 5% of hemolysis was observed with peptide-treated RBCs compared to the positive control group of RBCs treated with Triton-100. Taken together, the pH-triggered antimicrobial activity and excellent cytocompatibility and hemocompatibility of self-assembled WH_9 highlight their great potential as a new antimicrobial strategy to effectively treat bacterial infections associated with acidity.

In summary, we have demonstrated a new pH-responsive antimicrobial nanomaterial based on the self-assembly *of de novo* designed MDPs for acid-responsive antimicrobial delivery at the site of infection associated with bacterial acidity. The MDP can be designed to form stable nanofibrous structure in neutral pH with excellent cytocompatibility and hemocompatibility. The pH-triggered disassembly was demonstrated in both the aqueous solution and on a bacteria-inoculated agar plate and shown to be important factors for their antimicrobial activity. This new antimicrobial strategy while awaiting more extensive *in vitro* evaluation and *in vivo* studies holds great promise to treat bacterial infections in which acidity plays an important role in bacteria pathogenesis. For future studies, SANs based on custom-designed non-natural amino acids may

offer diverse chemical functionality and broader pH-tunability to suit various clinical needs in the combat of infectious diseases.

This study was supported by the National Science Foundation (DMR 1824614) and the start-up funds from the University of Texas at Arlington.

Conflicts of interest

There are no conflicts to declare.

Notes and references

1 (a) V. P. Torchilin, *Nat. Rev. Drug Discov.* 2014, ***13***, 813; (b) O. Veiseh, B. C. Tang, K. A. Whitehead, D. G. Anderson and R. Langer, *Nat. Rev. Drug Discov.* 2014, ***14***, 45; (c) E. J. Chung, L. B. Mlinar, K. Nord, M. J. Sugimoto, E. Wonder, F. J. Alenghat, Y. Fang and M. Tirrell, *Adv. Healthc. Mater.* 2015, ***4***, 367; (d) L. L. Lock, Z. Tang, D. Keith, C. Reyes and H. Cui, *ACS Macro Lett.* 2015, ***4***, 552; (e) Y. Wang and D. S. Kohane, *Nat. Rev. Mater.* 2017, ***2***, 17020; (f) D. Rosenblum, N. Joshi, W. Tao, J. M. Karp and D. Peer, *Nat. Commun.* 2018, ***9***, 1410.

2 (a) H. J. Chung and T. G. Park, *Nano Today* 2009, ***4***, 429; (b) H. Hosseinkhani, P.-D. Hong and D.-S. Yu, *Chem. Rev.* 2013, ***113***, 4837; (c) L. Zhang, J. M. Chan, F. X. Gu, J.-W. Rhee, A. Z. Wang, A. F. Radovic-Moreno, F. Alexis, R. Langer and O. C. Farokhzad, *ACS Nano.* 2008, ***2***, 1696.

3 (a) L. Gu and D. J. Mooney, *Nat. Rev. Cancer.* 2015, ***16***, 56; (b) D. A. Scheinberg, C. H. Villa, F. E. Escorcia and M. R. McDevitt, *Nat. Rev. Clin. Oncol.* 2010, ***7***, 266; (c) J. A. Barreto, W. O'Malley, M. Kubeil, B. Graham, H. Stephan and L. Spiccia, *Adv. Mater.* 2011, ***23***, H18; (d) Q. Sun, Z. Zhou, N. Qiu and Y. Shen, *Adv. Mater.* 2017, ***29***, 1606628.

4 (a) A. F. Radovic-Moreno, T. K. Lu, V. A. Puscasu, C. J. Yoon, R. Langer and O. C. Farokhzad, *ACS Nano.* 2012, ***6***, 4279; (b) M. Hughes, S. Debnath, C. W. Knapp and R. V. Ulijn, *Biomater. Sci.* 2013, ***1***, 1138; (c) B. Horev, M. I. Klein, G. Hwang, Y. Li, D. Kim, H. Koo and D. S. W. Benoit, *ACS Nano.* 2015, ***9***, 2390; (d) M. Xiong, Y. Bao, X. Xu, H. Wang, Z. Han, Z. Wang, Y. Liu, S. Huang, Z. Song, J. Chen, R. M. Peek, L. Yin, L.-F. Chen and J. Cheng, *Proc. Natl. Acad. Sci. U.S.A.* 2017, ***114***, 12675.

5 (a) S. Fuchs, J. Pané-Farré, C. Kohler, M. Hecker and S. Engelmann, *J. Bacteriol.* 2007, ***189***, 4275; (b) B. Marteyn, F. B. Scorza, P. J. Sansonetti and C. Tang, *Cell. Microbiol.* 2011, ***13***, 171.

6 (a) R. Dubos, *Lancet* 1955, ***266***, xxiv; (b) A. S. Trevani, G. Andonegui, M. Giordano, D. H. López, R. Gamberale, F. Minucci and J. R. Geffner, *J. Immunol.* 1999, ***162***, 4849; (c) B. J. Marsland and E. S. Gollwitzer, *Nat. Rev. Immunol.* 2014, ***14***, 827; (d) M. Kilian, I. L. C. Chapple, M. Hannig, P. D. Marsh, V. Meuric, A. M. L. Pedersen, M. S. Tonetti, W. G. Wade and E. Zaura, *Bdj* 2016, ***221***, 657.

7 R.-C. Mercier, C. Stumpo and M. J. Rybak, *J. Antimicrob. Chemother.* 2002, ***50***, 19.

8 (a) D. Xu, D. Dustin, L. Jiang, D. S. K. Samways and H. Dong, *Chem. Commun.* 2015, ***51***, 11757; (b) D. Xu, L. Jiang, A. Singh, D. Dustin, M. Yang, L. Liu, R. Lund, T. J. Sellati and H. Dong, *Chem. Commun.* 2015, ***51***, 1289.
9 D. Xu, W. Chen, Y. J. Tobin-Miyaji, C. R. Sturge, S. Yang, B. Elmore, A. Singh, C. Pybus, D. E. Greenberg, T. J. Sellati, W. Qiang and H. Dong, *ACS Infect. Dis.* 2018, ***4***, 1327.
10 Y.-T. Tsai, J. Zhou, H. Weng, J. Shen, L. Tang and W.-J. Hu, *Adv. Healthc. Mater.* 2014, ***3***, 221.
11 W. Aoki, K. Kuroda and M. Ueda, *J. Biosci. Bioeng.* 2012, ***114***, 365.

Supporting Information

Experiment section

Materials and methods

1. Materials

Fmoc-protected amino acids, 2-(6-Chloro-1-H-benzotriazole-1-yl)-1,1,3,3-

tetramethylaminium hexafluorophosphate (HCTU), MBHA rink amide resin, were purchased from Novabiochem. Piperidine, diisopropylethylamine (DIPEA) 5(6)-Carboxyfluorescein (FAM), 5(6)-carboxy-tetramethyl-rhodamine, Mueller Hinton Broth (MHB), MTT assay kit were purchased from Sigma-Aldrich. LIVE/DEAD™ BacLight™ Bacterial Viability Kit, Centrifugation filters with molecular weight cutoff at 10 kDa and 30 kDa, Agar, Triton™ X-100, Blood agar (TSA with 5% sheep blood) were purchased from Fisher Scientific. Dulbecco's modified Eagle medium (DMEM) culture medium was purchased from Life Technologies. Fetal Bovine Serum (FBS) was purchased from VWR. TEM staining reagent, uranium acetate dihydrate and TEM grid were purchased from TED PELLA, INC. *Escherichia coli* (ATCC 25922), *Bacteroides fragilis* (ATCC 25285) and *Staphylococcus aureus* (ATCC 29213) were purchased from ATCC.

2. Synthesis and purification of peptides

Multidomain peptides were synthesized on a *Prelude*® peptide synthesizer using standard FMOC-solid phase peptide synthesis procedures. Fmoc groups were deprotected by 20% (V/V)

piperidine in N, N-dimethylformamide (DMF) for 5 min (2 times). HCTU was used as the coupling reagent and mixed Fmoc protected amino acids in the presence of DIPEA with a molar ratio of 1:1:2.5 (amino acid: HCTU: DIPEA). Upon the completion of the synthesis, the N-terminus of the peptides were acetylated in the presence acetic anhydride and DIPEA in DMF. The acetylated peptides were cleaved from the resin using a mixture of trifluoroacetic acid (TFA) / triisopropanolsilane (TIS) / H_2O (95/2.5/2.5 by volume) for 3 hours. The cleavage solution was collected through filtration and neat TFA was used to wash the resin twice. TFA solution was evaporated under moderate air flow. The residual peptide solution was precipitated in cold diethyl ether, followed by centrifugation and washing with cold diethyl ether for four times. The crude peptide was dried under vacuum overnight for HPLC purification. The peptide was purified using a preparative reversed phase C4 column with a linear gradient of water/acetonitrile containing 0.05% TFA. Elution was monitored at 230 nm and 280 nm. The mass of the three peptides were confirmed by MALDI. WH_5: expected $[M+H]^+$: 2634, observed $[M+H]^+$: 2634; WH_7: expected $[M+H]^+$: 2908, observed $[M+H]^+$: 2908; WH_9: expected $[M+H]^+$: 3182, observed $[M+H]^+$: 3182. Fluorescein and rhodamine terminated peptides were synthesized as follows. After final deprotection of the peptide, the N-terminus was coupled with 4 equivalents of 5(6)-carboxyl fluorescein or 5(6)-carboxy-tetramethyl-rhodamine using a combination of 4 equivalents of HCTU and 8 equivalents of DIPEA in DMF. The reaction mixture was stirred overnight. The completion of the coupling reaction was confirmed by the Kaiser test. If necessary, the coupling of 5-(6)-carboxyl-fluorescein or 5(6)-carboxy-tetramethyl-rhodamine was repeated once. The cleavage and purification procedure followed the same procedure as described for the nonlabelled peptides. The molecular weight was confirmed by MALDI. FITC-WH_9: expected $[M+H]^+$: 3499, observed $[M+H]^+$: 3500; Rho-WH_9: expected $[M+H]^+$: 3553, observed $[M+H]^+$: 3554.

The purified MDP solutions that were collected from HPLC machine were lyophilized for 48hrs to remove any solvents. Then the powder of MDPs was dissolved in sterile Tris buffer or MES buffer for further bacterial and cell assay.

3. Structural Characterization

3.1 Circular Dichroism (CD) Spectroscopy

Samples were prepared by dilution from the peptide stock solution to a concentration at 50 μM in either Tris buffer (pH 7.4, 20 mM) or MES buffer (pH 5.7, 20 mM). The samples were incubated at 4°C overnight. Data were collected from 250 nm to 190 nm at room temperature (RT) using a 1 mm cuvette, a bandwidth at 1 nm, scan rate at 100 nm/min and a response time of 2 sec. Each spectrum was averaged from three scans. The mDeg of rotation was converted to molar residual ellipticity via the formula $\theta=(mDeg*1000)/(c*n*l)$, where c is the concentration of the peptide solution expressed in mM, n is the number of amino acids in the peptide sequence and l is the path length of the cell used in mm.

3.2 Transmission Electron Microscopy (TEM)

Sample preparation was the same as that used in the CD experiment. Peptide solution (10 μL) was dropped onto a holey carbon grid (TED PELLA 01824). After 2 minutes, excess solution was carefully removed with filter paper. 10 μL of 2 wt % uranyl acetate aqueous solution was dropped onto the grid for negative staining. After 2 minutes, excess staining solution was removed and the TEM samples were dried for overnight before imaging.

3.3 Critical aggregation concentration (CAC) measurement

Peptide solution (160 μM) was added in either 200 μL Tris buffer (20 mM, pH 7.4) or 200 μL MES buffer (20 mM, pH 5.7) with an increment of 2 μL each time. Fluorescence spectra were acquired after each peptide addition by monitoring the emission of peptides from 295 nm to 440 nm using an excitation wavelength at 280 nm. Fluorescence intensity at 350 nm was plotted as a function of the peptide concentrations. The CAC was determined to be the concentration at which nonlinearity started to develop as shown in **Figure S2**.

4. Minimum inhibitory concentration (MIC) determination

For the MIC test in the aerobic condition, *E.coli* was cultured in MHB media under constant shaking at 100 rpm at 37 ^{o}C to reach the mid-exponential growth phase. The bacterial solution was plated on an agar plate for colony forming unit (CFU) counting. Bacterial suspensions were diluted to approximately $2x10^5$ CFU/mL in MHB media at either pH 7.4 or 5.7. Peptide solutions

at various concentration (80, 40, 20, 10, 5, 2.5 µM) were prepared in either Tris buffer (pH 7.4, 20 mM) or MES buffer (pH 5.7, 20 mM). 50 µL of each peptide solution was mixed with 50 µL of bacterial solution in a 96-well plate and the experiments were performed in triplicates. The plates were incubated at 37 ^{o}C under constant shaking at 100 rpm for 18 hrs and the optical density (OD) at 600 nm was measured on a plate reader. The MIC was determined at the peptide concentration in which OD reading is below 0.06 and no cloudiness was visible to naked eyes.

For the MIC test in the anaerobic condition, *E. coli* (ATCC 25922), *B. fragilis* (ATCC 25285) and *S. aureus* (ATCC 29213) inocula were prepared using the BBL Prompt Inoculation System to generate an approximate 1.5 x 10^8 CFU/mL that was further diluted to generate an inoculum at 1.0 x 10^6 CFU/mL in MHB media at pH 7.4. Peptide solutions with various concentration (80, 40, 20, 10, 5, 2.5 µM) were prepared in Tris buffer (pH 7.4, 20 mM). All the reagents for the anaerobic test were reduced under anaerobic conditions for at least 2 hrs prior to the initiation of testing and care was taken to minimize all bacterial strains to oxygen exposure. 50 µL of each peptide solution was mixed with 50 µL of bacterial solution in a 96-well plate and the experiments were performed in triplicates. The plates were incubated 48 hrs under constant shaking at 100 rpm. The MIC was determined at the peptide concentration in which OD reading is below 0.06 and no cloudiness was visible to naked eyes. For all MIC tests, bacterial culture without peptides was used as a negative control. Gentamicin was used as the positive control that helps validate the MIC assay. Gentamicin is efficacious against *E.coli* and *S. aureus* although the MIC is shifted higher in anaerobic versus aerobic conditions.

Bacterial culture without peptides were used as a negative control. Gentamicin was used as the positive control that helps validate the MIC assay. Gentamicin is efficacious against *E.coli* and *S. aureus* although the MIC is shifted higher in anaerobic versus aerobic conditions.[1]

5. Scanning electron microscopy to examine the morphology of the bacterial membrane

400 µL bacterial suspensions (*E.coli*, 10^8 CFU/mL) were added to a 24-well plate with a cover glass (d=12 mm) placed on the bottom of each well. After 24 hrs of incubation, bacterial suspension was removed and the plates were washed with PBS buffer (pH 7.4) to remove any non-adherent bacteria. 100 µL of fresh MHB media (pH 5.7) and 100 µL of 40 µM peptide solution in MES buffer (pH 5.7, 20 mM) were mixed and added in each well and incubated at 37 ^{o}C for 1 hr. The media were removed and the cover glasses were washed with Tris buffer for

three times. Bacteria were fixed using 4% glutaraldehyde solution for overnight. The cover glasses were further dehydrated using a series of graded ethanol solutions from 35, 50, 75, 90, 95 and 100% (contents of ethanol volume). Samples were placed on a carbon tape and further coated with a 5 nm-thick gold layer. The morphology of the bacteria with and without peptide treatments were observed using a field emission scanning electron microscope operated at an accelerating voltage of 1.0 kV and a working distance of 5.8 mm.

6. Live and dead bacterial assay

400 µL of bacterial suspensions (*E.coli*, 10^8 CFU/mL) was added to confocal dish and incubated at 37 ^oC for 24 hrs. Bacterial suspensions were removed from the confocal dish and washed with PBS buffer (pH 7.4) for three times to remove any non-adherent bacteria. 100 µL of fresh MHB media and 100 µL of 40 µM peptide solution in either Tris buffer (pH 7.4, 20 mM) or MES buffer (pH 5.7, 20 mM) was added sequentially in the confocal dish. After incubation at 37 ^oC for 3 hrs, the culture media were removed and washed with PBS buffer (pH 7.4) for three times. Bacteria were stained with live/dead bacteria assay kit solution at room temperature for 15 min. Finally, bacteria were washed with PBS buffer (pH 7.4) for three times. Images were captured with epifluorescence and processed with ImageJ software.

7. Membrane localization assay

Bacterial suspensions (*E.coli*, 10^8 CFU/mL) were added to a confocal dish. After 24 hrs of incubation, bacterial suspensions were removed and confocal dish was washed with PBS buffer (pH 7.4) for three times to remove any non-adherent bacteria. Next, 100 µL of MHB media and 100 µL of 7% FITC-labeled peptides were added to confocal dish to reach a concentration at 40 µM. After 3 hrs of incubation, bacteria were washed with PBS (pH 7.4) for three times. Bacteria were stained with PI at room temperature for 15 min. Finally, bacteria were washed with PBS buffer (pH 7.4) for three times. Images were captured using a fluorescence microscope and processed with ImageJ software.

8. Hemolytic activity test

Human red blood cells (RBCs) were donated from a volunteer and 4% of human RBCs were prepared in PBS buffer (pH 7.4). 20 µL of peptide solution at various concentrations (1600, 800, 400, 200, 100, 50, and 25 µM) were prepared in PBS buffer (pH 7.4). Peptides were mixed with

180 µL of RBC suspensions in a 1.5 mL Eppendorf tube. The mixtures were incubated at 37 ºC for 1 hr, followed by centrifugation at 3000 g for 5 mins. 100 µL of the supernatant was taken out and transferred to a 96-well plate. Hemoglobin release was determined by measuring the absorbance of the supernatant at 540 nm on a microplate reader (Vitor2 1420 Multilabel Counter, PerkinElmer). RBCs treated with 1% Triton-X served as positive controls and untreated RBCs served as a negative control group. Each sample was tested in three replicates. The percentage of hemolysis remained is calculated using the following equation

$$\% \text{ hemolysis} = (A_{\text{peptide}} - A_{\text{negative control}}) / (A_{\text{Triton X}} - A_{\text{negative control}}) \times 100$$

in which the negative control group contains RBC suspension mixed with PBS buffer without peptides.

9. Cytotoxicity measurement

NIH/3T3 cells were seeded onto a 96-well plate at a density of 10^4 cells/well and incubated for 24 hrs at 37 °C in an incubator with 5% of CO_2. After 24 hrs, the culture medium was removed. 10 µL of peptide solution at various concentrations (800, 400, 200, 100, 50, 25, 12.5 µM) was mixed with 90 µL fresh culture medium in a 96-well plate. After 24 hrs of incubation, the MTT assay was performed to quantify the cell viability by monitoring the UV absorbance at 490 nm. Cell culture without peptides were used as a negative control. All the experiments were performed in four replicates.

10. Measurement of the microenvironmental pH in bacterial colonies

The pH value of the *B. fragilis* living milieu was measured using a pH ratiometric fluorescence imaging probe based on our previous publication with minor modification.[2] First, probes in PBS (0.5mg/mL) with different pH values were dropped on surface of the blank TSAB (Trptic Soy Agar with 5% sheep blood) plate, imaged with an *in vivo* Kodak imager (Ex 630nm, Em 700 nm, Exposure time 10s; Ex 760nm, Em 830 nm, Exposure time 10s). The results were analyzed to acquire a correlation curve between fluorescence ratio and indicated pH value and further plotted as a standard curve. Secondly, probes suspended in DI water (0.5mg/mL) were dropped on individual *B. fragilis* colonies on a TSAB plate and the plate without bacteria (as a control) and were imaged with the same protocol. The pH around bacterial colonies was determined based on the standard curve established above.

11. Statistical analysis

All data were expressed as means ± standard deviation (SD). The statistical analysis was performed using Student's T-test and one-way analysis of variance (ANOVA) at confidence levels of 95%.

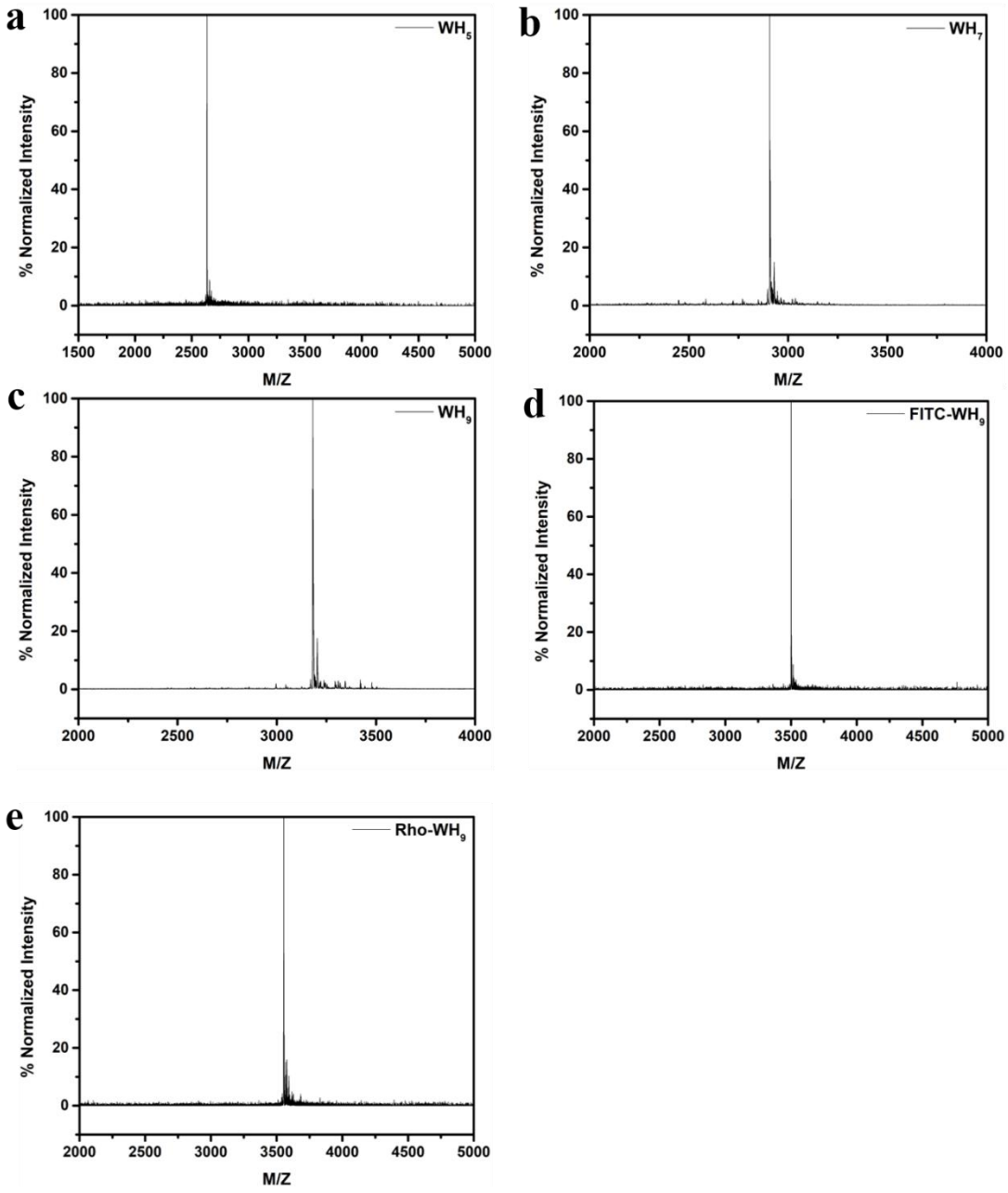

Figure S1. MALDI spectra of WH_5 (a), WH_7 (b), WH_9 (c), FITC-WH_9 (d) and Rho-WH_9 (e).

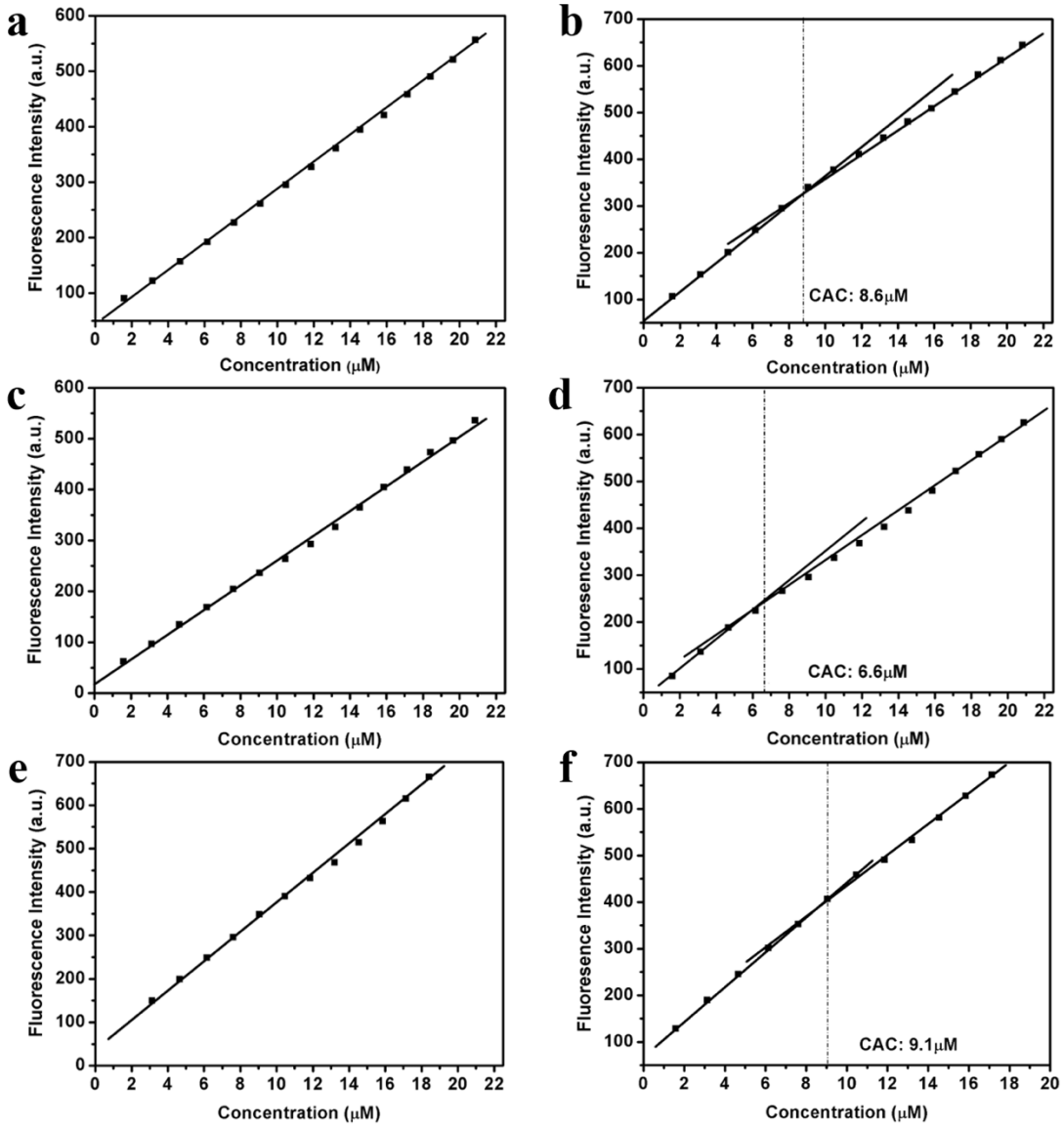

Figure S2. CAC determination by monitoring the tryptophan fluorescence at various peptide concentrations at pH 7.4 and pH 5.7. WH_5 at (**a**) and pH 5.7 (**b**) pH 7.4; WH_7 at (**c**) pH 5.7 and (**d**) pH 7.4; WH_9 at (**e**) pH 5.7 and (**f**) pH 7.4.

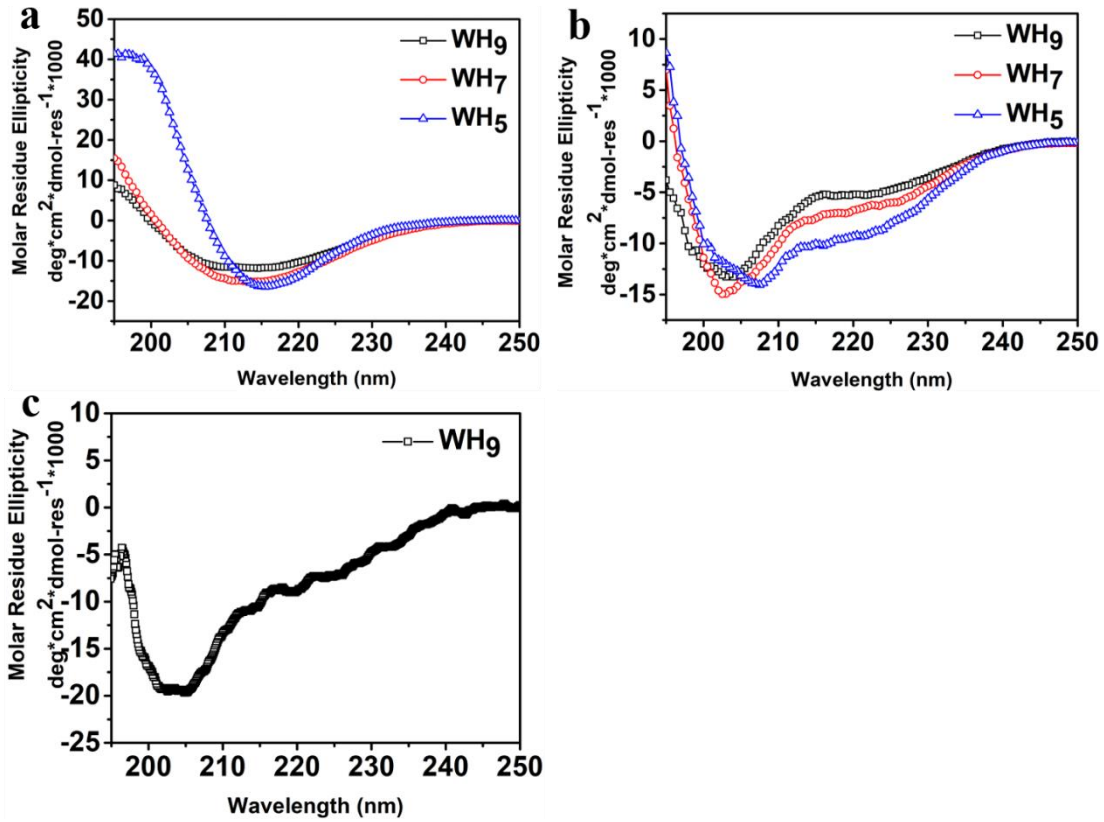

Figure S3. pH-dependent peptide secondary structures by CD spectroscopy at RT. (a) CD spectra of peptides showing predominant β-sheet secondary structures in Tris buffer (pH 7.4, 20 mM); (b) CD spectra of peptides in MES buffer (pH 5.7, 20 mM) showing weak helices/random coils; (c) CD spectrm of the filtrate of WH_9 in MES buffer (pH 5.7, 20 mM) showing a random coiled strcuture. Peptide concentration: 50 μM.

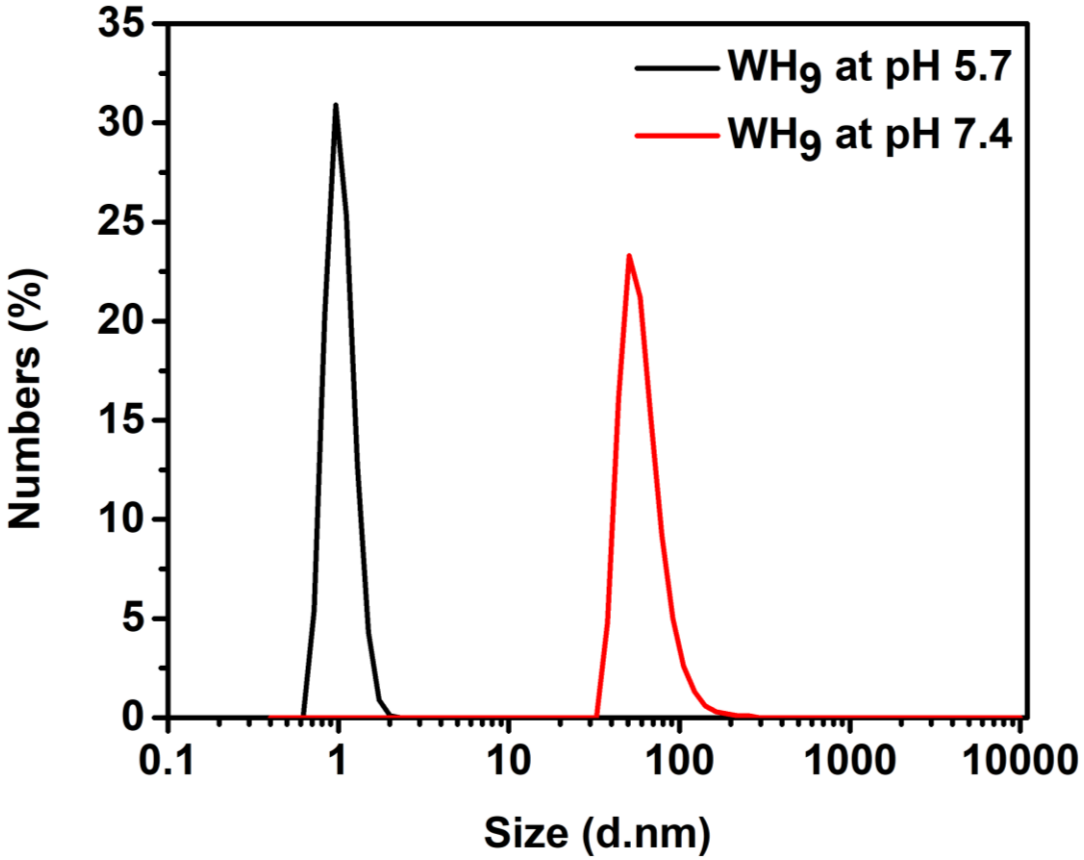

Figure S4. Particle size distribution by numbers (%) of WH_9 at neutral and acidic condition.

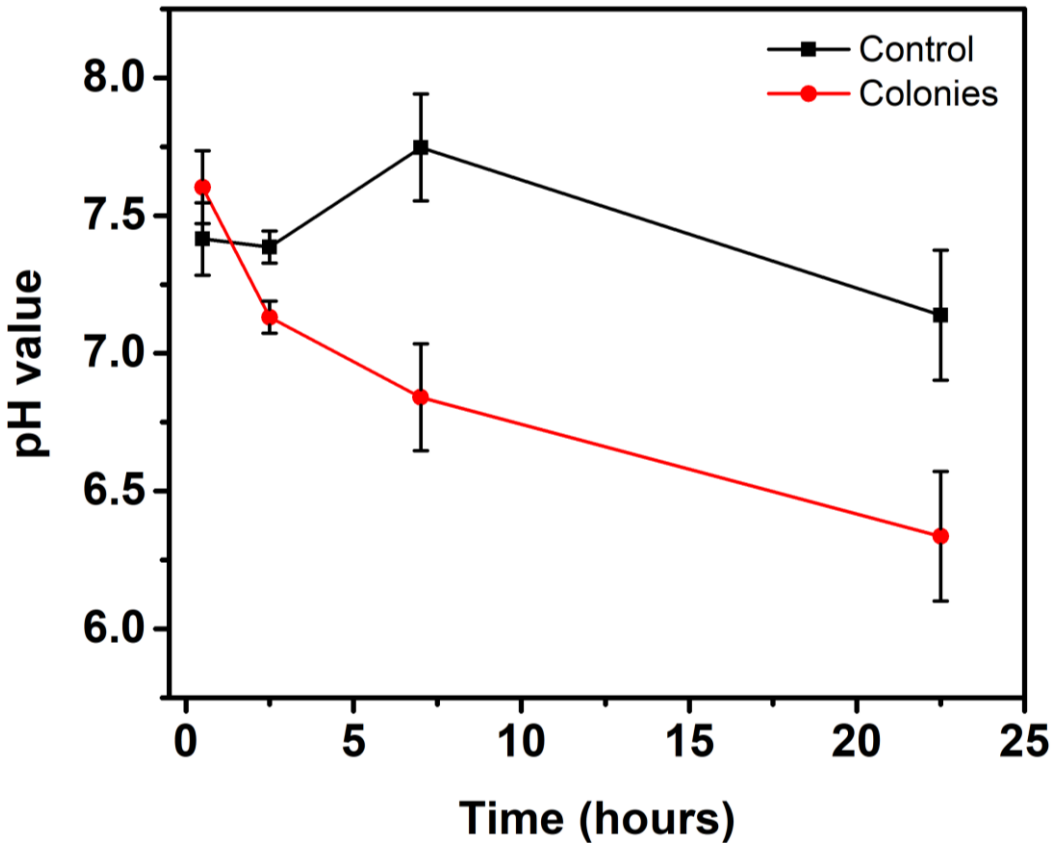

Figure S5. Time-dependent local pH of *B. fragilis* on the agar plate.

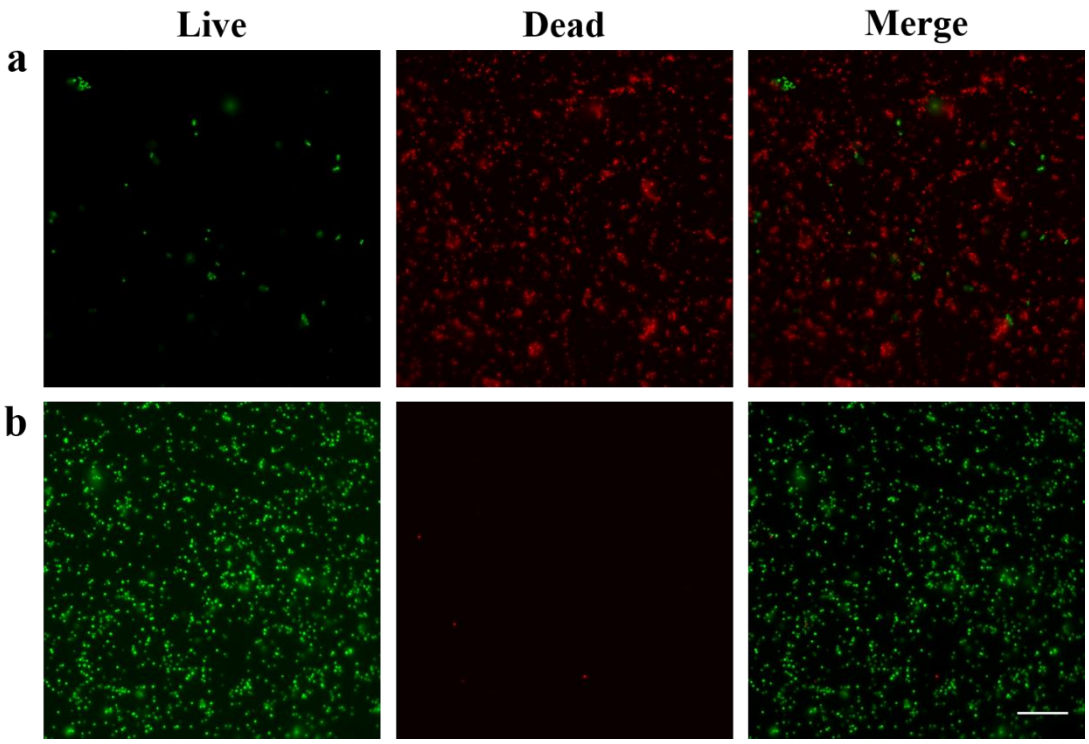

Figure S6. Fluorescence images of Live/dead bacterial assay results. Top panel: S.aureus treated with 10 µM WH9 at (a) pH 5.7 and (b) pH 7.4 for 3hrs. Live bacteria were stained with SYTO9 (green) and dead bacteria was stained with PI (red). Scale bar: 20 µm.

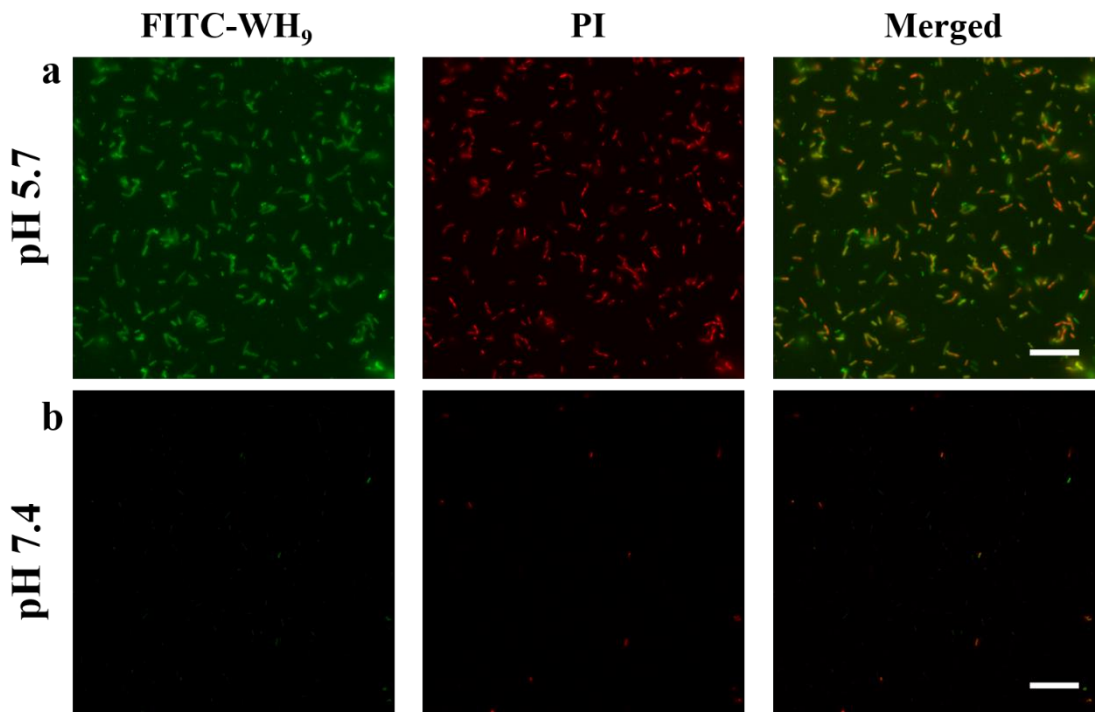

Figure S7. Fluorescence images of *E.coli* treated with FITC-WH_9 followed by PI staining in (**a**) acidic (pH 5.7) and (**b**) neutral culture condition (pH 7.4). FITC-WH_9 was found to attach on the bacterial membrane in the acidic condition, causing membrane disruption and bacterial death as stained by PI. Scale: 20 μm.

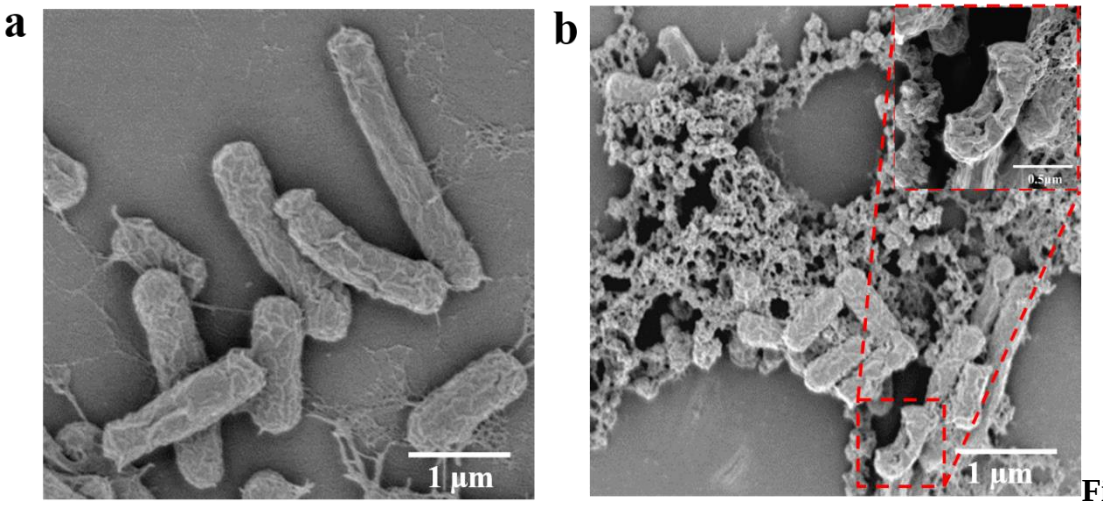

Figure S8. SEM images showing the morphological change of *E. coli* with and without peptide treatment in the acidic condition. **a**) *E. coli* without peptide treatment at pH 5.7. **b**) *E. coli* upon WH_9 incubation (2x MIC) for 1 hr at pH 5.7. The inset picture shows the damage of bacterial membrane upon peptide treatment.

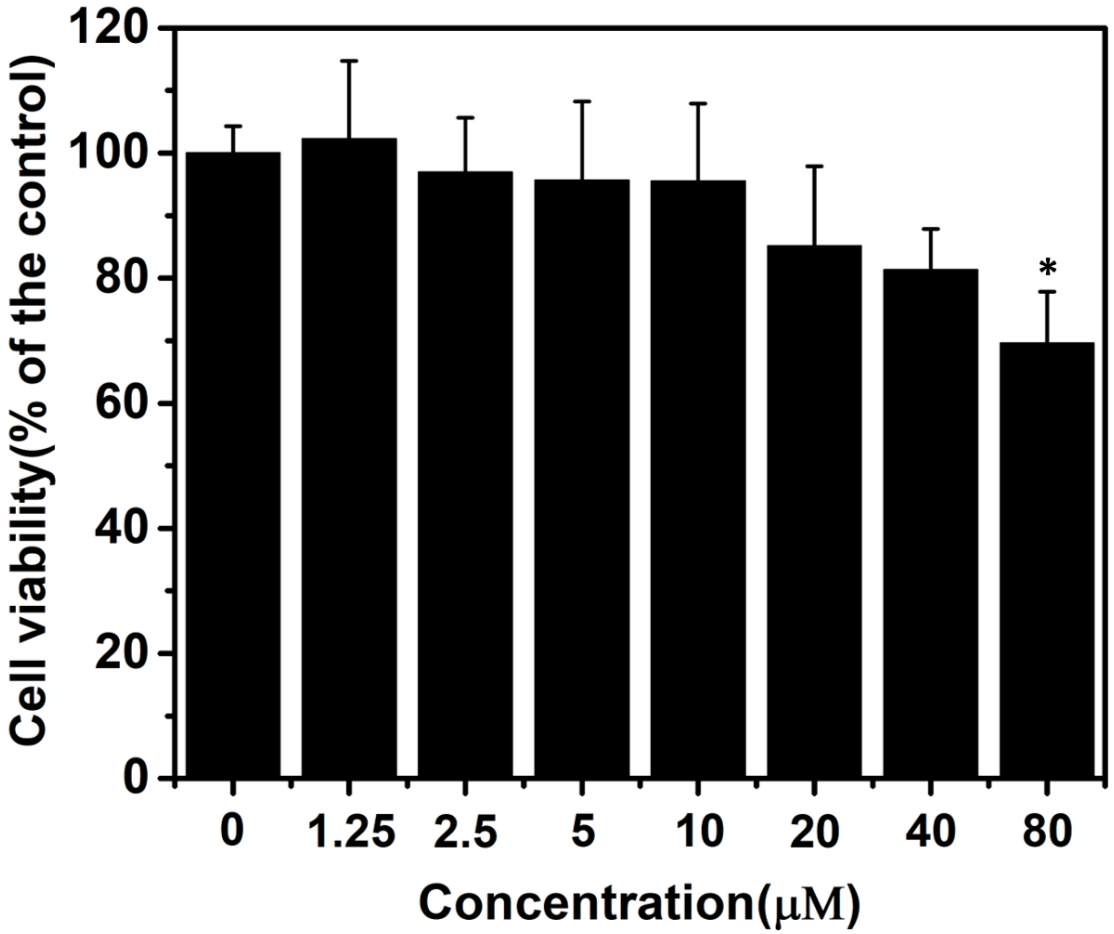

Figure S9. NIH/3T3 cell viability of peptide-treated cells in relative to the control group without peptides after 24 hrs of incubation with WH_9 at various concentrations. Statistic significant difference are indicated by *$p < 0.05$.

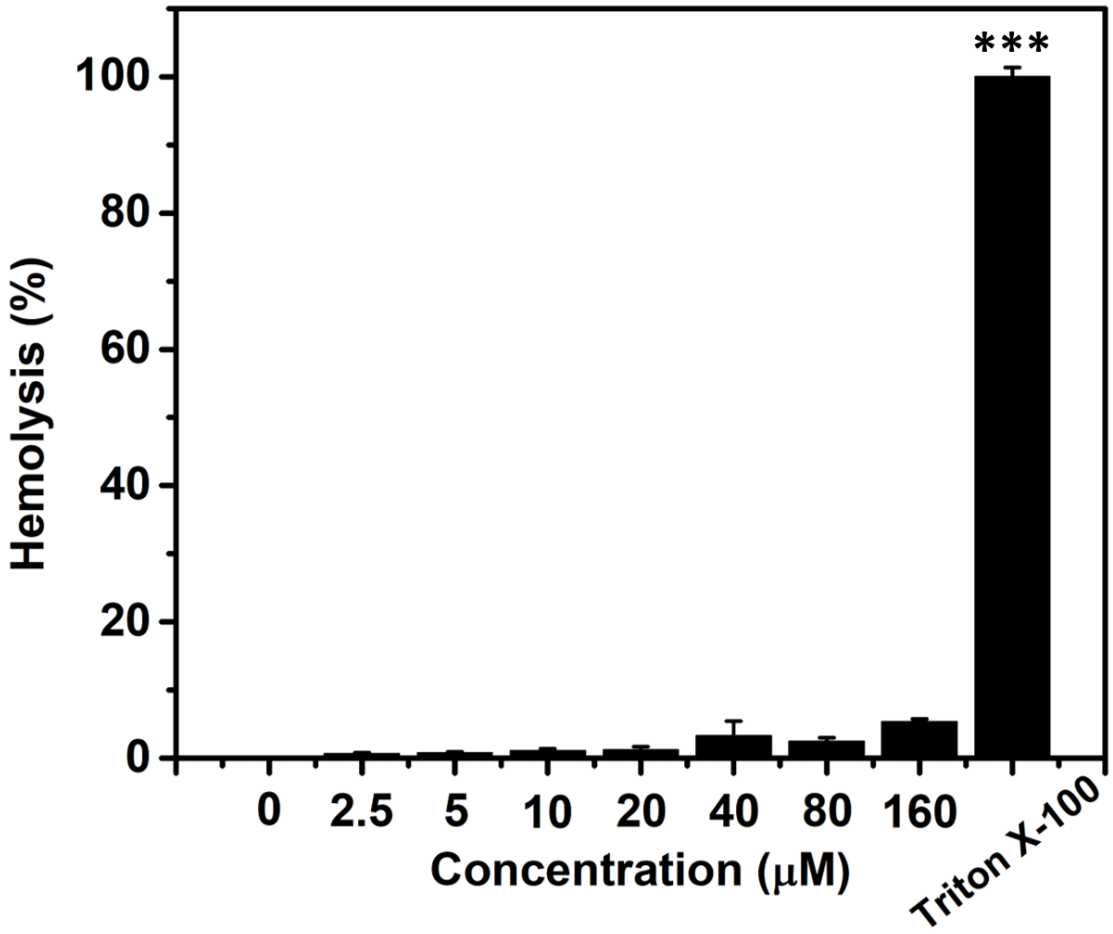

Figure S10. The percentage of hemolysis induced by WH_9 at various peptide concentrations. Statistic significant difference are indicated by ***$p < 0.001$.

1 (a) Z. DeMars, S. Biswas, R. G. Amachawadi, D. G. Renter and V. V. Volkova, *PLOS ONE* 2016, ***11***, e0155599; (b) L. J. Harrell and J. B. Evans, *Antimicrob. Agents Chemother.* 1978, ***14***, 927.

2 Y.-T. Tsai, J. Zhou, H. Weng, J. Shen, L. Tang and W.-J. Hu, *Adv. Healthc. Mater.* 2014, ***3***, 221.

Chapter 3. Injectable Click Chemistry-based Bioadhesives for Accelerated Wound Closure

Shuxin Li,[1] Jun Zhou,[1] YiHui Huang,[1] Joyita Roy,[1] Ning Zhou,[3] Kyungsuk Yum,[2] Xiankai Sun,[3] Liping Tang[1]*

1. Department of Bioengineering, University of Texas at Arlington, Arlington, TX 76019, USA
2. Department of Materials Science and Engineering, University of Texas at Arlington, Arlington, TX 76019, USA
3. Department of Radiology, The University of Texas Southwestern Medical, Dallas, TX 75390, USA

* Corresponding author. Department of Bioengineering, University of Texas at Arlington, P.O. Box 19138, Arlington, TX 76019-0138, USA. Tel.: +1 817 272 6075; fax: +1 817 272 2251. E-mail address: ltang@uta.edu.

Abstract

Tissue adhesives play a vital role in surgical process as a substitution of sutures for wound closure. However, most currently existing tissue adhesives suffer cell toxicity, weak adhesive strength to tissue, and costly. Herein, by taking advantage of the fast and specific inverse-demand Diels-Alder cycloaddition reaction, a series of bioadhesive were produced by employing copper-free click chemistry pair trans-cyclooctene (TCO) /tetrazine (Tz) in the chitosan. The gelation time of the bioadhesives can be optimized to be less than 2 minutes, which meets the need for surgical wound closure in practice. With the adding of 4-arm polyethylene glycol propionaldehyde (PEG-PALD) as a co-crosslinker, the adhesive strength of the bioadhesives is optimized to be 2.7 times higher than that of the conventional fibrin glue. Moreover, by adjusting the amount of the co-crosslinker, the swelling ratio and pore size of the chitosan bioadhesives can be tuned to fit the need of drug encapsulation and cell seeding. The chitosan bioadhesives possess excellent *in vitro* cytocompatibility. Through a mice skin incision wound model, we proved that the chitosan bioadhesives was able to close the wound faster and promote wound healing process faster than the fibrin glue. In conclusion, our results support that the innovative click-chemistry based bioadhesives have been developed with improved physical and biological properties for surgical wound closures.

Keywords: Bioadhesives, click chemistry, Chitosan, Hydrogel, Wound healing.

Statement of Significance

The manuscript describes a new group of click chemistry-based chitosan bioadhesives fabricated by reacting copper-free click chemistry pair trans-cyclooctene/tetrazine with co-crosslinker PEG-PALD. The new bioadhesives possess the properties of simple preparation, injectability, fast gelation, a minimal cytotoxicity, strong adhesive strength to tissue, and enhanced wound healing responses. This innovative strategy may draw interests of readers from the field of biomaterials, drug delivery, surgical device, and translational medicine.

1. Introduction

Tissue adhesives, a common adjunct in surgical practice, have been widely used in dentistry [1, 2], orthopedics [3, 4], and cardiovascular wounds closure [5] to replace the traditional suturing approach due to the decreased foreign body reactions and no need for further removal [6]. However, many of the existing commercial tissue adhesives have their individual flaws upon application. For example, cyanoacrylate (Super Glue), which is considered as the strongest tissue adhesive, has been shown to possess strong cytotoxicity [7, 8]. Moreover, since it transforms to rigid plastics immediately after exposure to water, it is not suitable for wet tissue application [9]. Fibrin glue (TISSEEL, Baxter) and polyethylene glycol adhesives (COSEAL, Baxter) are widely used due to their fast closure process and biodegradability [10, 11]. However, both glues have limited application due to their poor adhesive property and tensile strength [12]. Recently mussel-inspired adhesives have become a popular topic in the research field due to its strong adhesion strength on a wet surface mimicking the blue mussel [13-15]. Nevertheless, since prohibitive compounds such as dopamine have to be used and the neurological effects of dopamine remain

risky [16], such dopamine-based bioadhesives are still not acceptable for clinical application. Therefore, tissue adhesives with strong adhesion strength, biodegradability, low cytotoxicity, and can be applied on a wet surface remain highly desirable.

The adhesion strength mainly relies on two factors: the cohesive strength within the bioadhesives and the adhesive strength between the bioadhesives and the tissue surface [17]. To increase the cohesive strength, click chemistry is considered as a practical tool in materials chemistry due to its fast reaction, high yield, and biocompatible byproducts under wet condition. The bi-orthogonal click chemistries have been used widely in cell labeling [18], imaging [19], cell surface modification [20], and drug delivery [21]. To avoid using the copper catalysts which are commonly used in click reactions and harmful to cells [22], tetrazine/trans-cyclooctene was chosen as a ligation pair due to its high chemo selectivity and ultrafast kinetics [23]. A dihydropyridazine bond was then formed between the ligation pair through an inverse-demand Diels-Alder cycloaddition reaction.

To increase the adhesive strength, chitosan (CS) has been selected as the backbone of the bioadhesives. Chitosan, bio-based polysaccharides extracted from deacetylated chitin, has been developed as a good candidate for bioadhesives due to its good mechanical properties, biocompatibility, biodegradability, and antimicrobial property [24, 25]. Moreover, as the primary amine becomes positive charged NH_3^+ at acidic pH (<6.5) [26], a chitosan can interact with a negatively charged surface of tissues under wet condition through not only electrostatic force but also hydrogen bonds and van der Waals force [27]. Additionally, due to its natural hemostatic properties, chitosan-based materials have been used for skin wound closure in many previous publications [28-30]. Hence, chitosan was applied as the main component of the synthesized bioadhesives.

To further strengthen both the cohesive strength and adhesive strength, PEG-PALD was added into the bioadhesives as a co-crosslinker. Under an acidic milieu, aldehydes can react with primary amines from both chitosan and tissue proteins and form imine derivatives which is also known as Schiff bases (compounds with C=N) [31]. Consequently, the covalent bond formed within the bioadhesives and between the bioadhesives and the tissues may significantly increase the cohesive strength and adhesive strength, respectively.

Here, we present a click chemistry enhanced and dual crosslinked chitosan bioadhesive as a new strategy for wound closure with strong adhesive strength, injectability, and biocompatibility. In detail, CS-TCO and CS-Tz precursors were synthesized through carboxyl-to-amine crosslinking (scheme 1). Upon administration, 4-arm PEG-PALD was mixed with one of the precursors and both of the precursors were injected and mixed within the wound (scheme 1, 2). The crosslinking of the CS was through both the rapid reaction between conjugated click chemistry pair TCO/Tz and the formation of Schiff bases between PEG-PALD and primary amines on CS. The mixture can form a solid hydrogel within 2 minutes. By optimizing the dosage of the co-crosslinker, adhesive strength, rheology, swelling ratio, and pore size of the hydrogel were characterized and compared, and the recipe that had the strongest adhesive strength was chosen for further animal study. Precursors and the formed hydrogel were tested to be free of cytotoxicity. With a mice skin incision wound healing model, the bioadhesives showed significantly better wound closure and wound healing outcome compared with commercial fibrin glue (TISSEEL, Baxter). With further development, there is a great potential for these bioadhesives to be further developed and utilized as a regular wound closure tool.

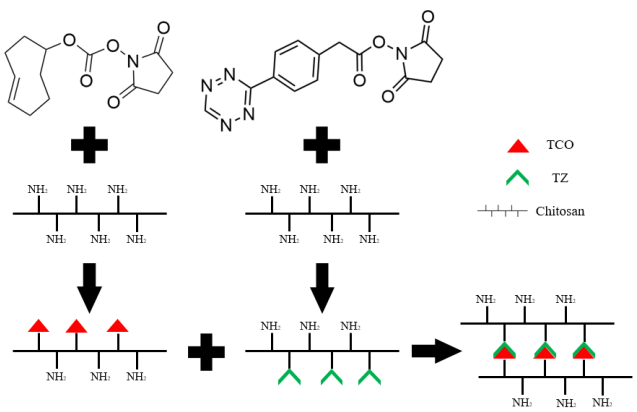

Scheme 1. Step-by-step synthesis of the precursors and crosslinking of CS bioadhesives.

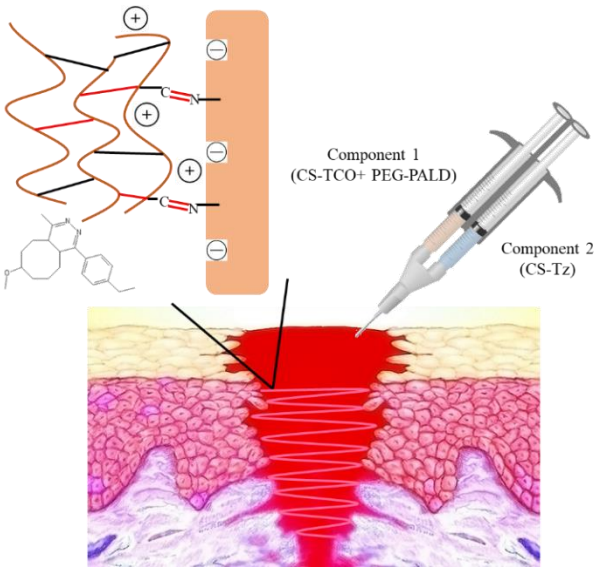

Scheme 2. A depiction of the bonding structure between the CS bioadhesives and surrounding tissue.

2. Materials and methods

2.1 Materials

Low-molecular-weight chitosan was purchased from MilliporeSigma (St. Louis, MO). TCO-NHS Ester and Tz-NHS Ester were purchased from Click Chemistry Tools (Scottsdale, AZ). 4-arm PEG-PALD (10kDa) was purchased from Laysanbio (Arab, AL).

2.2 Synthesis and characterization of CS bioadhesives

Two precursors of the CS bioadhesives, CS-TCO and CS-Tz, were synthesized through carbodiimide crosslinking between primary amine groups on the chitosan and NHS groups on TCO/Tz-NHS Ester. Briefly, 2mL TCO/Tz-NHS solution (62mM, dimethyl sulfoxide) was added into 2mL chitosan solution (10 mg/mL, 50mM MES buffer, pH 6.0) which resulted in an equivalent molar of NHS and a primary amine. The reaction was carried out through constant stirring in the dark for overnight. For purification, conjugated CS was precipitated through excessive acetone and unconjugated TCO/TZ was washed off with dimethylformamide. The precipitated conjugated CS were dissolved in 20ml of 1% acetic acid solution and further purified

with exhaustive dialysis (molecular cutoff: 2 kDa) against 1% acetic acid solution and subsequently against water. The CS-TCO and CS-Tz were lyophilized and stored at 4 ^{o}C for further use. To quantify the degree of substitution (DS) of TCO and Tz, 0.5% (w/v) solution of CS, CS-TCO, CS-Tz in 1.75% DCl D_2O solution were placed into three 5-mm-outside diameter tubes and analyzed by ^{1}H NMR using a 400 MHz Varian VNMRS direct drive Varian console spectrometer (Varian Medical Systems, Palo Alto, CA). Lyophilized CS-TCO and CS-Tz were dissolved to 10mg/mL and 6.67 mg/mL in 50mM MES buffer respectively for further experiments.

2.3 Assessment of gelation times

Gelation times were tested through test-tube tilting method as reported before [32]. Briefly, a total volume of 100μL of TCO/TZ-CS solution was added into a glass tube with different formulations (see Table 1). The tube was gently rocked until the solution lost its mobility and the time was recorded. The experiments were done under room temperature and repeated three times.

2.4 Adhesive strength measurement

The adhesive strength of the bioadhesives with different formulations was tested and compared through a porcine skin model [33]. Briefly, fatty-layer-free porcine skin was sliced into 1X3 cm^2. 25μL of one component solution of bioadhesives was put on the dermal side of each skin slice, and then the same volume of another component solution was mixed together on the skin slice. For groups with PEG-PALD crosslinker, the crosslinker was mixed with one of the two component solutions. Two skins were then overlapped to a bonding area of 1x1 cm^2. After loading a weight of 50 g for 10 minutes, the skin was placed in 4°C overnight for thorough reaction. The adhesive strength was measured using MTS electromechanical tension system (MTS Systems

Corporation, MN, USA) under 10 mm/min preload stress speed at room temperature. Adhesion strength was calculated in a method of dividing the maximum load by overlapping contact area. All the measurements were repeated at least 3 times in order to get statistic results and fibrin glue was also measured under the same condition as a control.

2.5 Rheological properties of the precursors and the CS bioadhesives

Rheological tests were carried out by using a DHR-2 rheometer (TA instruments, New Castle, DE) in a parallel plate configuration by employing sandblasted stainless steel 20 mm diameter plates and a Peltier plate for temperature control. The injectability of the two precursors was tested through the viscosity response upon application of shear. Viscosities of CS-TCO (10 mg/mL) and CS-Tz (6.67 mg/mL) were measured in a viscosity flow sweep with a change of shear rate from 0.1-500 1/s. To test the rapid gelation process through the click chemistry reaction, viscosities of the two precursors and a mixture of the two precursors were measured over time under a flow peak hold mode (shear rate 0.5 1/s). Moreover, the effect of PEG-PALD addition on the bioadhesive's mechanical strength were also investigated through monitoring the change of storage modulus and loss modulus against frequency sweeping under a constant strain (5%). All experiments were carried out within the linear viscoelastic region.

2.6 Properties of the CS bioadhesives

Swelling ratios and pore sizes of the CS bioadhesives were studied. Swelling ratios of the CS bioadhesives were tested based on the existing protocol with minor modification [34]. The swelling ratio can be calculated by using the following formula: Swelling ratio (%) = $(W_s - W_d)/W_d \times 100\%$, where W_s equals to the weight of the bioadhesives after swelling in DI water and W_d

equals to the weight of dried bioadhesives after swelling. Each group was repeated three times to get the statistic result. The pore sizes of the CS bioadhesives with different crosslink densities were observed by using a scanning electron microscope (Hitachi S-4800 II FE SEM, operating voltage 15 kV) and quantified with image J.

2.7 In vitro cytotoxicity tests of CS bioadhesives

The cytotoxicity of the two precursors and conditioned media of the CS bioadhesives was studied quantitatively using MTT assay with mice fibroblast (NIH/3T3, ATCC, Manassas, Virginia). Briefly, cells were seeded in a 96-well plate at a density of 1×10^4 cells/well and incubated with Dulbecco's modified eagle's medium (DMEM) supplemented with 10% (v/v) fetal bovine serum and 1% (v/v) penicillin-streptomycin for 24 hours in an incubator set at 5% CO_2, 37°C, and 95% relative humidity. The medium of each well was substituted with precursor-containing DMEM solutions with various concentrations (0.1, 0.01, and 0.001 mg/mL). After 24 hours of incubation, MTT assay analysis was performed as per the manufacturer's protocol. Viability of the cells was normalized to the cells cultured control medium (0 mg/mL) as a control.

For the conditioned medium toxicity tests, the CS bioadhesives (2mg) were incubated in 1.0 ml PBS (pH 7.4) in the absence/presence of lysozyme (0.8 mg/ml) for 3 days, and then the conditioned media were obtained by collecting the supernatants [35]. Three different dilutions (10x, 100x, and 1000x) of the conditioned media using DMEM were prepared and their toxicity was characterized using MTT assay under the same condition as mentioned before [34].

2.8 In vivo mice incision wound closure and healing

The *in vivo* biocompatibility and wound healing properties of the CS bioadhesives were tested using a modified mice skin incision model [36]. All experiments were performed with the approval of the University of Texas at Arlington Institutional Animal Care and Use Committee (IACUC) in accordance with the Animal Welfare Act, and consistent with the Guide for the Care and Use of Laboratory Animals. Briefly, ten Balb/c mice (6 - 8 weeks old, Taconic Farms, Inc., Germantown, NY) were anesthetized and their backs were shaved and sterilized with betadine and followed by 70% ethanol. Two linear, full thickness surgical wounds (1.3cm long) were produced on both sides of the spine (parallel and symmetric). For wounds closure, the right wound was closed by dropping sterilized CS bioadhesives (25μL of CS-TCO 10mg/mL, 25 μL of CS-Tz 6.67mg/mL, and 5μL of PEG-PALD 90mg/mL) into the wound followed by finger-clamping for about two minutes while the left wound was closed by fibrin glue as a control. One surgeon performed all the procedures in a consistent manner to minimize variations in surgical intervention. Each mouse was imaged every day to monitor the wound healing process and the length of the wound was measured using image J. On the 7^{th} and 14^{th} day post-surgery, 5 mice were sacrificed with an overdose of anesthetic at each time point and skin tissue at wound sites were excised, embedded in OCT compound, and cryosectioned for histological analysis. Hematoxylin and eosin (H&E) staining was used for morphological assessment and Masson trichrome staining was used to assess production of collagen [37]. CD11b immunohistochemistry (IHC) staining was used to evaluate infiltrated inflammatory cells [34]. Briefly, after blocking of endogenous peroxidase and non-specific binding, the tissue sections were incubated with CD11b primary antibody (1:50, rabbit anti-mouse Integrin αM, H-61, Santa Cruz Biotechnology, Santa Cruz, CA, USA) overnight at 4 ^{o}C, followed by HRP-conjugated goat anti-rabbit IgG antibody (1:500, Abcam, Cambridge,

MA, USA) incubation for 1 hour at room temperature. Diaminobenzidine (DAB, sigma, MO, USA) was used as a chromogen for color development and hematoxylin was used for counter staining. A negative control was simultaneously generated by omitting the primary antibody. Wound gap was measured through H&E stained tissue section using image J. Cell infiltration into the incision area was quantified through cell counting of H&E stained tissue sections and inflammatory cells quantification was done similarly using the CD11b IHC stained tissue sections. Collagen density was determined by calculating the ratio of blue-stained area to the whole incised area within the Masson trichrome staining images [38].

2.9 Statistical Methods

All the results will be expressed as mean ± standard error (including gelation time, adhesive strength, swelling ratio, pore size, cell viability, wound gap, wound length, cell density, inflammatory cell percentage, and collagen density). Student t-test was performed to compare the difference between groups (including unpaired t-test for cell viability of different treatments and paired t-test for wound healing status evaluation between two different treatments on the same mice). A value of $p \leq 0.05$ was considered significant.

3. Results

3.1 Synthesis and characterization of CS bioadhesives precursors

CS-TCO and CS-Tz were synthesized using carbodiimide coupling reaction between primary amine and NHS ester. Peaks assigned to TCO/Tz were also identified on the conjugated precursors. Representative spectra of ^{1}H NMR analysis of the purified precursors are depicted in Fig. 1. Compared to the spectra of CS (Fig. S1A), The chemical shifts at 2.6-3.0 ppm were assigned to protons of CH directly conjugated to primary amine/amide on each repeating unit of chitosan. The multiple peaks between 2.0 and 2.4 ppm were assigned to protons of CH_2 located next to alkene (C=C) which was the characteristic structure of TCO (Fig. 1A&S1B). Meanwhile, the multiple peaks between 7.5 and 8.2 ppm were assigned to protons of benzene ring which was the characteristic structure of Tz (Fig. 1B&S1C). The DS of the precursor CS-TCO and CS-Tz were 5% and 18.5% through comparing the area under peaks of CH_2 (next to C=C) and benzene ring protons shifts with that of assigned to protons of chitosan.

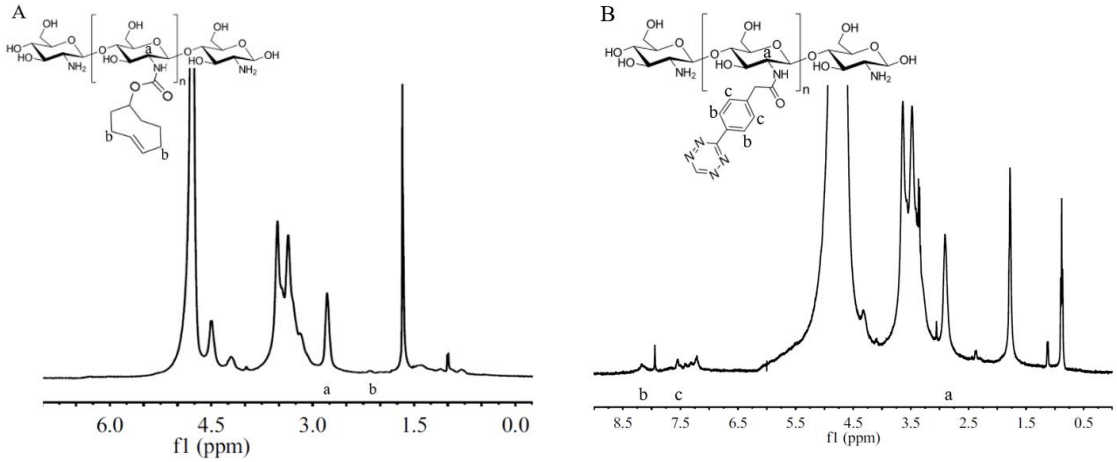

Figure 1. (A) ^{1}H-NMR spectrum of CS-TCO; (B) ^{1}H-NMR spectrum of CS-Tz.

3.2 Gelation times of CS bioadhesives

The gelation times of different formulations are shown in Table 1. By changing the ratio between CS-TCO and CS-Tz, the gelation time can go from 62 seconds to 116 seconds which revealed the fast crosslinking speed through the click chemistry reaction. It is interesting that with the adding of different concentrations of PEG-PALD, the gelation time stayed around 63 seconds. The phenomenon can be explained that the crosslinking reaction between aldehydes and primary amines required longer reaction time which didn't have much influence on instant gelation time.

Table 1. Gelation times of CS bioadhesives

Name of CS bioadhesives	Formulation	Gelation time (s)
TCO-Tz 2-3	Volume ratio TCO-Tz 40%-60%	62.33±9.53
TCO-Tz 3-2	Volume ratio TCO-Tz 60%-40%	99.67±26.03
TCO-Tz 1-4	Volume ratio TCO-Tz 20%-80%	108.67±20.07
TCO-Tz 4-1	Volume ratio TCO-Tz 80%-20%	116.33±28.41
CS-TCO-Tz-PEG 0*	Volume ratio TCO-Tz 50%-50%	85.67±14.38
CS-TCO-Tz-PEG 3*	PEG-PALD concentration 3 mg/mL	63.67±10.37
CS-TCO-Tz-PEG 9*	PEG-PALD concentration 9 mg/mL	63±4.24

* Volume ratio of TCO-Tz remains 50%-50% for these groups

3.3 Adhesion strength of the CS bioadhesives

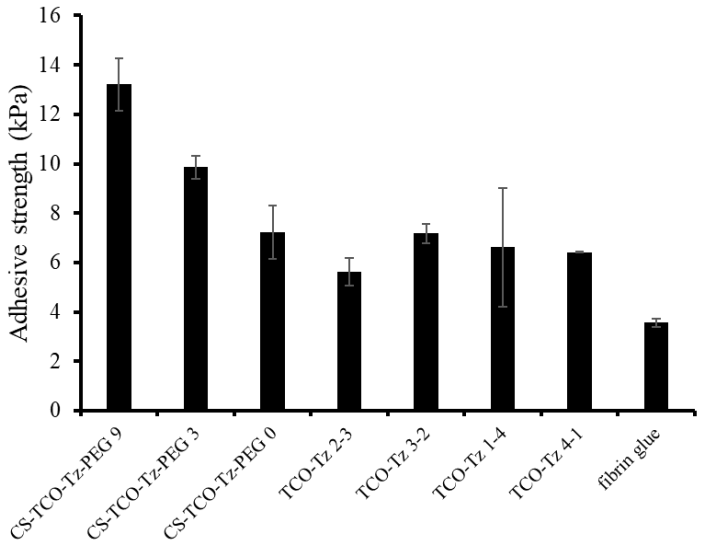

Figure 2. Adhesive strength of CS bioadhesives with different formulations, measured through porcine skin tensile test. Fibrin glue was used as a control

The adhesive strength of the CS bioadhesives with different formulations for groups of PEG-PALD concentration of 9, 3 mg/mL, volume ratio of TCO to TZ of 1-1, 2-3, 3-2, 1-4, 4-1, and fibrin sealant was measured as 13.22±1.06, 9.87±0.47, 7.23±1.08, 5.64±0.56, 7.17±0.39, 6.62±2.40, 6.42±0.007, 3.56±0.18, respectively. Without adding of PEG-PALD as a co-crosslinker, the highest adhesive strength of the CS-TCO-Tz can be reached about twice as much as fibrin sealant. After addition of PEG-PALD (9 mg/mL), the adhesive strength of the CS-TCO-Tz-PEG bioadhesives can achieve about 2.7 times higher than the fibrin sealant. The result is summarized and compared in Fig. 2.

3.4 Rheological characterization

By measuring the viscosity response upon an increase of shear rate, both precursor solutions could be characterized as shear thinning behavior fluids and thus proved their injectability (Fig. 3A). The viscosity of the precursor solutions and their mixture solution over time was investigated as shown in Fig. 3B. One can observe that viscosity of the mixture solution increased over time while that of the individual precursor solution kept unchanged (even reduced). These results indicated that the successful crosslinking occurred and the gelation time matched the

one measured via tilting tests (Fig. 3B). To study effect of PEG-PALD, different concentrations of PEG-PALD were added to CS-TCO/CS-Tz mixture. After 24 hrs, the formed adhesive hydrogels were objected to the frequency sweeping, and the result was shown in Fig. 3C. With more PEG-PALD added, the storage modulus of the adhesive hydrogel increased significantly (Fig. 3C).

By combing the results of adhesive test and rheological analysis, it might be rationalized that addition of PEG-PALD can improve not only adhesive strength (covalent bonding formation

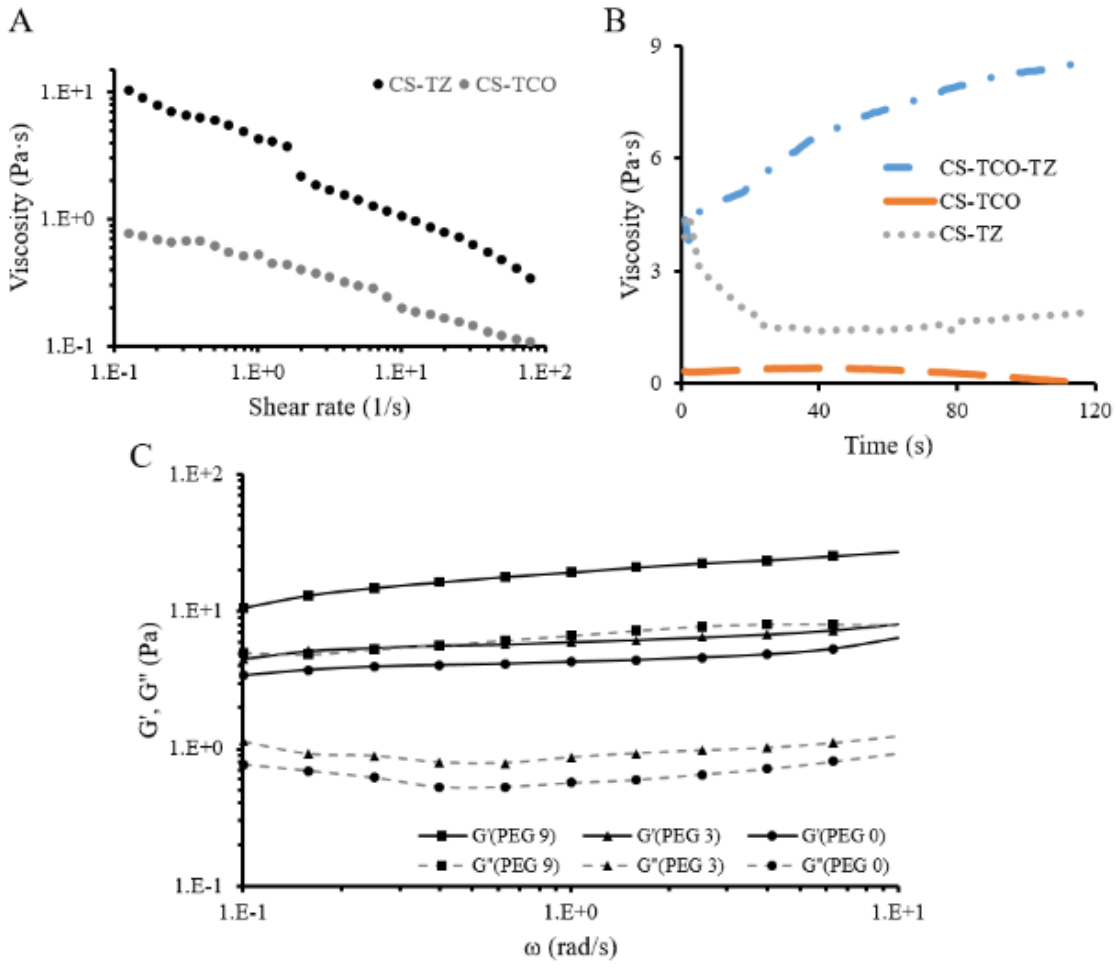

Figure 3. Rheological evaluation of precursors and CS bioadhesives. (A) Injectability test of precursors; (B) Viscosity change over gelation process; (C) G' and G'' of CS bioadhesives with different concentrations of PEG-PALD.

between amino groups on tissue surface and –CHO groups of PEG), but also cohesive strength (increasing crosslinking density of CS adhesives).

3.5 Swelling ratio and pore size of the CS bioadhesives

By increasing the concentration of PEG-PALD, we find that the swelling ratio of the CS bioadhesives decrease d significantly from 891.8 % to 496.8 % which suggest the increase of the

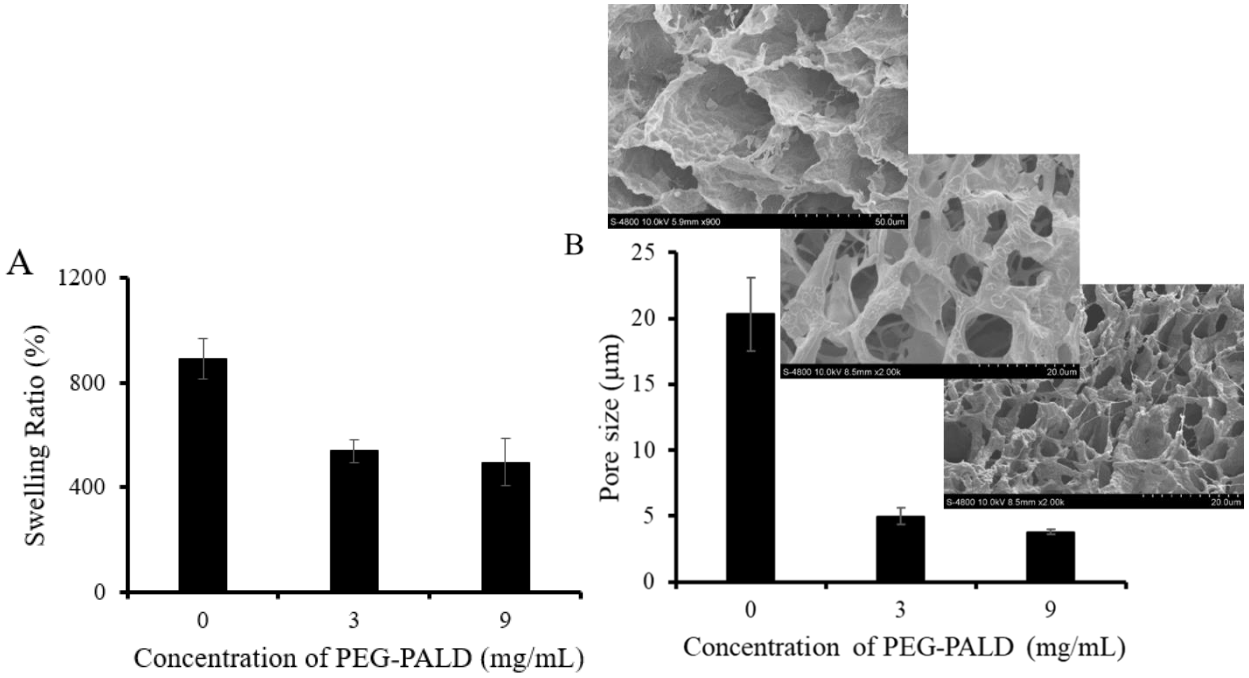

Figure 4. Optimization of swelling ratios and pore sizes. (A) swelling ratio of CS bioadhesives with different amount of PEG-PALD; (B) Pore size of CS bioadhesives with different amount of PEG-PALD measured by SEM.

crosslinking densities (Fig. 4A). Coincidentally, SEM studies also confirm that the increase of PEG-PALD concentrations decrease the pore size of the lyophilized CS bioadhesives from 20 μm to 3.8 μm possibly caused by the increasing crosslinking densities (Fig. 4B).

3.6 In vitro cytotoxicity evaluations of CS bioadhesives

For *in vitro* study, no significant cytotoxicity was seen for both the precursors polymers (up to 0.1mg/mL) (Fig. 5A) and the leachable content (up to 10X dilution) of the CS bioadhesives (Fig. 5B). There is a mild toxicity found in the conditioned medium of CS-TCO-Tz-PEG 9 lysozyme group and that is possibly due to existence of the residual lysozyme as well as non-reacted PEG-PALD.

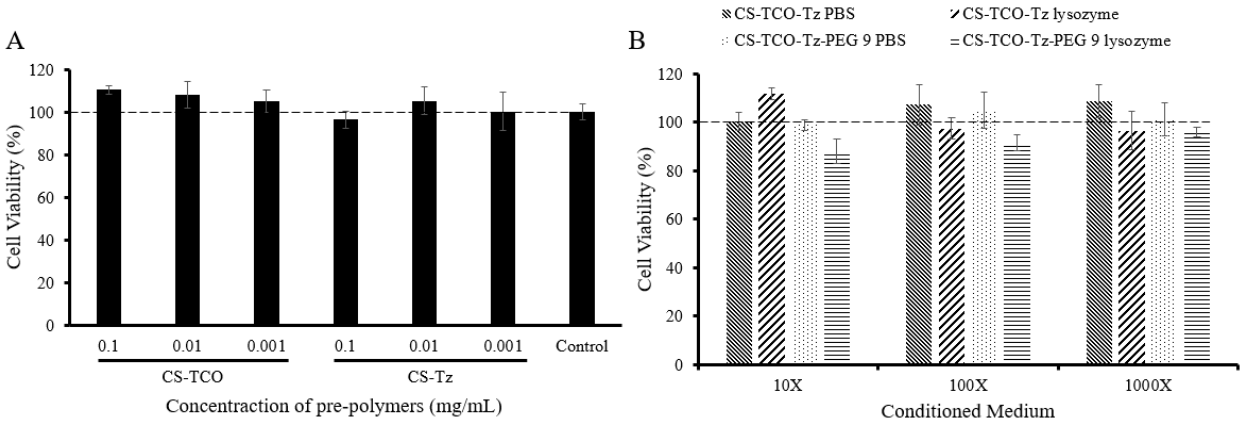

Figure 5. Cell toxicity characterization of the bioadhesive precursors and conditioned media of the CS bioadhesives. (A) Cytotoxicity of different concentrations of the precursors; (B) Cytotoxicity of different concentrations of the conditioned media. Results were acquired through MTT assay using NIH/3T3 fibroblasts and were normalized to the control group.

3.7 In vivo mice incision wound closure and healing

The adhesive property and tissue compatibility was evaluated using a mouse incisional skin wound model. After implantation for different periods of time, wound sites were isolated and histologically evaluated. After implantation for one weeks, the wounds closed by CS bioadhesives were found to have significantly smaller wound gaps than those wounds closed fibrin glue (0.668± 0.225 mm vs. 1.922±0.429 mm) (Fig. 6A). Also, over time, the wound sizes decreased and, ever since day 4 post-incision, wounds closed by CS bioadhesives were 0.22 ~ 0.32 cm shorter than those closed by fibrin glue (Fig. 6B&S2). The morphological evaluation (H&E staining) of both treatment groups showed the granulation tissue on day 7 (Fig. 6C 1st week) and skin

epidermalization on day 14 (Fig. 6C 2nd week). Interestingly, we find that the treatment of CS bioadhesive improve skin epidermalization with more hair follicle regrowth at the incision area than those treated with the fibrin glue group. There were no significant differences in cell densities at the incision area between two treatment groups - CS bioadhesives (day 7: 10,900±1,600 #/mm^2; day 14: 8,700±2,600 #/mm^2) and fibrin glue (day 7: 12,000±4,200 #/mm^2; day 14: 8,300±1,100 #/mm^2) (Fig. 6C). Similarly, the percentages of CD11b positive inflammatory cells in the incisions area at 7th and 14th day post-surgery were not significantly different between CS bioadhesives treated group (day 7: 27.0±0.5%; day 14: 7.3±2.1%) and fibrin glue treated group (day 7: 29.1±6.2%; day 14: 11.4±1.9%) (Fig. 6D). Nevertheless, a significantly higher amount of collagen was found at the site of CS bioadhesives treated wounds (day 7: 45.3±5.9%; day 14: 61.0±7.0%) than the one treated with fibrin glue (day 7: 25.9±5.7%; day 14: 44.6±5.9%) on both day 7 and 14 (Fig. 6E). Interestingly, the amount of collagen at the CS bioadhesive treated site on day 7 was almost equivalent to that fibrin glue treated site on day 14 which indicated that the CS bioadhesives may have accelerated the wound healing process by approximately 7 days.

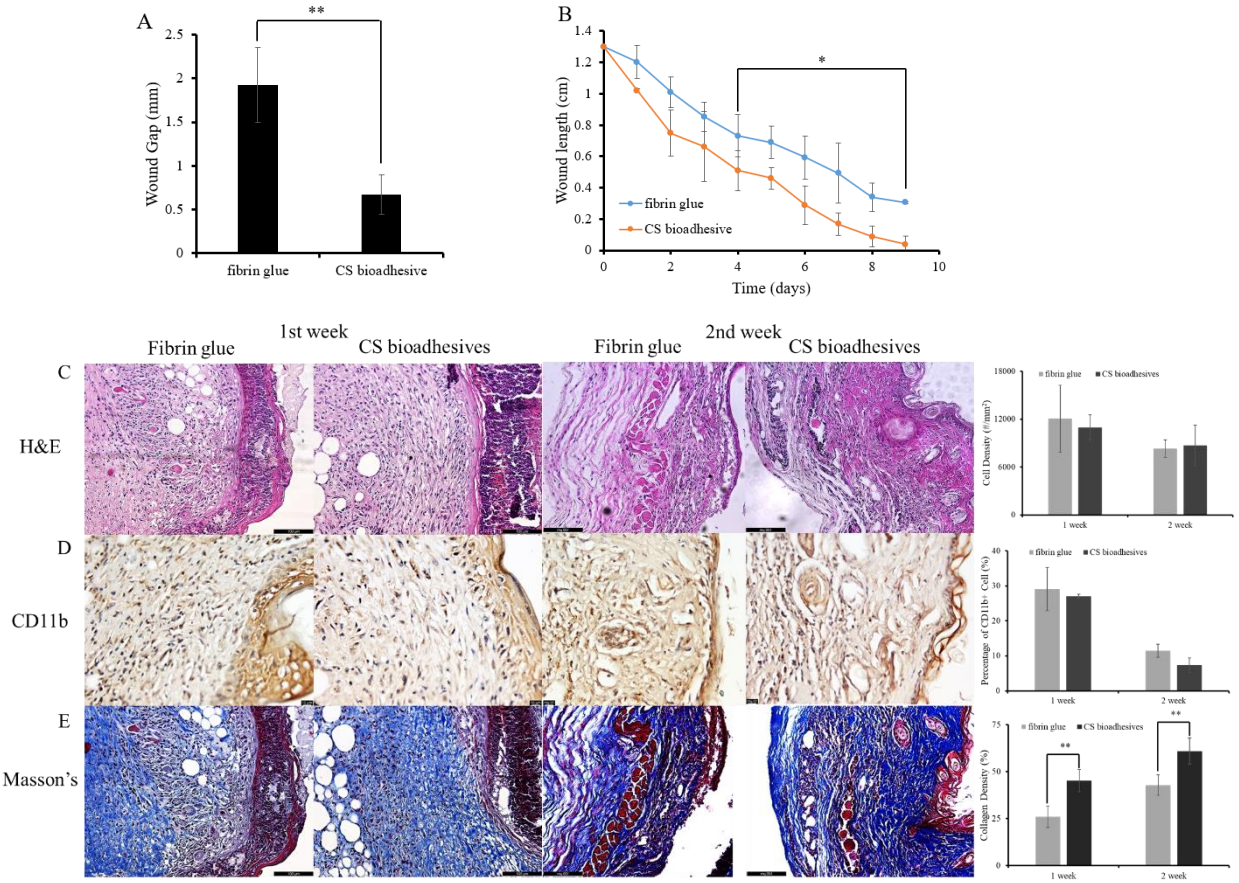

Figure 6. Histological evaluation of the tissue compatibility and skin tissue regeneration properties of skin wounds treated with either fibrin glue or CS bioadhesive on day 7 and 14 post incision. (A) Quantification and comparison of the wound gaps between both treatment on day 7; (B) The effect of bioadhesive on the changes of wound lengths over time up to day 9; (C) Representative images of H&E staining images and quantitative comparison of cell densities between both treatment groups; (D) Representative images of CD11b staining and quantitative comparison of percentages of CD11b positive inflammatory cells between two treatment groups; (E) Representative images of Masson's trichrome staining and quantitative comparison of collagen ratio between both treatment groups.

4. Discussion

In the present study, click chemistry-based CS bioadhesives were fabricated and evaluated for their ability to accelerate wound closure and promote wound healing. By taking advantage of the rapid click chemistry reaction time, we are able to tune the gelation time of the CS bioadhesives to be around 60-70 seconds for various clinical applications. With the optimized formulation, the

adhesive strength of the CS bioadhesives was 2.7 folds higher than that of fibrin glue. The quantitative in vitro cytotoxicity evaluations of the CS bioadhesives supported the application of this material in medical field. Finally, with the application of the CS bioadhesives for wound closure in mice, it showed that the material accelerated wound closure, healing process and led to a better healing outcome compared with traditional fibrin glue. Therefore, the CS bioadhesives can be used to replace the fibrin sealant on wound closure and promote the wound healing process.

To design an ideal bioadhesive, there are several criteria that we can follow: 1) safe, sterializable, and easy to prepare; 2) injectable; 3) rapidly solidify in the physiological condition; 4) strong tissue bonding and adhesion; 5) degradable and absorbable with minimal toxicity; 6) affordable and cost-effective [39, 40]. For the currently FDA approved bioadhesives, they all have their own flaws such as safety over degradation (cyanoacrylates) [41], poor tissue adhesion (fibrin glue) [42], and costly (PEG based sealants) [43]. Based on the result we acquired, the new CS bioadhesives are safe, injectable, with short gelation time (<2 minutes), strong adhesive strength to tissue (2.7 folds over fibrin glue), and degradable with none toxicity. Since the main component, chitosan, is very easy and cheap to acquire, the bioadhesives are cost efficient and easy to prepare.

There is room for improvement on the design of the CS bioadhesives. Firstly, the DS of the TCO or Tz on chitosan is relatively low. With the increasing of DS, the cohesive strength of the hydrogel and storage modulus will be significantly increased. Since TCO/Tz-NHS is insoluble in an aqueous condition, a mixture of DMSO and water was used as the reaction medium to achieve moderate solubility for both chitosan and TCO/Tz, and that could explain the low DS. To possibly solve the issue, TCO/Tz-NHS can be conjugated onto 4-arm PEG-COOH (high MW) first to increase the aqueous solubility. Secondly, other than skin wound closure, tissues that lack of surrounding healthy collagenous structure and fascia supports need to be stitched with

bioadhesives, such as cartilage [44], meniscus [44], cardiac tissue [45] and even blood vessel [46]. For those applications, the CS bioadhesives should be optimized and then tested in the relevant and corresponding wound closure models. Thirdly, inspired by mucosal bioadhesive drug delivery system [47], the CS bioadhesives can be utilized as a drug delivery system to deliver beneficial drug, antibiotics, growth factor, and peptides to the damaged area for a better wound healing process. Since our group has pioneered in using chemokine delivered scaffolds for tissue regeneration with autologous stem cells [48], there is a great potential for the CS bioadhesives to function as a drug delivery and stem cell recruiting scaffold for autologous tissue regeneration purpose.

5. Conclusions

In conclusion, a copper-free click chemistry pair trans-cyclooctene/tetrazine, reacted through the inverse-demand Diels-Alder cycloaddition with high chemoselectivity and ultrafast kinetics, was introduced into chitosan polymers to form the injectable bioadhesives. Upon administration, the CS bioadhesives were firstly crosslinked through click chemistry reaction between TCO and Tz within 2 minutes. The bioadhesives can be grafted onto the surrounding tissue through the hydrogen bond, electrostatic force, and even covalent bond formed by the reaction between aldehydes and primary amines from tissue proteins with the adding of PEG-PALD as a co-crosslinker. The new bioadhesives were proved to be injectable, fast gelated, minimally cytotoxic, strongly adhesive to tissue, and benefit of wound healing. With proper modifications, the potential applications of these CS bioadhesives can be extended as an injectable drug delivery scaffold for both internal and external applications.

Acknowledgments

This work was partially supported by the support from Wilson Charitable Foundation Trust and a Research & Scholarship Excellence Gift.

Supplementary material

Injectable Click Chemistry-based Bioadhesives for Accelerated Wound Closure

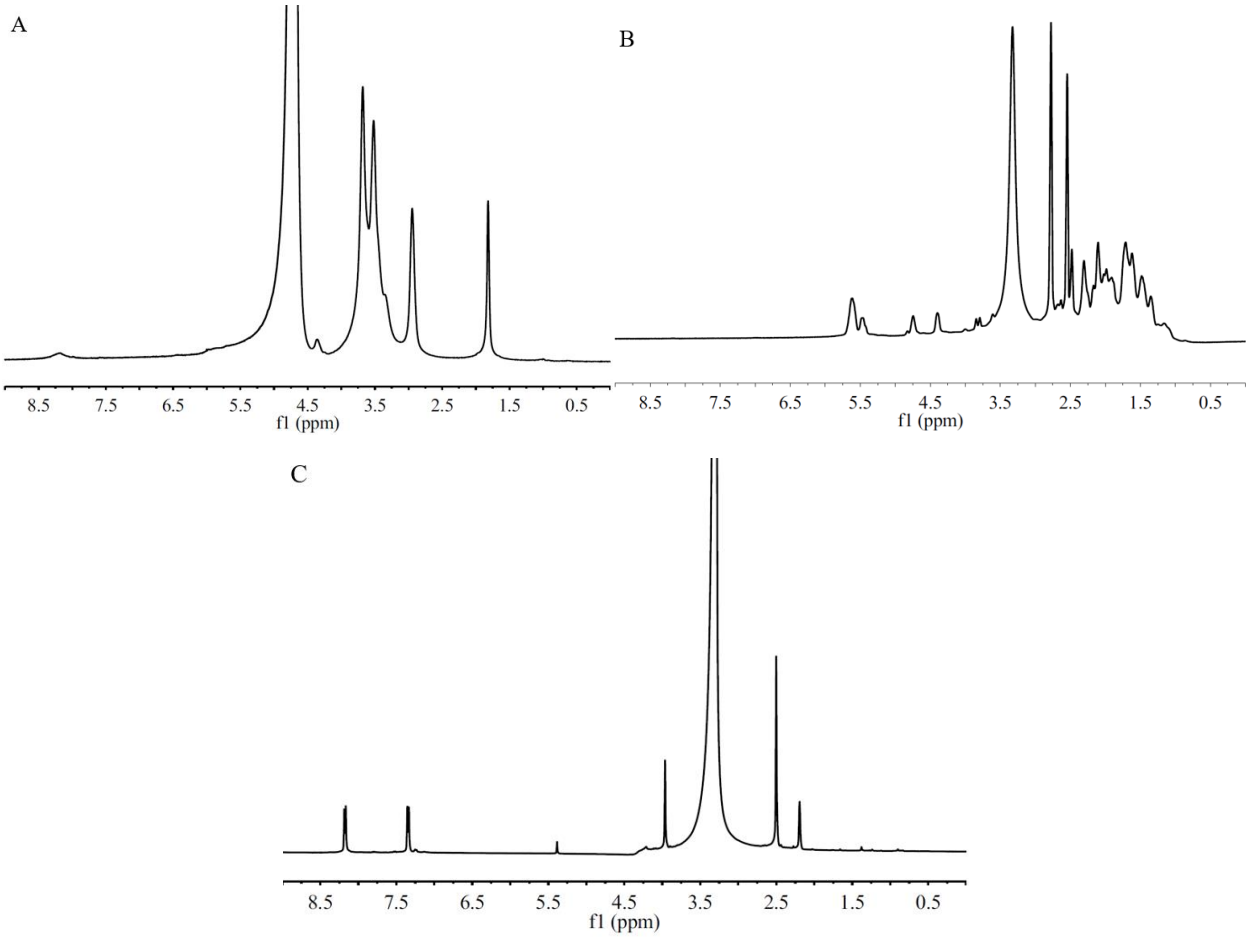

Figure S1. (A) ^{1}H-NMR of CS only in D_2O; (B) ^{1}H-NMR of TCO-NHS in DMSO-d6; (C) ^{1}H-NMR of Tz-NHS in DMSO-d6.

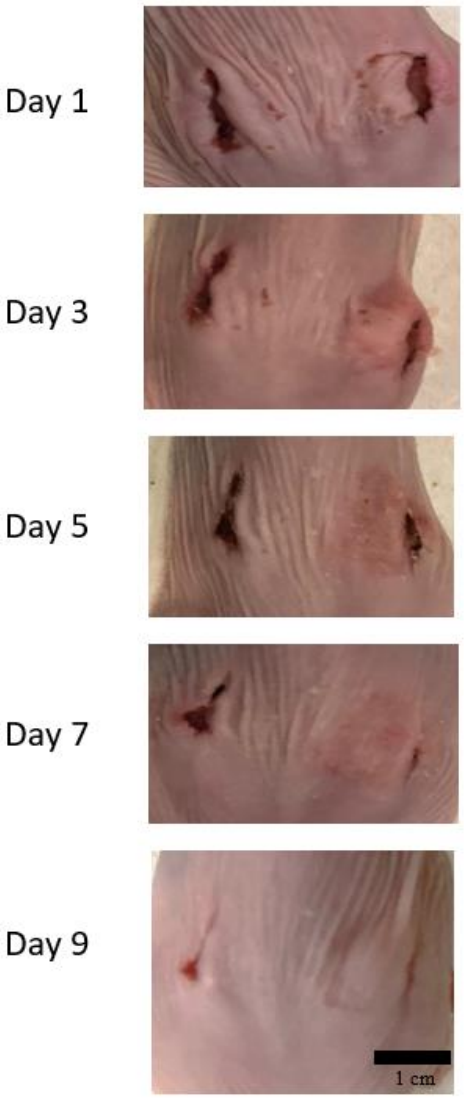

Figure S2. Representative images of the mice incision wounds' healing process with different treatments over 9 days (Left: fibrin glue; Right: CS bioadhesives).

References

[1] K. Yoshihara, Y. Yoshida, N. Nagaoka, D. Fukegawa, S. Hayakawa, A. Mine, M. Nakamura, S. Minagi, A. Osaka, K. Suzuki, Nano-controlled molecular interaction at adhesive interfaces for hard tissue reconstruction, Acta Biomaterialia 6(9) (2010) 3573-3582.

[2] M. Cardoso, A. de Almeida Neves, A. Mine, E. Coutinho, K. Van Landuyt, J. De Munck, B. Van Meerbeek, Current aspects on bonding effectiveness and stability in adhesive dentistry, Australian dental journal 56 (2011) 31-44.

[3] A. Nordberg, P. Antoni, M.I. Montanez, A. Hult, H. Von Holst, M. Malkoch, Highly adhesive phenolic compounds as interfacial primers for bone fracture fixations, ACS applied materials & interfaces 2(3) (2010) 654-657.

[4] J. Simson, J. Crist, I. Strehin, Q. Lu, J.H. Elisseeff, An orthopedic tissue adhesive for targeted delivery of intraoperative biologics, Journal of Orthopaedic Research 31(3) (2013) 392-400.

[5] N. Lang, M.J. Pereira, Y. Lee, I. Friehs, N.V. Vasilyev, E.N. Feins, K. Ablasser, E.D. O'Cearbhaill, C. Xu, A. Fabozzo, A blood-resistant surgical glue for minimally invasive repair of vessels and heart defects, Science translational medicine 6(218) (2014) 218ra6-218ra6.

[6] W.D. Spotnitz, S. Burks, State-of-the-art review: Hemostats, sealants, and adhesives II: Update as well as how and when to use the components of the surgical toolbox, Clinical and Applied Thrombosis/Hemostasis 16(5) (2010) 497-514.

[7] K.A. Vakalopoulos, Z. Wu, L. Kroese, G.-J. Kleinrensink, J. Jeekel, R. Vendamme, D. Dodou, J.F. Lange, Mechanical strength and rheological properties of tissue adhesives with regard to colorectal anastomosis: an ex vivo study, Annals of surgery 261(2) (2015) 323-331.

[8] D.G. Cerdá, A.M. Ballester, A. Aliena-Valero, A. Carabén-Redaño, J.M. Lloris, Use of cyanoacrylate adhesives in general surgery, Surgery today 45(8) (2015) 939-956.

[9] H. Vinters, K. Galil, M. Lundie, J. Kaufmann, The histotoxicity of cyanoacrylates, Neuroradiology 27(4) (1985) 279-291.

[10] W.D. Spotnitz, Fibrin sealant in the United States: clinical use at the University of Virginia, Thrombosis and haemostasis 73(01) (1995) 482-485.

[11] D. Wallace, G. Cruise, W. Rhee, J. Schroeder, J. Prior, J. Ju, M. Maroney, J. Duronio, M. Ngo, T. Estridge, A tissue sealant based on reactive multifunctional polyethylene glycol, Journal of Biomedical Materials Research: An Official Journal of The Society for Biomaterials, The Japanese Society for Biomaterials, and The Australian Society for Biomaterials and the Korean Society for Biomaterials 58(5) (2001) 545-555.

[12] D.H. Sierra, Fibrin sealant adhesive systems: a review of their chemistry, material properties and clinical applications, Journal of biomaterials applications 7(4) (1993) 309-352.

[13] B.P. Lee, P.B. Messersmith, J.N. Israelachvili, J.H. Waite, Mussel-inspired adhesives and coatings, Annual review of materials research 41 (2011) 99-132.

[14] B.K. Ahn, S. Das, R. Linstadt, Y. Kaufman, N.R. Martinez-Rodriguez, R. Mirshafian, E. Kesselman, Y. Talmon, B.H. Lipshutz, J.N. Israelachvili, High-performance mussel-inspired adhesives of reduced complexity, Nature communications 6 (2015) 8663.

[15] L. Han, K. Liu, M. Wang, K. Wang, L. Fang, H. Chen, J. Zhou, X. Lu, Mussel- Inspired Adhesive and Conductive Hydrogel with Long- Lasting Moisture and Extreme Temperature Tolerance, Advanced Functional Materials 28(3) (2018) 1704195.

[16] W. Schultz, Multiple dopamine functions at different time courses, Annu. Rev. Neurosci. 30 (2007) 259-288.

[17] M. Mehdizadeh, J. Yang, Design strategies and applications of tissue bioadhesives, Macromolecular bioscience 13(3) (2013) 271-288.

[18] M. Fernández-Suárez, H. Baruah, L. Martínez-Hernández, K.T. Xie, J.M. Baskin, C.R. Bertozzi, A.Y. Ting, Redirecting lipoic acid ligase for cell surface protein labeling with small-molecule probes, Nature biotechnology 25(12) (2007) 1483.

[19] R. Rossin, P. Renart Verkerk, S.M. Van Den Bosch, R.C. Vulders, I. Verel, J. Lub, M.S. Robillard, In vivo chemistry for pretargeted tumor imaging in live mice, Angewandte Chemie International Edition 49(19) (2010) 3375-3378.

[20] H. Koo, M. Choi, E. Kim, S.K. Hahn, R. Weissleder, S.H. Yun, Bioorthogonal Click Chemistry- Based Synthetic Cell Glue, Small 11(48) (2015) 6458-6466.

[21] Y. Jiang, J. Chen, C. Deng, E.J. Suuronen, Z. Zhong, Click hydrogels, microgels and nanogels: emerging platforms for drug delivery and tissue engineering, Biomaterials 35(18) (2014) 4969-4985.

[22] C. Uttamapinant, A. Tangpeerachaikul, S. Grecian, S. Clarke, U. Singh, P. Slade, K.R. Gee, A.Y. Ting, Fast, cell- compatible click chemistry with copper- chelating azides for biomolecular labeling, Angewandte Chemie International Edition 51(24) (2012) 5852-5856.

[23] B. Oliveira, Z. Guo, G. Bernardes, Inverse electron demand Diels–Alder reactions in chemical biology, Chemical Society Reviews 46(16) (2017) 4895-4950.

[24] N. Mati-Baouche, P.-H. Elchinger, H. de Baynast, G. Pierre, C. Delattre, P. Michaud, Chitosan as an adhesive, European Polymer Journal 60 (2014) 198-212.

[25] P. Sahariah, M. Masson, Antimicrobial chitosan and chitosan derivatives: a review of the structure–activity relationship, Biomacromolecules 18(11) (2017) 3846-3868.

[26] M. Rinaudo, Chitin and chitosan: properties and applications, Progress in polymer science 31(7) (2006) 603-632.

[27] D.W. Lee, C. Lim, J.N. Israelachvili, D.S. Hwang, Strong adhesion and cohesion of chitosan in aqueous solutions, Langmuir 29(46) (2013) 14222-14229.

[28] R. Jayakumar, D. Menon, K. Manzoor, S. Nair, H. Tamura, Biomedical applications of chitin and chitosan based nanomaterials—A short review, Carbohydrate polymers 82(2) (2010) 227-232.

[29] W. Nie, X. Yuan, J. Zhao, Y. Zhou, H. Bao, Rapidly in situ forming chitosan/ε-polylysine hydrogels for adhesive sealants and hemostatic materials, Carbohydrate polymers 96(1) (2013) 342-348.

[30] M.J. Barton, J.W. Morley, D.A. Mahns, D. Mawad, R. Wuhrer, D. Fania, S.J. Frost, C. Loebbe, A. Lauto, Tissue repair strength using chitosan adhesives with different physical-chemical characteristics, Journal of biophotonics 7(11- 12) (2014) 948-955.

[31] M. Sugimoto, M. Morimoto, H. Sashiwa, H. Saimoto, Y. Shigemasa, Preparation and characterization of water-soluble chitin and chitosan derivatives, Carbohydrate polymers 36(1) (1998) 49-59.

[32] J. Guo, W. Sun, J.P. Kim, X. Lu, Q. Li, M. Lin, O. Mrowczynski, E.B. Rizk, J. Cheng, G. Qian, Development of tannin-inspired antimicrobial bioadhesives, Acta biomaterialia 72 (2018) 35-44.

[33] X. Mo, H. Iwata, Y. Ikada, A tissue adhesives evaluated in vitro and in vivo analysis, Journal of Biomedical Materials Research Part A: An Official Journal of The Society for Biomaterials, The Japanese Society for Biomaterials, and The Australian Society for Biomaterials and the Korean Society for Biomaterials 94(1) (2010) 326-332.

[34] M. Mehdizadeh, H. Weng, D. Gyawali, L. Tang, J. Yang, Injectable citrate-based mussel-inspired tissue bioadhesives with high wet strength for sutureless wound closure, Biomaterials 33(32) (2012) 7972-7983.

[35] A. Lončarević, M. Ivanković, A. Rogina, Lysozyme-induced degradation of chitosan: the characterisation of degraded chitosan scaffolds, Journal of Tissue Repair and Regeneration 1(1) (2017) 12.

[36] Z. Değim, N. Celebi, H. Sayan, A. Babül, D. Erdoğan, G. Take, An investigation on skin wound healing in mice with a taurine-chitosan gel formulation, Amino acids 22(2) (2002) 187-198.

[37] A. Suvik, A. Effendy, The use of modified masson's trichrome staining in collagen evaluation in wound healing study, Mal J Vet Res 3 (2012) 39-47.

[38] D.W. Baker, Y.-T. Tsai, H. Weng, L. Tang, Alternative strategies to manipulate fibrocyte involvement in the fibrotic tissue response: pharmacokinetic inhibition and the feasibility of directed-adipogenic differentiation, Acta biomaterialia 10(7) (2014) 3108-3116.

[39] J.A. Callow, A.M. Smith, Biological adhesives, Springer2006.

[40] W. Zhu, Y.J. Chuah, D.-A. Wang, Bioadhesives for internal medical applications: a review, Acta biomaterialia 74 (2018) 1-16.

[41] J.F. Julián Ibáñez, J. Tarascó Palomares, J. Navinés López, J.M. Balibrea del Castillo, E.K. Odermatt, M.A. Pacha Gonzalez, L.F. del Castillo Riestra, N. Guardia Torner, P. Turon Dols, J. Fernandez-Llamazares Rodriguez, Introduction of Flexible Cyanoacrylates in Sutureless Gastric Closure, Surgical innovation 23(5) (2016) 490-497.

[42] P.A. Janmey, J.P. Winer, J.W. Weisel, Fibrin gels and their clinical and bioengineering applications, Journal of the Royal Society Interface 6(30) (2008) 1-10.

[43] N. Annabi, K. Yue, A. Tamayol, A. Khademhosseini, Elastic sealants for surgical applications, European Journal of Pharmaceutics and Biopharmaceutics 95 (2015) 27-39.

[44] I. Strehin, Z. Nahas, K. Arora, T. Nguyen, J. Elisseeff, A versatile pH sensitive chondroitin sulfate–PEG tissue adhesive and hydrogel, Biomaterials 31(10) (2010) 2788-2797.

[45] J. Shin, J.S. Lee, C. Lee, H.J. Park, K. Yang, Y. Jin, J.H. Ryu, K.S. Hong, S.H. Moon, H.M. Chung, Tissue adhesive catechol- modified hyaluronic acid hydrogel for effective, minimally invasive cell therapy, Advanced Functional Materials 25(25) (2015) 3814-3824.

[46] G. Feng, I. Djordjevic, V. Mogal, R. O'Rorke, O. Pokholenko, T.W. Steele, Elastic light tunable tissue adhesive dendrimers, Macromolecular bioscience 16(7) (2016) 1072-1082.

[47] J. Xu, M. Tam, S. Samaei, S. Lerouge, J. Barralet, M.M. Stevenson, M. Cerruti, Mucoadhesive chitosan hydrogels as rectal drug delivery vessels to treat ulcerative colitis, Acta biomaterialia 48 (2017) 247-257.

[48] A.M. Nair, Y.-T. Tsai, K.M. Shah, J. Shen, H. Weng, J. Zhou, X. Sun, R. Saxena, J. Borrelli Jr, L. Tang, The effect of erythropoietin on autologous stem cell-mediated bone regeneration, Biomaterials 34(30) (2013) 7364-7371.

Chapter 4. A Near- infrared Fluorescent pH Sensing Film for Wound Milieu pH Monitoring

Shuxin Li,[1] Hong Vu,[3] Jon Senkowsky,[2] Wenjing Hu,[3] Liping Tang[1]*

1. Department of Bioengineering, University of Texas at Arlington, Arlington, TX 76019, USA
2. Texas Health Physician's Group, 1001 N Waldrop Drive, # 612, Arlington, TX 76012
3. Progenitec Inc., 7301 W Pioneer Parkway, Suite B, Arlington, Texas 76013-2804

* Corresponding author. Department of Bioengineering, University of Texas at Arlington, P.O. Box 19138, Arlington, TX 76019-0138, USA. Tel.: +1 817 272 6075; fax: +1 817 272 2251. E-mail address: ltang@uta.edu.

ABSTRACT

Studies have shown that wound pH is a potentially influential factor in the healing process. Due to the flaws of traditional pH measurement approaches, wound pH measurement has not become part of current standard of care. A near-infrared pH sensitive ratiometric film was created and characterized for measuring wound pH. This film was fabricated by physically absorbing poly (N-isopropyl Acrylamide) nanoparticles conjugated with pH sensitive (CypHer5E) and pH insensitive (Cy7) fluorescent dyes into 2-hydroxyethyl methacrylate hydrogel film. The pH pattern on wounds can be indirectly measured by pressing freshly discarded wound dressing on top of the pH sensitive film and imaging it. *In vitro* tests show that the film can accurately and rapidly detect a wide range of pH (from pH 4 to 8) in wound milieu. Further, patient studies showed that, by measuring pH on wound contact side of discarded wound gauze, the pH and its non-homogeneous distribution on wounds can be indirectly determined. By comparing patients with different wound conditions, we find that near-infrared pH sensing film can be used to measure wound exudate pH with high accuracy and efficiency. In addition, wound pH determination can provide an accurate assessment of wound healing activity in real time.

Keywords: Ratiometric, Wound dressing, Wound healing status, Wound imaging.

1. BACKGROUND

Chronic wounds affect ~6.5 million patients in the United States itself. With no signs of abatement in these numbers, this highly significant burden of over 25 billion dollars on the healthcare system is only expected to increase in the years ahead [1]. Wound pH has been shown to affect many important factors in wound healing responses in many recent publications [2-7]. Thus, monitoring it can give vital information on the status of wound healing. Currently, wound surface pH can be measured in two ways in clinic: litmus paper and glass pH electrode [8]. Litmus papers lack both specificity and accuracy, while glass pH electrode is time consuming, painful and could further aggravate the wound as the electrode is rigid and contacts the wound directly. In addition, both methods acquire average pH value of one point at a time which is neither efficient nor practical [9]. It is plausible that a new imaging modality to reveal pH distribution (instead of an average single-spot measurement) in wound milieu can greatly benefit wound care.

A number of research tools are available to map the pH of the wound environment. For example, luminescent pH detection using pH sensitive dye has been widely used and referenced to measure intracellular pH [10, 11]. However, the applications of these products generally require long scanning time, rigid imaging conditions, and sophisticated equipment, which are not clinically feasible. To overcome these drawbacks, ratiometric pH probes have been created by incorporating both pH sensitive and insensitive dyes which have distinct excitation or emission wavelengths [12]. To measure tissue pH in live animals, we developed an optical ratiometric pH sensor to measure *in situ* pH changes using the ratiometric imaging technique [13]. Based on this early advance, this work was aimed to develop a new technology to measure the pH of wound milieu.

2. QUESTIONS ADDRESSED

To monitor the pH of wound milieu with high accuracy and without directly contacting the wound, we designed a pH sensing film using both ratiometric imaging nanoparticles and ion-exchange membrane. Firstly, both pH-sensitive and pH-insensitive dye were covalently linked to poly(N-isopropylacrylamide) (PNIPAM) nanoparticles which serve as the pH sensing part. Secondly, a2-hydroxyethyl methacrylate (HEMA) membrane was synthesized by free-radical redox polymerization employing ethylene glycol dimethacrylate (EGDMA) as a cross-linker. Thirdly, nanoparticles were physically encapsulated into the membrane which was then ready to use for the imprinting and imaging process. Finally, using the calibration curve generated by the standard simulated wound fluid on the membrane, pH on the membrane was calculated using a software that was developed in-house. A pseudo color map was produced that reflected the wound milieu pH distribution. To test its accuracy and reproducibility, wound dressings from different patients in various stages of healing were tested. Our results support that this new pH sensing film can not only measure pH of wound milieu, but also monitor the change in pH during the wound healing process.

3. EXPERIMENTAL DESIGN

See Appendix S1.

4. RESULTS

To prove that the pH of wound exudate doesn't change through the transportation process from patients' wound to wound dressings, pH of simulated wound fluid (SWF) before and after soaking on the dressings was measured using the skin pH meter. A Bland–Altman mean difference

plot [14] was created for the data comparison (Figure 1K) and 100% of the measurements were within the 95% confidence interval which meant there was excellent concordance between two measurements. This proves that the dressing does not have any significant influence on the pH of SWF. Continuously, after imprinting the contaminated dressings on to the pH sensing film, a strong linear relationship between the fluorescence ratios on the film and the pH values measured by the skin pH meter (Ratio = -8.447 * pH + 82.667, $R^2 = 0.972$; Figure 1L) was found within the simulated measurements. After image processing, the pseudocolor images revealed the pH of SWF on the film which equaled that on gauze sponges (Figure 1L). The pH maps here were no more just measurements of single spots but showed two-dimensional distributions on the measured surface. In conclusion, the pH sensing film can be used to map the pH distribution on simulated gauzes.

The pH sensing film was used to measure pH distribution of wound fluids on wound dressings recovered from different patients (Figure 2A patient #1, Figure 2B patient #2, Figure 2C patient #3, Figure 2D patient #4, Figure 2E-G patient #5 with three visits, and Figure 2H & I patient #6 with two visits). Returning patients (Figure 2E-I) came back to the clinic for dressing replacement every week and wound dressings were typically changed every 3 days. We analyzed the pH distribution on the discarded dressings isolated from several patients with chronic wounds. As shown in the images (Figure 2A-D), chronic wounds typically had uneven pH distribution with most alkaline pH (pH>7.5) and some neutral pH (6.5 <pH< 7.5). By comparing with the optical image (Figure 2B & C), we found that the acidic pH regions of wounds often coincided with the area of granulation tissue indicating localized inflammatory responses.

We also monitored the wound pH distribution following wound debridement in two patients. Interestingly, in the first patient's case (Figure 2E-G), imaging results clearly show that

the wound pH changed from alkaline (pH 7.5-8) to acidic (pH 4.5-5.5). The changes of wound pH may reflect the dynamic changes in wound environment. Some areas of wound had a neutral pH and showed a sign of epithelialization. In the second patient's case (Figure 2H & I), we found similar uneven wound pH distribution which may be caused by different extent of wound healing activities on wounds. The wound pH changes (from alkaline to acidic) were also observed following wound debridement.

5. CONCLUSIONS

There are many approaches for measuring the pH of wound milieu. Using indicator dyes is one of the simplest and most cost-effective methods [15]. In order to study heterogeneous tissue structures such as chronic wounds, optical imaging of pH should be observed and quantified over the whole area rather than at a single point of measurement like a pH glass electrode did [9]. Thus, many researchers incorporated their pH sensitive fluorescent probes into wound dressings [16, 17]. To eliminate errors induced by variations in concentration and distribution of fluorescent probes, a 2D ratiometric luminescence lifetime referencing pH sensor and an RGB ratiometric pH sensor film for *in vivo* imaging has been developed and used directly for human wound pH imaging [18, 19]. However, the most challenging part of this approach is that probes must not leach from the dressings [15]. Our pH sensing film can avoid this drawback as it measures pH of wound exudate on the wound dressing instead of measuring wound milieu directly. The equivalence relation of these two pH values has been proven through the result of the simulated measurement. Additionally, since this device can be used to detect the pH of exudate on many types of wound dressings, clinicians may utilize it to track the changes in wound pH environment.

Many studies have shown that wound milieu pH is a good indicator of wound healing status and associated activities with an alkaline pH being the hallmark of chronic wounds [20-23]. In fact, severity of chronic pressure sores has been correlated with increased wound pH (Stage I – pH 5.7, Stage II- pH 6.9, and Stage III – pH 7.6) [21]. Another study corroborated this observation and concluded that the mean wound surface pH of healing wounds is pH 6.91 compared with pH 7.42 for non-healing wounds [24]. It has also been shown that healing process is associated with the reduction of pH from a baseline of alkaline towards acidic [25]. It is also well established that wound debridement can improve healing of chronic wounds so that they granulate similar to acute wounds [26-29]. Coincidentally, inflammation and tissue granulation are typically found in acute wound with an acidic pH [21, 23, 28]. These early findings support our observation that wound debridement may reduce the pH in chronic wounds. Further study can be carried out to determine the relationship between wound pH and wound healing status which can be assessed by many factors, such as wound closure rate and granulation tissue appearance.

There is a preponderance of evidence pointing towards a strong relationship between pH of wound milieu and wound healing status. Since the change in pH is independent of the gender and ages of patients, etiology of the wound, and the types of wound dressing, it has been suggested that wound pH can be used as a universal indicator for different wounds [20]. It has also been suggested that routine monitoring and alteration of the wound pH using different wound treatments may significantly improve chronic wound therapy outcome [30]. Overall, the measurement and monitoring of wound milieu pH is critical for wound healing process and our pH sensing film can complete this mission efficiently and non-invasively.

ACKNOWLEDGEMENTS

This work was supported by a grant from National Institute of Health (AR064650).

CONFLICT OF INTEREST

Tang has a potential research conflict of interest due to a financial interest with Progenitec Inc. A management plan has been created to preserve objectivity in research in accordance with UTA policy. No competing financial interests exist for other authors.

AUTHOR CONTRIBUTIONS

SXL designed and performed experiments, performed statistical analyses, prepared figures and wrote the manuscript. HV performed experiments and prepared figures. JS assisted in all patient sample collection. WJH and LPT oversaw the project, designed experiments and wrote the manuscript.

TABLES AND FIGURES

Figure 1

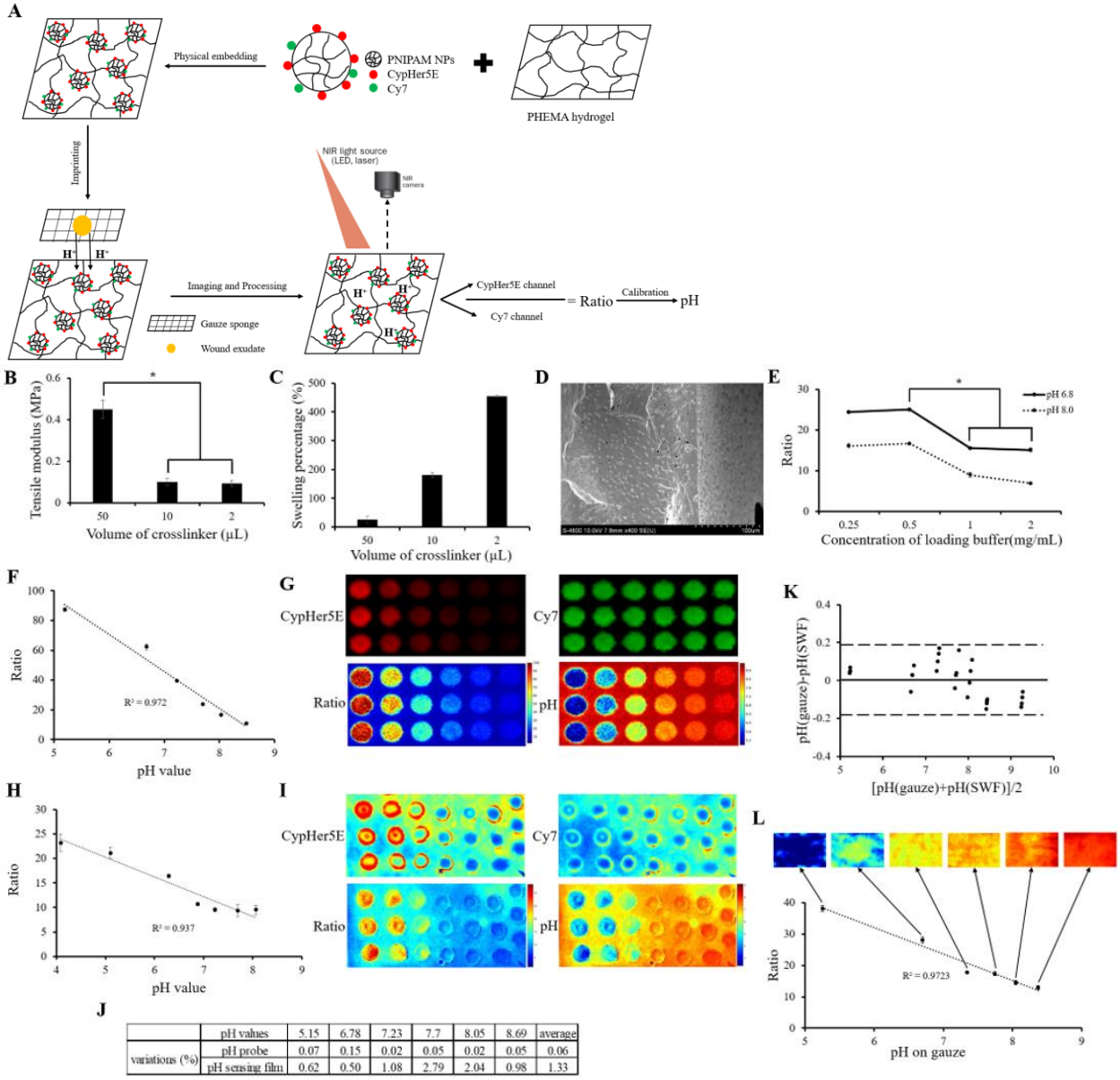

	pH values	5.15	6.78	7.23	7.7	8.05	8.69	average
variations (%)	pH probe	0.07	0.15	0.02	0.05	0.02	0.05	0.06
	pH sensing film	0.62	0.50	1.08	2.79	2.04	0.98	1.33

Figure 1. Schematic diagram of pH probe embedded hydrogel film fabrication as well as application, characterization of pH sensing film, comparison of pH sensitivity between skin pH meter and pH sensing film. **(A)** Firstly, dual dye labeled PNIPAM nanoparticles (pH probes) were fabricated. Secondly, pH probes were physically embedded into PHEMA hydrogel film. Thirdly, discarded dressings from patients were imprinted on the pH probe embedded hydrogel film to allow ionic exchange between wound fluid and hydrogel film. Eventually, dual fluorescent images were taken and the ratio of two fluorescent intensities was determined to calculate pH value based on the calibration curve. **(B)** Tensile modulus of PHEMA hydrogel membrane with different crosslink densities. **(C)** Swelling percentage of PHEMA hydrogel membrane with different crosslink densities. **(D)** SEM images of lyophilized PHEMA hydrogel (10μL crosslinker), thickness~214.3μm. **(E)** Ratio of pH indicator film with different pH probes loading

concentrations at pH 6.8 and 8.0. Student t-test was performed to compare tensile modulus of PHEMA hydrogel film with different crosslink densities and to compare ratio values of pH indicator film with different pH probes loading concentrations at pH 6.8 and 8.0. * $P \leq 0.05$; **(F)** Fluorescence ratios of CypHer5E/Cy7 recorded at different known pH values with 0.5mg/mL pH probes in simulated wound fluid (SWF). **(G)** Pseudocolor images generated through a modified ImageJ software reflecting fluorescent intensity of CypHer5E, Cy7, ratios of CypHer5E/Cy7 and pH distribution. **(H)** Fluorescence ratios of CypHer5E/Cy7 recorded at different known pH values with SWF on pH probe embedded film. **(I)** Pseudocolor images of pH probe embedded film generated through a modified ImageJ software. **(J)** Comparison of measurement variations under different pH conditions using pH probe solution (0.06%) and pH indicator film (1.33%); **(K)** Measurement of pH values in SWF and on SWF soaked gauzes using skin pH meter. The respective Bland–Altman mean difference plot shows 100% of measurements within the 95% confidence interval. **(L)** Relationship of pH values measurements between skin pH meter reading and fluorescence ratios of CypHer5E/Cy7. Pseudocolor pH images of pH probe embedded film imprinted with gauzes soaked with different pH values. The images were generated through modified ImageJ software.

Figure 2

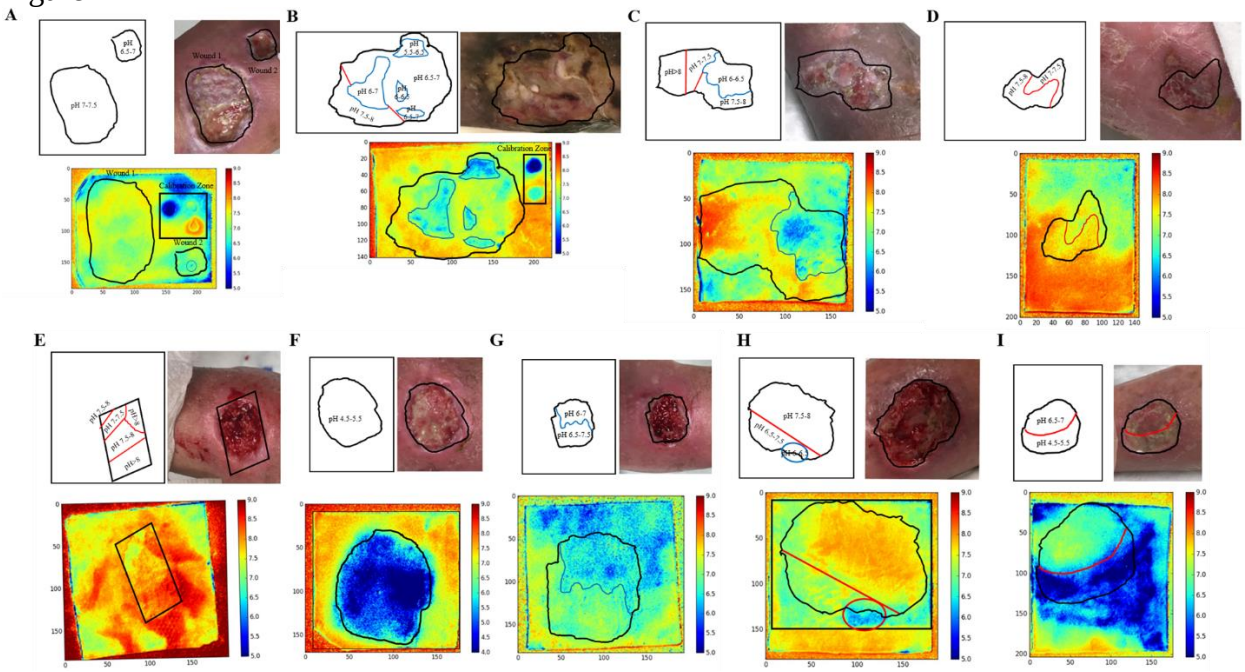

Figure 2. Application of pH indicator film on measuring wound milieu of patients with different wound conditions and monitoring wound healing process of patients with repetitive visits. **(A-D)** Individual patients with a single measurement. **(E-G)** One patient with three continuous visits (once a week). **(H,I)** One patient with two continuous visits (once a week). Wound dressing images and information of these patients. (A) Aquacel® Ag, antimicrobial dressings; (B) Aquacel® Ag, antimicrobial dressings; (C) Aquacel® Ag, antimicrobial dressings; (D) Cutimed® Siltec Sorbact®, foams; (E) Aquacel® Ag, antimicrobial dressings; (F) PolyMem®, foams; (G) Mesalt®, saline gauzes; (H) Mepilex® Border, foams; (I) Aquacel®, hydrocolloids.

REFERENCES

[1] C. K. Sen, G. M. Gordillo, S. Roy, R. Kirsner, L. Lambert, T. K. Hunt, F. Gottrup, G. C. Gurtner, M. T. Longaker, Wound Repair and Regeneration 2009, 17, 763.
[2] L. V. Thomas, J. W. Wimpenny, J. G. Davis, International journal of food microbiology 1993, 17, 289.
[3] T. K. Hunt, H. W. Hopf, Surgical Clinics of North America 1997, 77, 587.
[4] G. Gethin, S. Cowman, "Changes in surface pH of chronic wounds when a honey dressing was used", presented at *Wounds UK Conference Proceedings*, 2006.
[5] I. Rushton, Nursing Standard 2007, 21, 68.
[6] B. Nagoba, R. Gandhi, B. Wadher, R. Potekar, S. Kolhe, Journal of medical microbiology 2008, 57, 681.
[7] S. L. Percival, J. Thomas, S. Linton, T. Okel, L. Corum, W. Slone, International wound journal 2012, 9, 488.
[8] G. Gethin, Wounds uk 2007, 3, 52.
[9] G. S. Walpole, Biochemical Journal 1914, 8, 131.
[10] S. Bassnett, L. Reinisch, D. C. Beebe, American Journal of Physiology-Cell Physiology 1990, 258, C171.
[11] G. Ke, Z. Zhu, W. Wang, Y. Zou, Z. Guan, S. Jia, H. Zhang, X. Wu, C. J. Yang, ACS applied materials & interfaces 2014, 6, 15329.
[12] N. O'Connor, R. B. Silver, Methods in cell biology 2007, 81, 415.
[13] Y. T. Tsai, J. Zhou, H. Weng, J. Shen, L. Tang, W. J. Hu, Advanced healthcare materials 2014, 3, 221.
[14] J. M. Bland, D. Altman, The lancet 1986, 327, 307.
[15] T. R. Dargaville, B. L. Farrugia, J. A. Broadbent, S. Pace, Z. Upton, N. H. Voelcker, Biosensors and Bioelectronics 2013, 41, 30.
[16] S. Trupp, M. Alberti, T. Carofiglio, E. Lubian, H. Lehmann, R. Heuermann, E. Yacoub-George, K. Bock, G. Mohr, Sensors and Actuators B: Chemical 2010, 150, 206.
[17] L. Van der Schueren, K. De Clerck, Coloration Technology 2012, 128, 82.
[18] R. J. Meier, S. Schreml, X. d. Wang, M. Landthaler, P. Babilas, O. S. Wolfbeis, Angewandte Chemie International Edition 2011, 50, 10893.
[19] S. Schreml, R. J. Meier, O. S. Wolfbeis, M. Landthaler, R.-M. Szeimies, P. Babilas, Proceedings of the National Academy of Sciences 2011, 108, 2432.
[20] J. Dissemond, M. Witthoff, T. Brauns, D. Haberer, M. Goos, Der Hautarzt; Zeitschrift fur Dermatologie, Venerologie, und verwandte Gebiete 2003, 54, 959.
[21] A. Glibbery, Int J Microcir Clin Exptl. 1992, 109.
[22] N. Sayegh, J. Dawson, N. Bloom, W. Stahl, Current surgery 1988, 45, 23.
[23] A. Lengheden, L. Jansson, European journal of oral sciences 1995, 103, 148.
[24] G. Roberts, A. Chumley, R. Mani, Wound Repair and Regeneration 2006, 14, A23.
[25] V. Shukla, D. Shukla, S. Tiwary, S. Agrawal, A. Rastogi, Journal of wound care 2007, 16, 291.
[26] D. L. Steed, The American journal of surgery 2004, 187, S71.
[27] H. Brem, M. Tomic-Canic, The Journal of clinical investigation 2007, 117, 1219.
[28] L. A. Schneider, A. Korber, S. Grabbe, J. Dissemond, Archives of dermatological research 2007, 298, 413.

[29] T. Velnar, T. Bailey, V. Smrkolj, Journal of International Medical Research 2009, 37, 1528.
[30] S. Schreml, R. M. Szeimies, S. Karrer, J. Heinlin, M. Landthaler, P. Babilas, Journal of the European Academy of Dermatology and Venereology 2010, 24, 373.

Supplementary materials and methods

1 Fabrication of PHEMA hydrogel film and pH probe embedded film

The PHEMA hydrogel was synthesized by free radical polymerization with HEMA as the monomer, different concentrations of EGDMA as the crosslinker, ammonium persulfate (APS) as a free radical initiator, and N, N, N', N'-tetramethylethylenediamine (TEMED) as a catalyzer. The synthesis was carried out as described earlier with minor modifications [1]. To start with, 2.7mL of HEMA was mixed with 1mL of DI water in a glass vial. 2, 10, and 50 μL (0.074%, 0.37% and 1.85% of monomers) of EGDMA was added into the solution to acquire hydrogel with different crosslink density. The mixed solution was bubbled with nitrogen for 15 minutes to strip off the oxygen. Meanwhile, to create a mold for the hydrogel, a piece of Parafilm was cut into a hollow center shape as a spacer (240μm thickness) and was placed between two flat glass plates. After adding 100 mg of APS into the solution and mixing well, 100 μL of TEMED was added into the mixture. Instantly, as the reaction was taking place vigorously, the viscous solution was dropped on one glass plate along the edge of the spacer and the other glass plate was used to mount it. Following overnight reaction at room temperature, the membrane was peeled off and dialyzed against DI water for at least three days. The dual dye labeled PNIPAM nanoparticles (abbreviated as "pH probes") were fabricated using a precipitation polymerization method as described earlier [2]. To load the pH probes into the PHEMA hydrogel film and achieve the best measurement efficiency, pH probes were absorbed into hydrogel membrane physically by placing dehydrated PHEMA hydrogel membrane into 0.25, 0.5, 1, and 2 mg/mL pH probes suspension in DI water (Figure S1).

2 Characterization of PHEMA hydrogel film and pH probe embedded film

A series of tests were carried out to evaluate the physical, mechanical and optical properties of the hydrogel film. First, the tensile strength of hydrogel with different crosslink densities was tested with MTS electromechanical tension system (MTS Systems Corporation, MN, USA) under 10 mm/min preload stress speed at room temperature. Tensile modulus was calculated as: Tensile modulus (MPa) = {load at break (N)/ [original width (mm) X original thickness (mm)]}/ [elongation at break (mm)/ initial length (mm)] [3]. Second, swelling ratios of the hydrogel with different crosslink densities were tested based on the existing protocol with minor modification [4]. The swelling ratio can be calculated by using the following formula: Swelling ratio (%) = $[(W_s - W_d)/W_d] \times 100\%$, where W_s equals to the weight of hydrogel composites after swelling in DI water and W_d equals to the weight of dried hydrogel composites after swelling. Third, the sensitivities of pH sensing films with different loading concentrations were tested with PBS (pH 6.8 and 8.0). Briefly, 20 µL of PBS solution (pH 6.8 and 8.0) was dropped on the pH sensing films and Kodak In vivo FX Pro (Kodak, USA) imaging system was used to record the fluorescence on the films. For the imaging procedure, CypHer5E was excited at 630 nm and the fluorescence emission wavelength was 700 nm with an exposure period of 10 seconds, whereas Sulfo-Cy7 NHS ester was excited at 760 nm and the fluorescence emission wavelength was 830 nm with an exposure time of 3 seconds (f/stop, 2.5; 4 × 4 binning). The images were analyzed with an in-house software that was developed using MATLAB [5]. Finally, the morphology of lyophilized membrane loaded with pH probes and the existence of pH probes were verified using the SEM. Hydrogel membrane with high crosslink density (50µL crosslinker) had a tensile modulus of 0.45±0.045 MPa, with medium crosslink density (10µL crosslinker) had a tensile modulus of 0.10±0.018 MPa, and with low crosslink density (2µL crosslinker) had a tensile modulus of 0.093±0.016 MPa (Figure 1B). Swelling percentage of hydrogel membrane with high crosslink density, medium crosslink density, and low crosslink density was 25.5±2.0%, 180.9±8.6%, and 455.2±12.2% (Figure 1C). Hydrogel membrane with high crosslinking density was too stiff to stay intact for imaging during the measurement process. Those with low crosslinking density would contain more water that could dilute the wound exudate and lead to a neutral pH reading. Thus, PHEMA hydrogel membrane for pH

sensing film fabrication was synthesized with medium crosslinking density. A cross-section of the lyophilized PHEMA hydrogel membrane with medium crosslinking density was visualized using SEM which showed that the thickness of the membrane was around 214.3µm (Figure 1D). As the PHEMA hydrogel membrane and pH probes are combined through physical adsorption, it is important to optimize the concentration of the loading buffer for achieving the best measurement efficiency. With a loading concentration of 0.25, 0.5, 1, and 2 mg/mL, the ratio of CypHer5E to Cy7 on the pH sensing film was 24.35±0.26, 24.97±0.28, 15.47±0.22, and 15.03±0.43 respectively at a measured pH of 6.8 and 16.05±0.64, 16.60±0.10, 8.92±0.64, and 6.83±0.18 respectively at measured pH of 8.0 (Figure 1E). The bell-shaped fluorescence intensity curve indicates that the fluorescence increases with probe concentrations up to 0.5 mg/mL. Then, the fluorescence intensity decreases with increase in probe concentration due to fluorescence quenching as described earlier. The overall results showed that the optimal probe loading concentration was 0.5 mg/mL, since this concentration had the highest ratiometric values indicating highest pH detection sensitivity.

3 Sensitivity measurement of the pH sensing film

A previous study showed that pH probes can measure pH value ranging from 5.78 to 7.65 using the ratiometric imaging method [6]. Herein, after the physical combination of the pH probes with PHEMA hydrogel membrane, it was necessary to test if the pH sensing film retained its pH sensitivity. In order to simulate the pH measurement of wound exudate, simulated wound fluid (SWF) was prepared according to an existing protocol [7]. For assessing pH probe sensing ability, 20 µL of pH probes suspension in DI water (2.5mg/mL) was added into 80 µL of SWF (with various pH, including pH 5.20, pH 6.68, pH 7.23, pH 7.70, pH 8.03, and pH 8.49) in 96-well plate. The plate was imaged and analyzed as mentioned previously to acquire a linear calibration function. Pseudocolor images were algorithmically generated with the software. Ratio image was calculated by dividing CypHer5E image by Cy7 image. The pH image was calculated by substituting relevant calibration function. For pH sensing film, after loading with a suspension of pH probes

in DI water (0.5mg/mL), the film was placed on a transparent film that served as an imaging platform. 20 µL of SWF (with various pH, including pH 4.09, pH 5.10, pH 6.29, pH 6.88, pH 7.23, pH 7.69, and pH 8.06) was dropped on the surface of the film without any cross contamination. Each group was repeated for at least three times. The pH sensitive property of the pH probes before and after loading into the PHEMA film was tested with the SWF. Using nanoparticles to measure various SWF in different pH, we were able to establish a strong linear relationship between the fluorescence ratios of CypHer5E to Cy7 and the pH values from 5.20 to 8.49 (Ratio = -24.91 * pH + 220, $R^2 = 0.97$; Figure 1F). After image processing and the calibration function substitution, pseudocolor images were output to visualize fluorescence intensities in different channels, fluorescence ratios, and pH value of the SWF in the 96-well plate (Figure 1G). For the pH sensing film, there was a strong linear relationship between the fluorescence ratios and the pH values from 4.09 to 8.06 (Ratio = -4.022 * pH + 40.308, $R^2 = 0.937$; Figure 1H). Through similar processing method, the pseudocolor images were generated with the self-developed software and visually showed the pH of the SWF on top of the film (Figure 1I). The result showed that pH sensitive property of the pH probes remained after embedding into PHEMA hydrogel membrane and the pH sensing film was capable of quantitatively measuring pH using the ratiometric imaging method. The pH measurement variations using pH probe solution in 96-well plate was 0.06% while using pH sensing film was 1.33% which indicated that the pH sensing film measurement was still accurate and consistent (Figure 1J).

4 Diagram depicting usage of the pH sensing film for simulated measurements

In order to avoid direct contact with patient's wound and potentially contaminating it, the pH sensing film was designed to measure the pH of wound exudate stained on the dressings. The working principle is based on ion-exchange process which transports the H^+ and OH^- from wound exudate on the gauze sponges to DI water on the hydrogel film rapidly (Figure 1A). In detail, freshly collected wound dressings from patients was imprinted onto pH sensing film placed on a transparency film for few seconds. Then, on the side of the sensing film, 20 µL of SWF (with pH 5.00, pH 6.50, and pH 8.00) was added onto

the film as pH references. Finally, the film was imaged as previously described and ratio image was acquired through a ratiometric calculation. The image pH was calculated based on the calibration function (Figure 1A). As the area of the wound exudate on the dressing corresponded to the wound milieu on the patient, the pH map indicates the pH of the wound milieu. Further studies were carried out to test whether the pH of wound exudate remains the same during the transportation process from patients' wound to the dressings. For that, an SWF was employed. A HI-99181 Skin pH Meter (Hanna Instruments Ltd, England, UK) was used here to measure the pH of SWF (200 µL, pH=5.20, 6.68, 7.23, 7.70, 8.03, and 8.49) before and after being dropped on the surgical dressings (Dynarex Corporation, NY, USA). Simultaneously, we also carried out pH measurement on SWF solution and SWF soaked gauzes using ratiometric imaging method. By comparing the pH reading between SWF in solution and on gauze, we determined whether exposure to gauze affects the value of wound pH. Finally, the relationship between pH values of the gauze sponges and ratio of fluorescent intensities was analyzed. All experiments were repeated at least three times.

5 Effect of multiple types of wound dressings on pH of simulated wound fluid

Simulated wound fluid (SWF) with pH of 4, 6 and 8 were prepared separately. Each dressing was cut into small pieces and soaked into SWF in 24-well plate, with a constant weight-to-volume ratio of 1%. Then it was incubated for 24 hours at room temperature. pH was measured before incubation and at the end of incubation using a pH meter. The tested wound dressings that are currently used in clinic include Foams - Curity™ gauze sponges (Covidien/ Medtronic, Minneapolis, Minnesota), Cutimed® Siltec Sorbact® (BSN medical, Inc., Charlotte, NC), Mepilex® Border (Mölnlycke Health Care US, LLC., Norcross, Georgia), Enluxtra (OSNovative Systems, Inc, Santa Clara, CA), Hydrofera Blue® (Hollister Incorporated, Libertyville, IL); Hydrocolloids–Aquacel®, DuoDerm® CGF™, DuoDerm® Hydrocolloid (ConvaTec Inc., Oklahoma City, OK); Saline gauzes–Mesalt® (Mölnlycke Health Care US, LLC., Norcross, GA); Films - Mepitel® One (Mölnlycke Health Care US, LLC., Norcross, GA), Xeroform® Occlusive Petrolatum Gauze Strip (Covidien/ Medtronic, Minneapolis, Minnesota), Steri-Strip™ (3M, MN);

Alginates - MEDIHONEY® (Derma Sciences Inc., Plainsboro, New Jersey); Antimicrobial dressings – Aquacel® Ag (ConvaTec Inc., Oklahoma City, OK), Mepitel® Ag (Mölnlycke Health Care US, LLC., Norcross, GA), Restore Contact Layer with Silver (Hollister Incorporated, Libertyville, IL), InterDry® Ag (Coloplast, Minneapolis, MN), Iodoflex* Cadexomer Iodine (Smith & Nephew, Fort Worth, TX), PROMOGRAN PRISMA™ Matrix (Systagenix, San Antonio, TX); Knitted fabric dressings - Curity™ Non-Adherent Strips (Covidien/ Medtronic, Minneapolis, Minnesota).

6 Application on pH measurement of the patients' gauze sponges

To fulfill the practical application of this device, freshly disposed wound dressings from several anonymous patients were collected during their visit at the Texas Health Arlington Memorial Wound Care and Limb Salvage Clinic, TX, USA. Two of these patients returned for routine treatment and their wound dressings were collected over time to study how the pH of the wound milieu changed as the wound healing process. Meanwhile, an image of the wound was taken right after the removal of the used dressing as a comparison for the pH measurement result. All the samples from the patients and the relevant measurement results were labeled with reception date. In the analysis process, outline of wound exudate and wound itself were marked both on the digital image of the patient's wound and on the pseudocolor pH map of the outcome. The pH of wound milieu can thus be matched with the pH map coordinately.

References

[1] Y. Kapoor, A. Chauhan, Journal of colloid and interface science 2008, 322, 624.
[2] R. Pelton, P. Chibante, Colloids and Surfaces 1986, 20, 247; J. Zhou, Y.-T. Tsai, H. Weng, D. W. Baker, L. Tang, Biomaterials 2011, 32, 9383.
[3] B. Demczyk, Y. Wang, J. Cumings, M. Hetman, W. Han, A. Zettl, R. Ritchie, Materials Science and Engineering: A 2002, 334, 173.
[4] H. Park, X. Guo, J. S. Temenoff, Y. Tabata, A. I. Caplan, F. K. Kasper, A. G. Mikos, Biomacromolecules 2009, 10, 541.
[5] Z. Peng, J. Zhou, A. Dacy, D. Zhao, V. Kearney, W. Zhou, L. Tang, W. Hu, Journal of biomedical optics 2017, 22, 016010.

[6] Y. T. Tsai, J. Zhou, H. Weng, J. Shen, L. Tang, W. J. Hu, Advanced healthcare materials 2014, 3, 221.
[7] J. Said, C. C. Dodoo, M. Walker, D. Parsons, P. Stapleton, A. E. Beezer, S. Gaisford, International journal of pharmaceutics 2014, 462, 123.

Figure S1

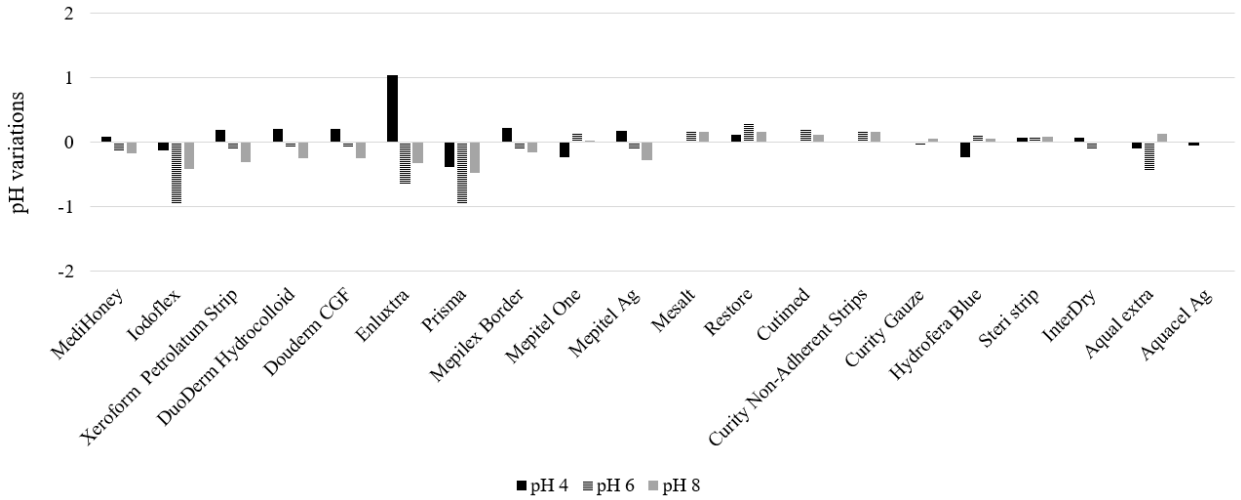

Figure S1. Effect of different types of wound dressings on pH of simulated wound fluid.

Figure S2

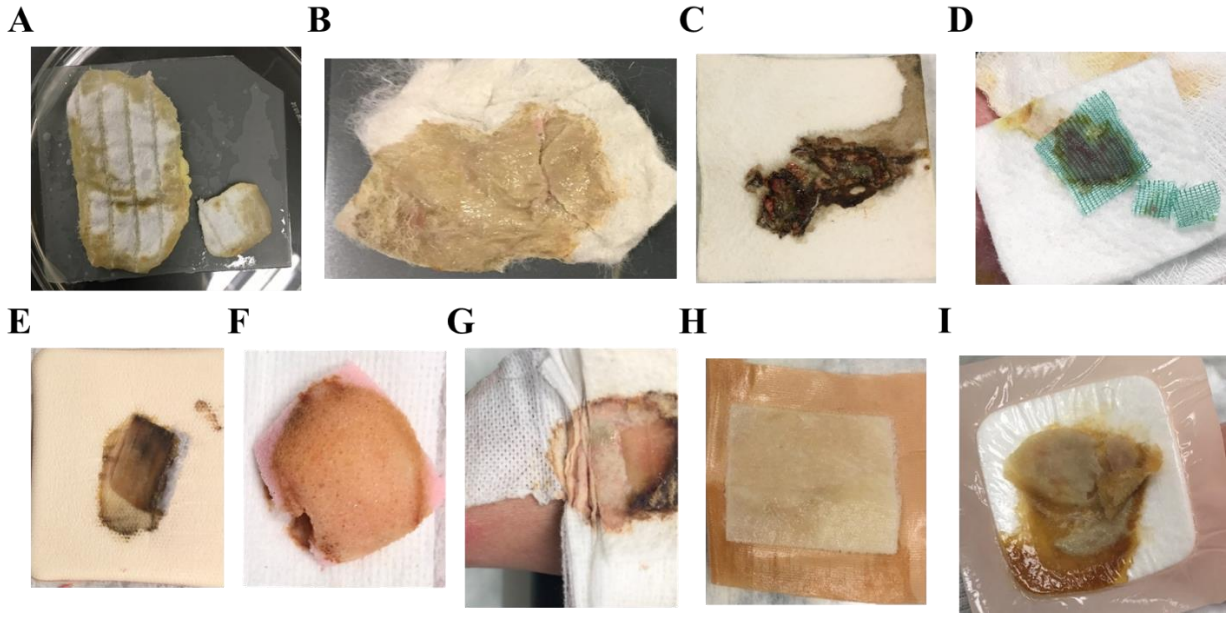

Figure S2. The images and information of different discarded wound dressings used in this investigation. **(A)** Aquacel® Ag, antimicrobial dressings; **(B)** Aquacel® Ag, antimicrobial dressings; **(C)** Aquacel® Ag, antimicrobial dressings; **(D)** Cutimed® Siltec Sorbact®, foams; **(E)** Aquacel® Ag, antimicrobial dressings; **(F)** PolyMem®, foams; **(G)** Mesalt®, saline gauzes; **(H)** Mepilex® Border, foams; **(I)** Aquacel®, hydrocolloids.

Chapter 5. Summary and Future Work

Every single project I have been working on is aiming to improve people's life with the approaches of biomedical engineering I have concurred. However, there is some additional work needed to translate these technologies. A list of the additional work is summarized below.

In Chapter 1, for early stage osteoarthritis diagnosis, the HA probes can target the activated macrophages on the osteoarthritic cartilage. Moreover, we are the first group to detect activated macrophages on osteoarthritic human cartilage and apply the probes to *ex* vivo human cartilage sample for severity diagnosis. For FDA approval, NIR dye used in this study may be replaced with an FDA approved NIR dye, such as ICG [1]. Since the idea of creating theranostics is emerging, the diagnostic probes for osteoarthritis can be encapsulated with biomolecules and drug to facilitate localized tissue regeneration. To evaluate the efficiency of the developed theranostic nanoparticles, the intra-articular tibial plateau fracture (IATPF) model can be used to study early stage of OA which is mainly induced by the inflammation [2]. Since we have already done tissue regeneration study using small animal model (rabbit), large animal model, such as sheep whose anatomical structure is similar to humans [3], is needed for further investigation.

In Chapter 2, for delivery of antimicrobial peptides, since many strains of bacteria produce alkaline environment under aerobic condition [4], there is a great need to design an alkaline-responsive self-assembly nanofiber to deliver the antimicrobial peptides under those circumstances. Esculentin-2EM, an α-helical peptide isolated from the frog, may be used for this purpose since the lytic activity of the peptide against membranes of Gram-positive bacteria has been shown to significantly enhanced under an alkaline environment [5]. Also, since all the antimicrobial effect of the self-assembly nanofibers were tested through *in vitro* study and the

multidomain peptides have no cytotoxicity, the antimicrobial activities of these self-assembly nanofibers should be tested in relevant animal infection models, such as mice [6] and rabbit [7].

In Chapter 3 and for bioadhesives development for wound closure, we are the first to employ inverse-demand Diels-Alder cycloaddition reaction, copper-free click chemistry pair trans-cyclooctene /tetrazine into the bioadhesives in order to increase the adhesive strength. Surprisingly, the bioadhesives can not only close the wound within few minutes, but also accelerate the wound healing process in the mice incised wound healing experiment. Thirdly, for wound milieu pH measurement, we are the first group to develop this non-contact approach with high accuracy and fast speed. The outcome of all these projects can be translational and further developed for clinical application. It should be noted that the bioadhesive can be further developed and used as a drug delivery vehicle for wound healing promotion as shown in many previous works [8-10]. For example, the bioadhesives can be developed for glenoid labrum tear regeneration through the cooperation of cellulose since it can provide higher tensile and compressive strength without introducing any toxicity [11]. Moreover, with the adding of gelatin [12], the bioadhesives may be used as a cell friendly scaffold to recruit cells for tissue regeneration. Also, since chitosan itself has been widely used as an antimicrobial material [13], the bioadhesives can be tested for its antimicrobial property which will expand its application in wound infection treatment.

The pH sensing film represents the first group of diagnosis tools for chronic wound diagnosis. Similar technology can be further developed for sensing other wound biomolecules, such as reactive oxygen species, blood sugar, matrix metalloproteinases, and oxygen content, can be used to monitor the wound healing process [14]. These new sensing films will no doubt to assist the physicians to monitor patients' long-term wound healing process.

References

[1] Kaplan-Marans, Elie, et al. "Indocyanine Green (ICG) in urologic surgery." Urology (2019).
[2] Goldring, Mary B., and Miguel Otero. "Inflammation in osteoarthritis." Current opinion in rheumatology 23.5 (2011): 471.
[3] Proffen, Benedikt L., et al. "A comparative anatomical study of the human knee and six animal species." The Knee 19.4 (2012): 493-499.
[4] Padan, Etana, et al. "Alkaline pH homeostasis in bacteria: new insights." Biochimica et biophysica acta (BBA)-biomembranes 1717.2 (2005): 67-88.
[5] Malik, Erum, et al. "pH dependent antimicrobial peptides and proteins, their mechanisms of action and potential as therapeutic agents." Pharmaceuticals 9.4 (2016): 67.
[6] Chai, Zhilan, et al. "A facile approach to functionalizing cell membrane-coated nanoparticles with neurotoxin-derived peptide for brain-targeted drug delivery." Journal of Controlled Release 264 (2017): 102-111.
[7] Yousry, Carol, et al. "Studying the influence of formulation and process variables on Vancomycin-loaded polymeric nanoparticles as potential carrier for enhanced ophthalmic delivery." European Journal of Pharmaceutical Sciences 100 (2017): 142-154.
[8] Saghazadeh, Saghi, et al. "Drug delivery systems and materials for wound healing applications." Advanced drug delivery reviews 127 (2018): 138-166.
[9] Kim, Bum Jin, et al. "A ccelerated skin wound healing using electrospun nanofibrous mats blended with mussel adhesive protein and polycaprolactone." Journal of Biomedical Materials Research Part A 105.1 (2017): 218-225.
[10] Pereira, Gabriela Garrastazu, et al. "Polymeric films loaded with vitamin E and Aloe vera for topical application in the treatment of burn wounds." BioMed research international 2014 (2014).
[11] Gupta, Praveen Kumar, et al. "An Update on Overview of Cellulose, Its Structure and Applications." Cellulose. IntechOpen, 2019.
[12] Huang, Yan, et al. "In vitro characterization of chitosan–gelatin scaffolds for tissue engineering." Biomaterials 26.36 (2005): 7616-7627.
[13] Perinelli, Diego Romano, et al. "Chitosan-based nanosystems and their exploited antimicrobial activity." European Journal of Pharmaceutical Sciences 117 (2018): 8-20.
[14] Li, Shuxin, et al. "Imaging in Chronic Wound Diagnostics." Advances in Wound Care (2019).

Biography

Shuxin Li's research interests focus on using chemokine delivery scaffolds for autologous musculoskeletal tissue regeneration and developing biomedical devices for wound healing process monitoring. He received his bachelor degree in Biomedical Engineering from Peking University in 2015 and his undergraduate thesis was about "Stretch and Pressure on the Mice Abdominal Aorta and Modeling of its Biomechanics". He joined Dr. Liping Tang's group in the Bioengineering Department at UTA as a PhD student and started to work on developing biomaterials-based strategies for tissue engineering application. With four years of studying and researching, he published one review paper and two research papers as a first author and he had another one review paper and one research paper under submission. He published another three papers through cooperation with other researchers.

Academic degrees

UT Arlington, Texas, USA (August 2015 – December 2019)
Degree: Doctor of Philosophy
Major: Bioengineering

Peking University, Beijing, China (Sep 2011 – Jun 2015)
Degree: Bachelor of Science
Major: Biomedical Engineering

Publications and Awards

A. Conferences

1. **Li S**, Tang L. Hyaluronic Acid Based Nanoscaffold for Cartilage Regeneration. *UTA Annual Celebration of Excellence by Students*. 2016, Arlington, Texas.
2. **Li S**, Zhou J, Hakamivala A, Ramesh S, Borrelli J, Tang L. Stem cell therapy of PTOA using erythropoietin-incorporated HA microscaffolds *Military Health System Research Symposium*. 2017, Kissimmee, Florida.
3. **Li S**, Zhou J, Hakamivala A, Huang Y, Cong W, Borrelli J, Tang L. Treatment of Osteoarthritis Using Macrophage-Targeting Hyaluronic Acid Microscaffolds. *Society for Biomaterials annual meeting*. 2018, Atlanta, Georgia (Invited for a rapid-fire presentation).
4. **Li S**, Tang, L. Functionalized Hyaluronic Acid Microscaffolds for Avascular Meniscus Tear Diagnosis and Therapy. *UTA Annual Celebration of Excellence by Students*. 2018, Arlington, Texas.
5. **Li S**, Tang, L. Injectable drug loaded fibrin gel for glenoid labrum tear regeneration. *iC3 Life Science Summit*. 2018, Arlington, Texas.
6. **Li S**, Borrelli J, Tang L. Injectable chemokine loaded fibrin gel for glenoid labrum tear regeneration. *Society for Biomaterials annual meeting*. 2019, Seattle, Washington.
7. **Li S**, Borrelli J, Tang L. Chemokine Releasing Gel for Glenoid Labrum Tear Regeneration. *Biomedical Engineering Society*. 2019, Philadelphia, Pennsylvania.

B. Publications

1. **Li S**, Cong W, Hakamivala A, Huang Y, Borrelli J Jr, Tang L. Hyaluronic Acid-Based Optical Probe for the Diagnosis of Human Osteoarthritic Cartilage. *Nanotheranostics* 2018; 2(4):347-359 (cover image).
2. Khang M K, Zhou J, Huang Y, Hakamivala A, **Li S**, Tang L. Correction: Preparation of a novel injectable in situ-gelling nanoparticle with applications in controlled protein release and cancer cell entrapment. *RSC Advances*. 2018; 8(72):41376-41376.
3. Chen W, **Li S**, Renick PJ, Yang S, Pandey N, Boutte C, Nguyen KT, Tang L, Dong H. Bacterial Acidity-Triggered Antimicrobial Activity of Self-assembling Peptide Nanofibers. *Journal of Materials Chemistry B*. 2019; 7(18):2915-2919.
4. **Li S**, Ali H M, Senkowsky J, Nair A, Tang L. Imaging in Chronic Wound Diagnostics. *Advances in Wound Care*. 2019.
5. Chen W, Yang S, **Li S**, Lang J C, Mao C, Kroll P, Tang L, Dong H. Self-Assembled Peptide Nanofibers Display Natural Antimicrobial Peptides to Selectively Kill Bacteria without Compromising Cytocompatibility. *ACS applied materials & interfaces*. 2019; 11(32): 28681-28689.
6. **Li S**, Vu H, Senkowsky J, Hu W, Tang L. A near infrared fluorescent pH indicator film for wound milieu pH monitoring. *Experimental Dermatology*. 2019.

7. **Li S**, Renick PJ, Senkowsky J, Nair A, Tang L. Diagnostics for wound infection. Advances in Wound Care. 2019 (under review).

8. **Li S**, Zhou J, Huang Y, Roy J, Tang L. Injectable Click Chemistry-based Bioadhesive for Accelerated Wound Closure. 2019 (under review).

9. Huang Y, Hakamivala A, **Li S,** Nair A, Ramesh S, Hsieh J, Tang L. Chemokine releasing particle implants for trapping circulating prostate cancer cells. *Scientific Report*. 2019 (under review).

10. Hakamivala A, **Li S,** Huang Y, Yu S, Yuan B, Tang L. Recruitment of endogenous progenitor cells by erythropoietin loaded particles for in situ cartilage regeneration. *Bioactive Materials*. 2019 (under review).

11. **Li S**, Borrelli J Jr, Tang L. Injectable chemokine loaded bioadhesives for glenoid labrum tear regeneration. 2019 (manuscript preparation).

C. Honor and Award

2016, recipient of **Franklyn Alexander PhD Scholarship**, College of Engineering, University of Texas at Arlington, Arlington, Texas.

2016-Present, recipient of **Bioengineering STEM Doctoral Fellowship,** Department of Bioengineering, University of Texas at Arlington, Arlington, Texas.